Doctoral Dissertation

Electron Microscopy Analysis of the Local Structure of Kanazawa Gold Leaf and Investigation of Its Formation Mechanism

XU YUANZHE

SUPERVISOR: YOSHIFUMI OSHIMA

GRADUATE SCHOOL OF ADVANCED SCIENCE AND TECHNOLOGY

JAPAN ADVANCED INSTITUTE OF SCIENCE AND TECHNOLOGY

[MATERIALS SCIENCE]

December 2025

ABSTRACT

2220019 Xu Yuanzhe

Kanazawa gold leaf, a traditional Japanese material renowned for its exceptional thinness and brilliant metallic luster, is produced through a meticulous hammering process that reduces its thickness to nanoscale dimensions. This study examines the distinct plastic deformation mechanisms and crystallographic texture evolution associated with the production of Kanazawa gold leaf. We focus on the various properties of Kanazawa Gold Leaf. By employing advanced analytical techniques such as Transmission Electron Microscopy (TEM) and Electron Backscatter Diffraction (EBSD), the research aims to analyze the microstructural transformations at the nanoscale during hammering.

Kanazawa gold leaf is fabricated using intricate hammering techniques to create a very thin film, approximately 200 nm in thickness. It has been reported that the (001) texture is formed; however, the mechanism of its formation remains unknown. We are utilizing electron backscatter diffraction (EBSD) and ultrahigh-voltage transmission electron microscopy (UHV-TEM). We found that a (011) slip system emerges in the thin Kanazawa gold leaf, which is unusual in face-centered cubic (FCC) crystals. We discuss the critical role of this (011) slip in the formation of the (001) texture.

In practical production, Kanazawa gold leaf products often vary in gold content, with several alloy elements like silver and copper (Cu). Notably, the Cu content in these products remains extremely low, approximately one atomic percent. To investigate the significance of such a low component, we analyzed both pure gold leaf and No.4 gold leaf using energy-dispersive X-ray spectroscopy (EDS) coupled with TEM. Our findings indicate that the No.4 gold leaf does not exhibit substantial changes in microstructure due to the presence of alloying elements from the pure gold leaf. However, EDS data analysis suggests that an increase in copper content significantly reduces the activity of the (011) slip system. Consequently, maintaining a low copper alloy content appears crucial for enabling the processing of gold leaf to achieve extremely thin thicknesses, as low as around 200nm.

In the Kanazawa area, materials other than gold are also thinned using the hammering process. Previous studies have reported that aluminum (Al) leaf exhibits a similar (001) texture, as indicated by XRD results. To further explore this phenomenon, we conducted experiments using EBSD and UHV-TEM. The microstructure of the Aluminum leaf was significantly different from that of the gold leaf. Some regions displayed recrystallized features, while other areas retained dislocation structures. Additionally, the texture peaks of the Al leaf revealed two distinct orientations, <110> {001} and

<100> {001}. We hypothesize that Al's lower melting point, approximately half that of gold, results in a significantly lower recrystallization temperature, enabling dynamic recrystallization during the hammering process.

Key words: Gold leaf; TEM; EBSD; the non-octahedral slip system; SFE.

CONTENT

Chapter1 Background

1. 1 Kanazawa Gold Leaf

1.1.1 Introduction

Kanazawa gold leaf is a traditional Japanese material renowned for its exceptional thinness, brilliant luster, and intricate hammering techniques, originating from Japan and named after the city, which has been refined over centuries. The meticulous packing and hammering process reduces gold to submicron thickness, with modern methods achieving as little as 0.1 μm. Historically, Kanazawa gold leaf has been widely utilized in artistic, architectural, and religious applications. Due to its extreme thinness and unique properties, it has also garnered attention from materials scientists.

Previous studies on Kanazawa gold leaf and other metal foils, such as aluminum leaf, primarily focused on their crystallographic texture and mechanical properties. Prof. Kitagawa indicates that during the deformation process of hammering, both gold and aluminum leaf tend to develop a stable {001} texture [1, 2]. The evolution of gold leaf's crystal orientation has been analyzed using X-ray diffraction (XRD) [3]. As shown in Figure 1, initially, the (011) plane texture is dominant; however, as the gold leaf becomes thinner (approximately 300 nm), the texture shifts significantly toward the

{001} plane. This transformation is hypothesized to be driven by cross-slip activation under severe deformation.

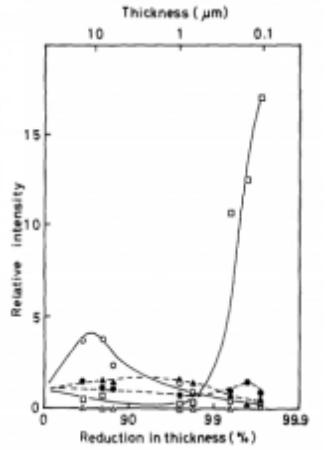

Figure 1. Variation of X-ray diffraction intensity of crystal planes as a function of thickness. The markers mean planes; □(001), ○(011), ▲(111), △(012),●(013) [3].

Despite being one of the oldest, well-known severe plastic deformation (SPD) techniques for material thinning, the Kanazawa gold leaf technique has received limited recent scientific attention. This study aims to investigate the microstructural characteristics of Kanazawa gold leaf using electron backscatter diffraction (EBSD) and transmission electron microscopy (TEM), with a particular focus on specimens thinner than 1 μm in thickness.

1.1.2 The production progress of gold leaf

The Kanazawa gold leaf has three main production processes (figure 2) [4].

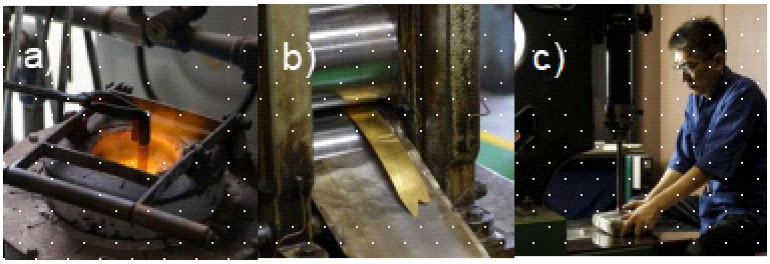

Figure 2.a) Melt the metal. b) Rolling the alloy block to reduce thickness. c) Harming progress for Kanazawa gold leaf.

(1) Formulation and melting

Actually, for the Kanazawa gold leaf industry, the material is not limited to pure gold but also includes gold alloys and other metals (Table 1). In our study, we selected sample No. 4. For making such gold leaf, the first step involves melting gold with a minute amount of silver and copper. The powders of gold, silver, and copper were added to a melting pot maintained at 1300°C [5]. The melt will be completed after waiting 10-15 minutes. The mixed metal solution is poured into a mold to form the desired shape.

	No.5	NO.1	NO.2	NO.3	NO.4	Three step color	watercolor
Gold(at%)	97.3	94.7	93.4	91.8	89.6	62.8	43.2
Silver(at%)	0.9	2.4	4.6	6.2	8.5	37.2	56.1
Copper(at%)	1.8	2.9	2.0	2.0	1.9	0	0

Table 1: the types of the gold leaf in Kanazawa area with the alloy element atom percentage [4].

(2) Rolling out

The alloy was rolled out in the pressure roller to a long strip. After repeating the process 20 times, the strip becomes approximately 40 μm thin. Then, the strip needs to be cut into 6cm squares.

(3) Packing and hammering

In each hammering stage, as shown in Figure 3, the gold sheets are alternately stacked with washi paper (also known as hammering paper) in a mille-feuille-like structure, which is then wrapped in leather. It's worth noting that several types of washi paper exist. As the gold foil becomes thinner, the paper must be replaced multiple times. With the decrease in the thickness of the gold foil, the friction coefficient of these different types of washi paper gradually reduces. The first hammering stage minimizes the thickness from 40 μm to approximately 1 μm. This process is conducted using an 80 mm diameter hammer, striking the gold sheet at a rate of 400 strokes per minute. After approximately 30,000 hammer strikes, the gold reaches a thickness of 1μm.

The second hammer stage reduces the thickness from 0.7 μm to approximately 0.1 μm. In this step, a smaller hammer with a diameter of 40 mm is employed, striking the gold at a rate of 700 strokes per minute. After

around 10,000 hammer strikes, the package is opened, allowing the temperature inside to return to room temperature. Following the hammering and opening process, which is repeated 15 times (resulting in approximately 150,000 strokes), the Kanazawa gold leaf can achieve a thickness of around 0.1 μm.

These hammering processes are illustrated in Fig. 2. The second stage involves finer processing, characterized by two key factors: (i) during the second hammering stage, the covering leather is periodically unwrapped every five minutes (open-package process) to allow internal temperatures to return to room temperature; (ii) washi paper, used as a connection layer with the gold sheet, is frequently replaced due to its gradual smoothing as the gold leaf thins [4].

1.2 Plastic deformation of FCC metal structures

The processing of Kanazawa gold leaf primarily demonstrates a plastic deformation process. Gold and gold alloys, with a small additional percentage of an element, are typical face-centered cubic (FCC) metals that undergo significant dislocation activity during deformation. This phenomenon plays a crucial role in how the material behaves during processing [6, 7].

1.2.1 Dislocation

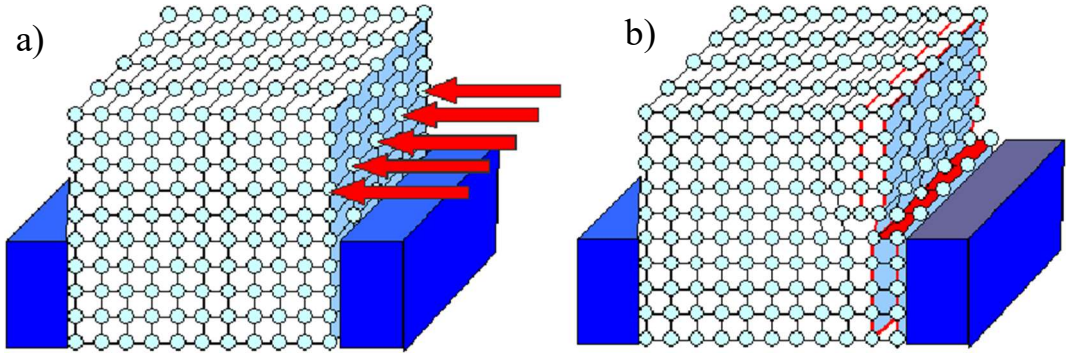

Figure 3.a) the force act at a perfect crystal; b) with the influence of the force a line of atoms glided and format a dislocation

At the onset of plastic deformation, dislocations — one-dimensional line defects within crystals — begin to form within the crystal structure. These dislocations distort the region around the dislocation line, disrupting the periodic arrangement of atoms and the crystal's lattice structure. This distortion creates internal stress within the material, effectively storing energy in the form of dislocation interactions [8, 9].

Dislocations consist of a core [10], which is the region of most excellent distortion, and a dislocation line, which represents the boundary of the slip within the crystal (Figure 4). The core is the location where atomic bonds undergo the most disturbance, and the dislocation line demarcates the path along which the dislocation propagates [11].

To quantify the magnitude and direction of lattice distortion caused by a

dislocation, researchers utilize the Burgers vector (b) [12]. In a perfect crystal (Figure 5a), a closed loop around the lattice returns to its starting point. In contrast, in a crystal with a dislocation (Figure 5b), the same loop fails to close due to the distortion present. The magnitude and direction of the discrepancy between the starting and ending points define the Burgers vector.

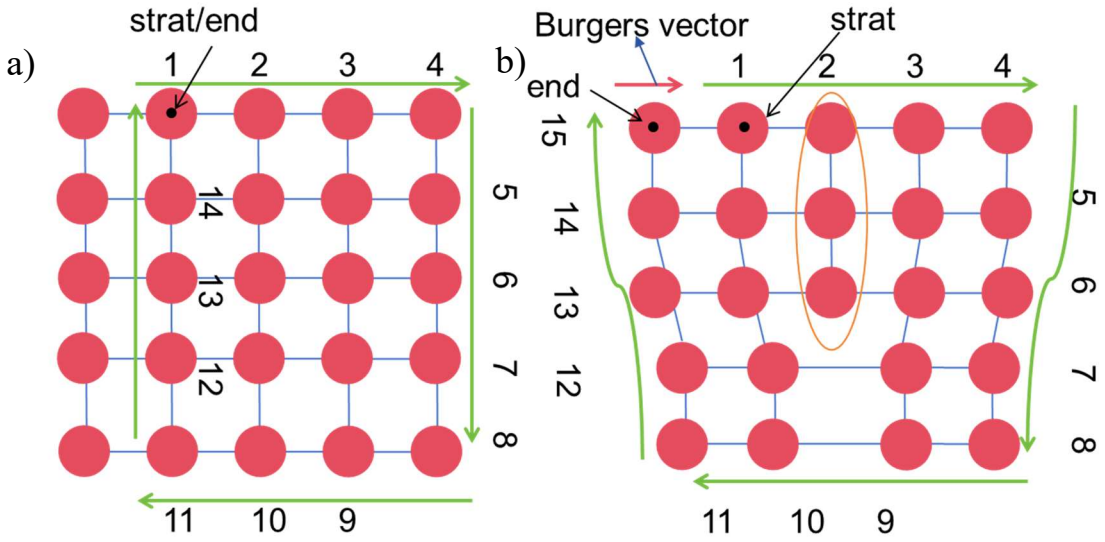

Figure 5. a) Perfect crystal b) When a dislocation in the crystal shows a burgers vector.

Based on the relative orientation of the Burgers vector and the dislocation line, dislocations can be categorized into three types:

Edge dislocations occur when the dislocation line is perpendicular to the Burgers vector [13]. Screw dislocations arise when the dislocation line is parallel to the Burgers vector [14]. Mixed dislocations are those in which the dislocation line is neither fully perpendicular nor parallel to the Burgers

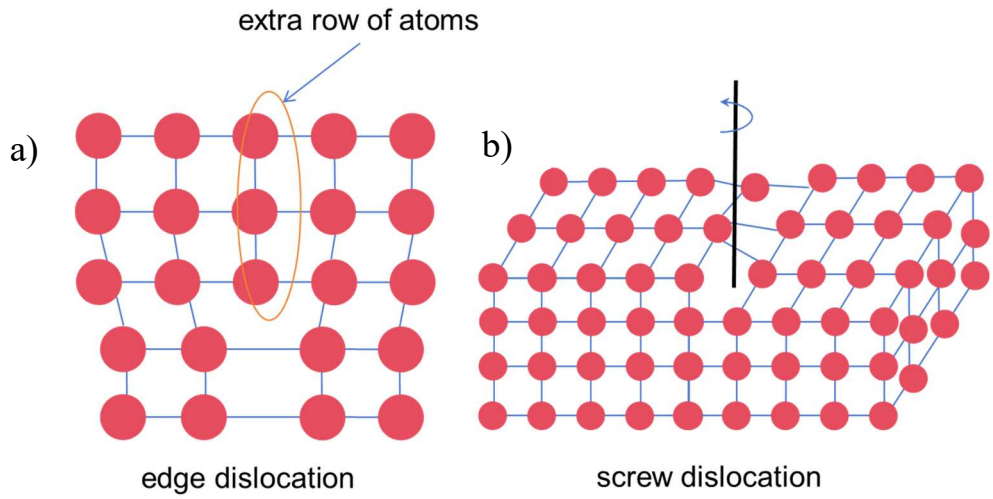

Figure 6. a) Edge dislocation b) Screw dislocation.

vector (Figure 6).

1.2.2 Slip of dislocation &Slip system

Plastic deformation in materials occurs when the applied stress exceeds the yield strength. Consequently, the material undergoes permanent deformation and cannot return to its original shape once the stress is removed. At the atomic level, this deformation occurs through the movement of dislocations along the crystal lattice planes. When stress is applied, dislocations slide, causing the permanent displacement of atomic layers. This mechanism is known as slip, which is the process by which atomic layers slide past each other along specific crystallographic planes referred to as slip planes [15].

Slip Systems

Dislocation motion refers to the movement of dislocations from one lattice position to another across a distance equal to the lattice spacing [16]. In FCC crystals, slip generally occurs along the {111} closest-packed planes and in the <110> closest-packed directions (see Figure 7) [17]. Consequently, movement along these planes and directions is recognized as the slip system with the lowest energy cost and shortest distance, with the {111} < 110> slip system being particularly favored for FCC crystals.

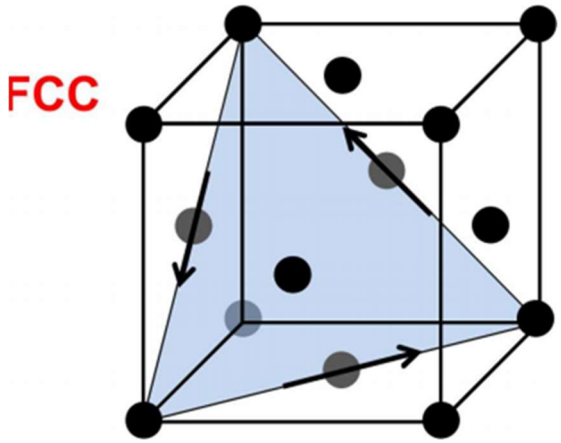

Figure 7. the bule tangle shows the {111} plane as the closest-packed planes and the arrow as the <110> closest-packed direction.

Shear Stress

Imagine a single crystal with a cross-sectional area A0 subjected to an external compressive force F0, which serves as an initiating force for deformation. To trigger shear in the atomic planes, a parallel force component, F|| , must be present along the slip plane (see Figure 8a) [18]. In contrast, a perpendicular force component F ⊥ only compresses the layers

without causing slip.

When the slip plane is inclined at an angle α to the tensile axis, F_0 decomposes into:

$$\text{shear force: } F_{\parallel}=F_0 \cdot \cos(\alpha) \quad (1)$$

$$\text{normal force: } F_{\perp}=F_0 \cdot \sin(\alpha) \quad (2)$$

For deformation to occur, the shear force F|| must be strong enough to activate the slip plane. In the case of angle device control, a four-alpha device control is insufficient; F|| remains low, making the force possibly inadequate for deformation. On the other hand, as α increases, the shear force initially rises. However, the area of the slip plane A also expands, which amplifies the binding forces between the atomic planes due to the compressive normal force F⊥. This additional normal force can prevent slip by increasing the shearing resistance.

This behavior is similar to a hook-and-loop fastener: if the shear force is inadequate, the materials remain intertwined. By increasing the force, the contact area also expands. In this scenario, slipping may not occur because the shear stress remains insufficient.

Shear stress is defined as the effective force applied per unit area.

$$\tau = \frac{F_{\parallel}}{A} \quad (3)$$

In this case, the value relies on α as indicated in equation (1), while the slip plane area A is defined by:

$$A = \frac{A_0}{\sin(\alpha)} \quad (4)$$

Schmid Factor and Critical Shear Stress

The slip initiates when the resolved shear stress τ on the slip system reaches a critical threshold [19]. The applied normal stress σ includes a component that acts along both the slip direction and the slip plane, as indicated by [20]:

$$\tau = \sigma \cdot \cos\phi \cdot \cos\lambda \quad (5)$$

Where τ is the resolved shear stress, σ is the applied everyday stress, and ϕ is the angle between the applied stress direction and the normal to the slip plane (the slip plane's normal vector). λ is the angle between the applied stress direction and the slip direction (i.e., the slip direction vector) (Figure 8b).

The Schmid factor (m) represents the geometric alignment and is defined as follows:

$$m = cos\phi \cdot cos\lambda \quad (6)$$

So that:

$$\tau = \sigma \cdot m \tag{7}$$

This relationship indicates that the efficiency of applied stress in causing slip relates directly to the magnitude of m. A higher Schmid factor is associated with improved alignment of stress with the slip system, enhancing the likelihood of slip. With a high m, the resolved shear stress τ increases for a specific applied stress σ, which lowers the critical shear stress τc necessary

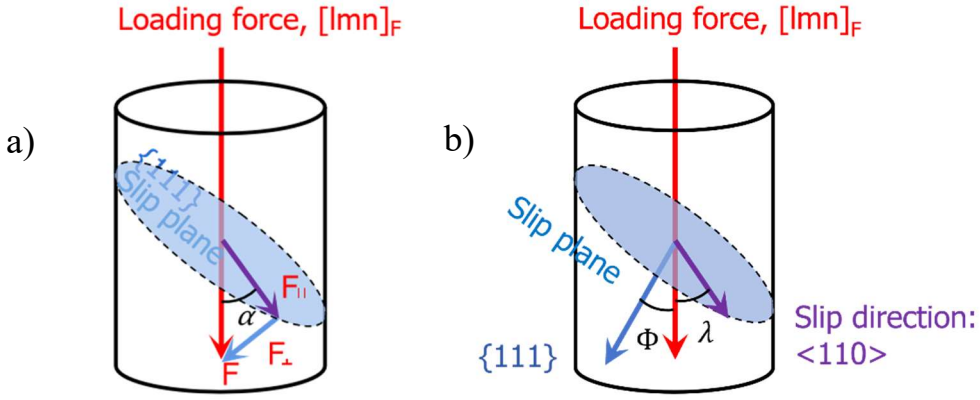

Figure 8. the relationship between slip plane, slip direction and loading force of a) shows the sheer force; b) shows the Schmid factor.

For initiating a slip.

A larger m signifies increased stress on the slip systems, aiding slip initiation. When $\tau \geqslant \tau c$ (the critical shear stress), the material undergoes plastic deformation. The τc value is influenced by bonding strength and lattice structure. Thus, analyzing σ, m, and τc is essential for predicting material deformation.

Peierls Valleys

In the processing of real metals, such as hammering Kanazawa gold leaf, each crystal contains multiple dislocations and varying structural features. During deformation, these dislocations travel along the path of least resistance, known as the Peierls Valley [21]. These valleys represent stable atomic configurations that are minimally disturbed. Ideally, the spacing of these valleys aligns with the lattice spacing in the closest-packed direction (Figure 9(a)). However, the lowest energy path may deviate due to dislocations resulting from altered atomic arrangements. Consequently, the energy cost for moving a single dislocation in this plane is no longer equal to the ideal scenario (Figure 9(b)). In FCC metals, such as gold leaf, if the {111} planes are densely populated with dislocations, they may no longer serve as the slip plane with the lowest energy cost. Instead, some dislocations may propagate into non-octahedral planes, such as the {110} planes, to facilitate further slip.

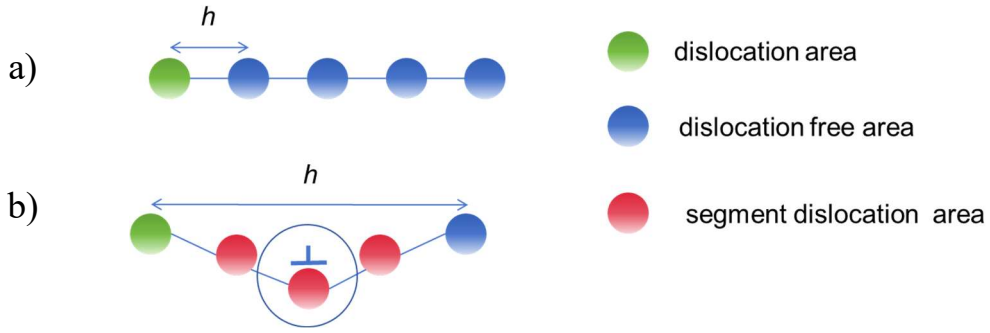

Figure 9.a) is the Perierls valley in a crystal with a low density of dislocation. b) is the Perierls valley in a crystal with a high density of dislocation, the h is much longer than it in a.

1.2.3 Slip and Rotation

Rotation and Plastic Deformation in Single Crystals

The slip associated with dislocation typically indicates the onset of plastic deformation. In this section, we utilize single-crystal examples to circumvent the complications introduced by grain boundaries in polycrystalline materials. During plastic deformation, the rotation of the single crystal is affected by the activation of the slip system. Here, we explore the relationship between slip and rotation in response to stress applied in various directions.

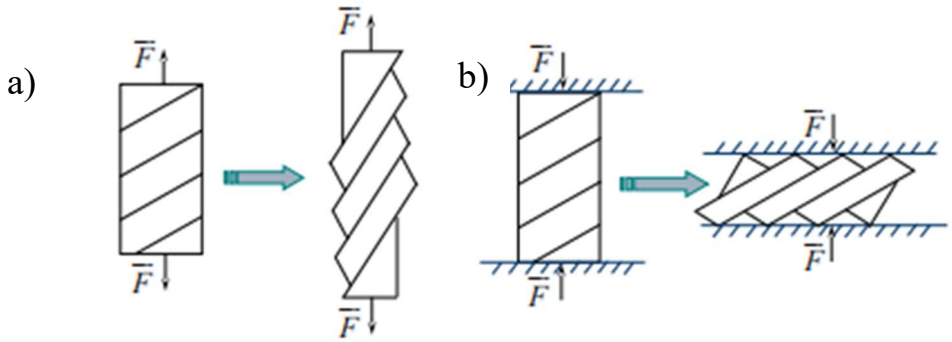

Figure 10.a) for stretching, the direction of slip seeks to turn (converge) towards the stretching axis; b) for compression, the slip surface tries to turn (converge) to the compression surface during slip surface.

Response to Tensile Force

When a crystal is subjected to tension, it elongates along the direction of the applied force. With both ends clamped, rotation is restricted, keeping the tensile axis fixed. As a result, a crystal experiences simultaneous slip and limited rotation. During deformation, the crystal's lower internal activation energy prevents changes at the top and bottom sides due to clamping. Thus, with the tensile axis stable, rotation causes the slip direction <110> to align more closely with the tensile axis, thereby enhancing alignment with the shear stress direction and reducing τ_c, which promotes slip activation (Figure 10a).

Response to Compressive Force

Under compression, the sample ends remain in fixed contact, which forces

the crystal to reorient internally. It cannot rotate globally to align with an ideal load direction because the boundaries are immovable. Instead, the internal structure aligns along the {111} plane, a close-packed plane that effectively withstands compression (Figure 10b) [25]. The compressive load is distributed through this dense atomic plane, minimizing strain. Consequently, slip planes adjust to stabilize the crystal under compressive loading.

In polycrystalline materials, slip-induced grain rotations during compression have a significant influence on crystallographic orientations and contribute to the development of texture.

1.2.4 Plastic Deformation Under Compression and Slip System Activation

In this study, we focus on compressive stress, specifically the downward force exerted by hammering. We use a single crystal to simplify our analysis, as grain boundaries in polycrystals introduce additional complexity. The activation and sequence of slip systems dictate the crystal rotation under stress.

Primary Slip System Activation

For example, we let the compression plane be as shown in the red area (Figure 11a). When compressing along [123], which is located between the

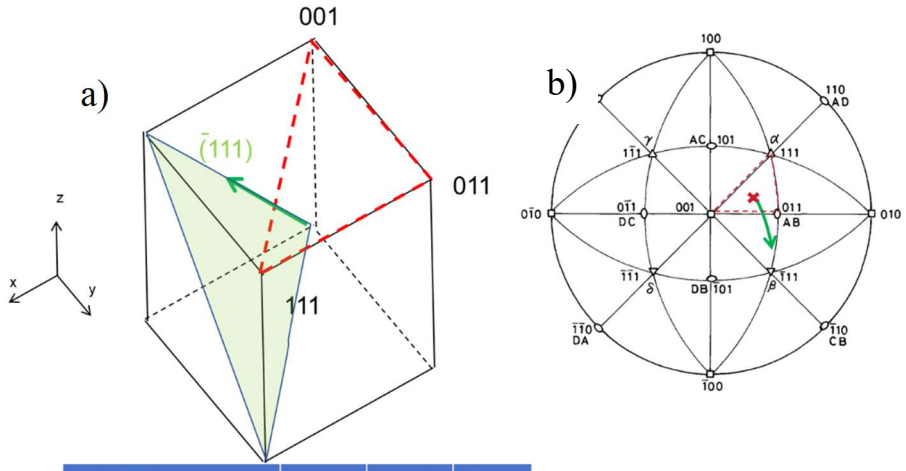

[123]Slip system	cosφ	cosλ	Ω
$(\bar{1}11)$ – [101]	0.61	0.76	0.46
(111) – $[\bar{1}01]$	0.92	0.38	0.35

Figure 11.a) at the compress axis from [123], the slip system shown in the green tangle will be start cause of the highest Schmid factor; b) as the slip system start the compress axis will rotate with the green arrow, to the [001]-[011] line.

crystallographic orientations [001], [011], and [111]. Under such a compressive condition, the $(\bar{1}11)$-[101] slip system has the highest Schmid factor. Such a slip system acts as the primary slip system, allowing for rotation in the crystal along the $[\bar{1}11]$ direction. The stress alignment maximizes the resolved shear stress required for slip, causing the compression axis to rotate along the [001]-[011] direction toward the [012] direction [26].

Secondary slip system

With continued hammering, the rotation causes the compress axis to align in the [012] direction. Two slip systems exhibit equally most significant Schmid factor (figure 12). Both systems become active, termed secondary slip, producing two distinct rotation tendencies [27]. In this case, there will be two forces rotating the sample: one is to $[\bar{1}11]$, and the other is to [111]. Combining these two forces, the rotation force will align on the [001]-[011] line. With these two types of slip systems, the compressive axis will shift from the [012] direction to the [011] direction along the [001]-[011] line (Figure 12b). In this case, a (011) texture is formatted.

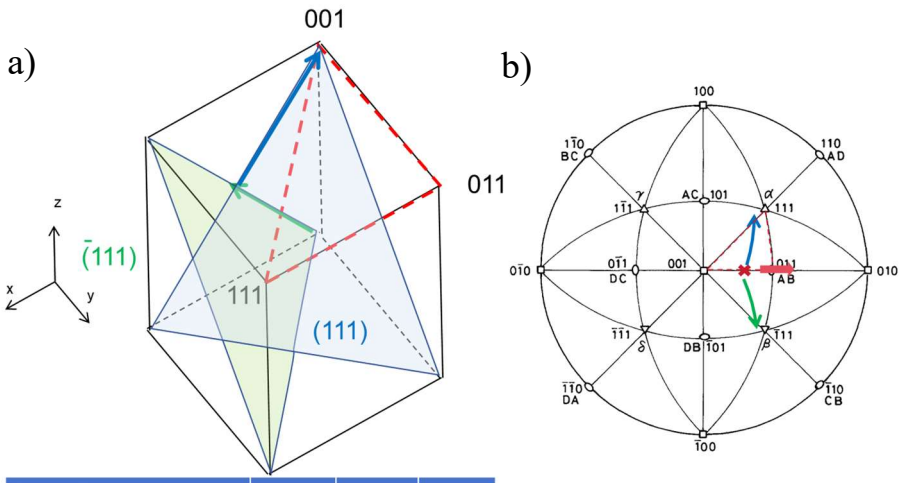

[012]Slip system	cosφ	cosλ	Ω
$(\bar{1}11) - [101]$	0.77	0.63	0.49
$(111) - [\bar{1}01]$	0.77	0.63	0.49

Figure12.a) at the compress axis from [012], the slip systems shown in the green and blue tangles will be start cause of the highest Schmid factor; b) as the slip system start the compress axis will rotate with the red arrow which combining with the two arrow along the [001]-[011] line.

Dislocation interaction

When multiple slip systems are active, dislocations in different planes may cross and interact. These interactions often lead to reactions that result in a general reduction of energy [28]. The standard expression for dislocation energy is:

$$E \approx \frac{1}{2} G b^2$$

Where E represents elastic energy per unit length of dislocation, G denotes the shear modulus, and b is the Burgers vector. Since G is constant, a longer Burgers vector b for a dislocation requires more energy for the interaction of dislocations. This can result in the generation of dislocations with smaller Burgers vectors, thereby reducing the system's energy.

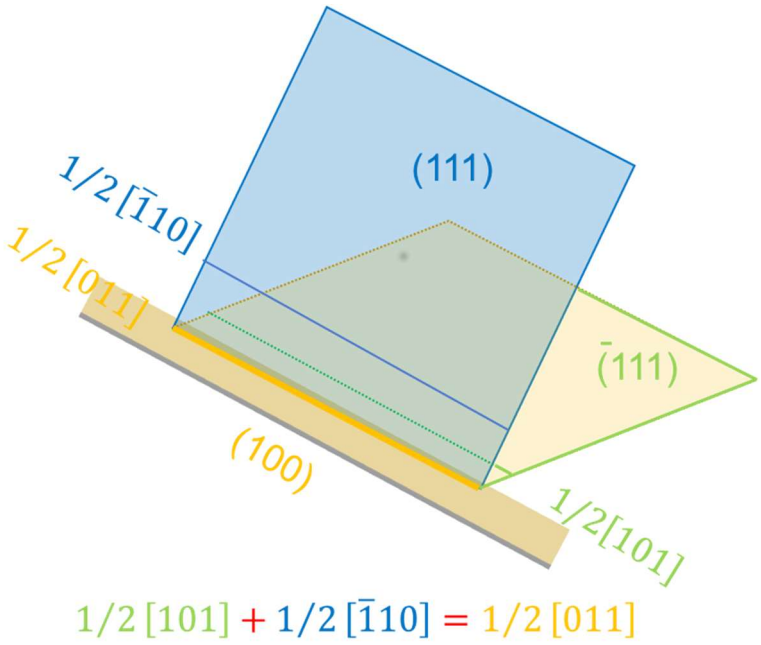

Figure 13. Dislocations from the secondary slip system can meet and interact. A so-called Lomer lock structure formatted at the edge of the planes.

Upon secondary slip, two dislocations within the two slip planes may meet and interact at the boundary between the two planes. Such interaction can reduce dislocation energy by up to ~50% (Figure 13), creating a new dislocation with a Burgers vector of 1/2[011]. As such, dislocation no longer belongs to the (111) or ($\bar{1}$11)slip planes but lies on the (100) plane. Usually, for FCC material, (100) planes are not a type of basic slip planes, which is unavailable for dislocations to slip. Such dislocation is named as Lomer lock—a sessile dislocation. Some researchers have found that the accumulation of Lomer locks increases dislocation density, a process known as forest hardening [29,30].

1.2.5 Cross-slip and Stacking fault

After the secondary slip system is activated, some of the dislocations may interact as a Lomer lock, contributing to the formation of frost hardening. In this case, the average mobility of dislocations may be reduced. Because the dislocation density becomes so high, further slip on the same planes for the secondary slip systems becomes increasingly complex, compelling dislocations to adjust their behavior to accommodate the applied stress.

Partial dislocation

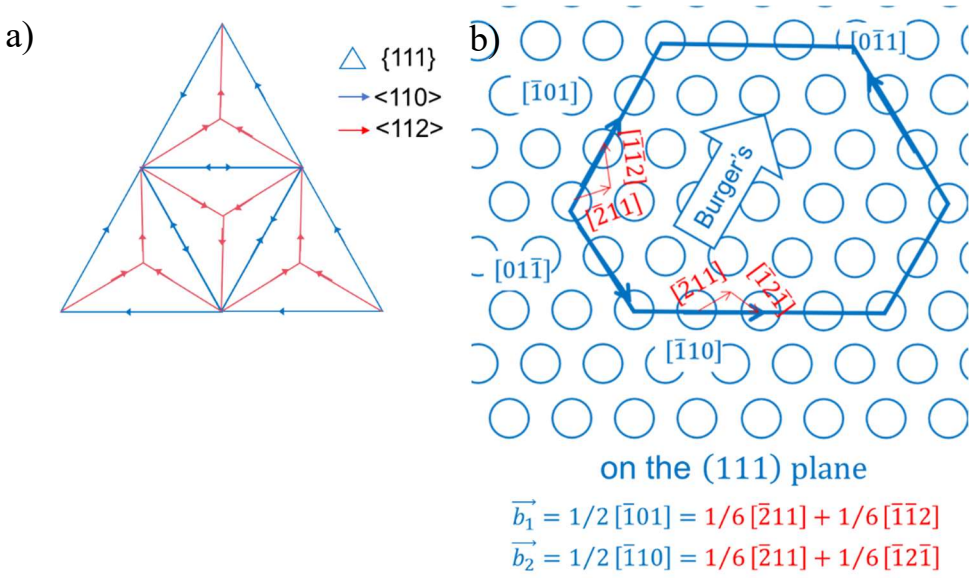

Figure 14.a) Shows possible slip directions within the {111} plane. The arrows represent different dislocation paths, with blue arrow for perfect dislocations and the red arrow for the partial dislocation; b) Shows the hexagonal close-packed arrangement of atoms on the {111} plane. The blue arrow labeled "Burgers" shows the Burgers vector ($\vec{b}$). The dislocations can decompose into partial dislocations, as indicated by the equations, which show how perfect dislocations break into partials.

A key adaptation is dissociation: a perfect dislocation can split into two partial dislocations. For example, a perfect dislocation with Burgers vector $1/2[\bar{1}01]$ may decompose into two Shockley partials with vectors $1/6[\bar{2}11]$ and $1/6[\bar{1}\bar{1}2]$ [31]. This dissociation enables the dislocation to shift out of the {111} plane into the {112} plane. As a new way to slip, this enables continued slip when it is difficult to activate within the {111} planes [32].

Stacking Faults

When a perfect dislocation dissociates into partials, it results in the formation of a stacking fault, disrupting the typical close-packed atomic stacking sequence in FCC crystals. Typically, the {111} layer stack is an ABCABC pattern. A stacking fault may alter the pattern to something like ABCABABC (Figure 15) [33, 34].

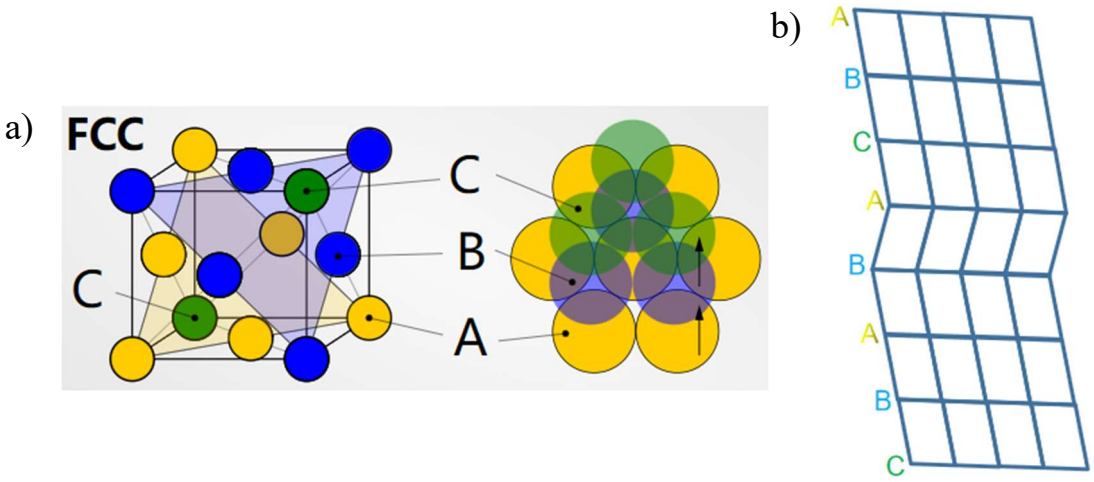

Figure 15.a) A, B, C marked with three types of color as three different types of {111} planes in FCC crystal; b) when one of the {111} planes change, such structure is so-called stacking fault.

Cross-slip

For instance, a screw dislocation with Burger's vector of 1/2[101] may slip

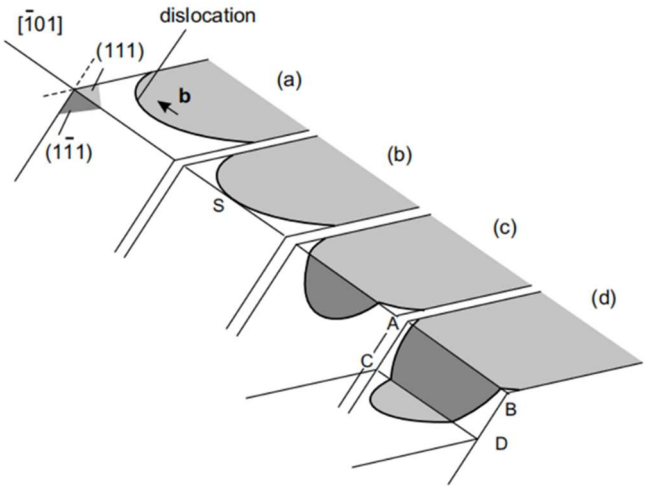

Figure 16. cross slip in the FCC metal.

in the plane initially as acting applied shear stress is shown in Figure 16. If the local stress field shifts in favor of motion along the $(1\bar{1}1)$ plane, cross-slip can occur at the point marked S in Figure 16, thereby allowing the dislocation to change its slip plane [35] [36]. This capability for cross-slip provides a unique flexibility in maintaining deformation under complex loading conditions—a property not shared by edge or mixed dislocations, which are constrained to a single slip plane [37, 38].

Stacking fault energy and cross-slip

The stacking fault energy (SFE), denoted as $\gamma_{SFE,}$ measures the energy per

unit area associated with the formation of a stacking fault. SFE strongly influences a material's ability to cross-slip. In high SFE metals (e.g., aluminum), this means the energy cost for forming an SF is high. And the dislocations avoid dissociating to partial dislocations. In this case, many of the dislocations still have a Burgers vector of 1/2[011] as a perfect dislocation. The screw dislocations more preferred to cross slip. In low SFE metals (e.g., copper), the energy cost to format SF is low. Most of the perfect dislocations are preferred to dissociate to partial dislocations. On the other hand, no more ideal dislocation chooses to move across the slip plane. The ability to cross-slip is low.

1.2.6 Annealing effect： recovery and recrystallization

Recovery Process

As deformation continues, the dislocation density increases, and the spacing between dislocations decreases. This means that the interaction between the dislocations becomes easier. Usually, dislocations with the same Burgers' vectors are referred to as like-sign dislocations, while those with opposite Burgers' vectors are called opposite-sign dislocations. If the spacing between dislocations is minor, like-sign dislocations (Figure 17b) repel each other due to similar stress fields. In contrast, opposite-sign dislocations (figure 17a)

attract each other due to opposing stress fields, sometimes annihilating one another. However, these forces can be modest, insufficient to overcome energy barriers between atoms. During deformation, raising the temperature or pressure can provide sufficient energy for dislocations to interact. Finally, the opposite-sign dislocations will annihilate each other. The process of decreasing the density of dislocations through the interaction of opposite-sign dislocations is known as recovery.

In gold, initial recovery may start near room temperature but generally continues up to approximately 340°C, corresponding to a temperature of about 0.1–0.2 Tm (melting temperature). At these temperatures, dislocations can climb out of their slip planes and annihilate. Above approximately 0.3 Tm, high-temperature recovery promotes the formation of low-angle grain boundaries (LAGBs), resulting in polygonized subgrain structures. Y-junctions form where multiple LAGBs intersect, indicating the onset of stable polygonization [39][40].

`Relationship Between Recovery and Recrystallization

Recrystallization Process

Above ~0.5 T_m, recrystallization ensues with the nucleation and growth of new, low-dislocation-density grains, separated by high-angle grain boundaries (HAGBs) [41]. Recrystallization typically proceeds in three stages (Figure 18):

1. **Nucleation**: Small, nearly dislocation-free regions act as nuclei for new grains.

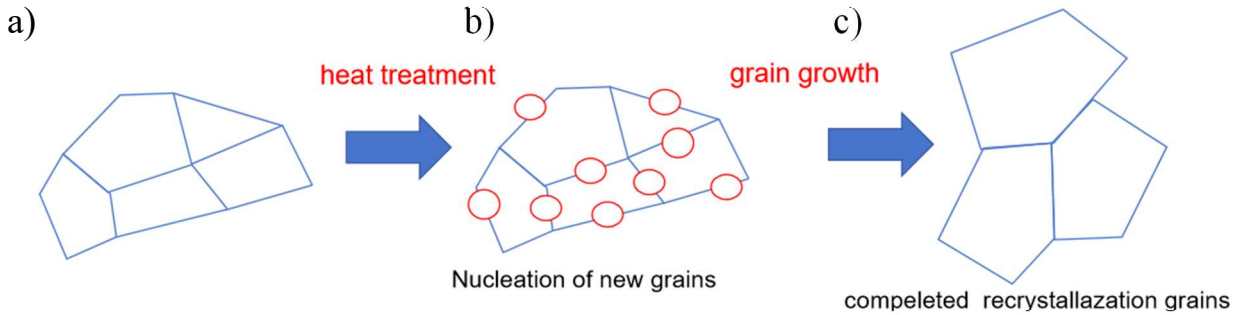

Figure 17.a) some grains have significant deformation after processing; b) with the heat treatment, among the grains some new grains nucleate; c) after the grain growth the new grains become larger and with no defects.

2. **Grain Growth**: The new grains expand via boundary migration, absorbing high-energy dislocations and replacing deformed grains.

3. **Complete Recrystallization**: Eventually, all original deformed grains are replaced by newly formed grains with relatively few dislocations, resulting in a fine-grained, uniform structure [41].

Relationship Between Recovery and Recrystallization

Recovery and recrystallization both reduce internal stress by lowering dislocation density, but their structural outcomes differ. During recovery, dislocations mainly rearrange or annihilate; during recrystallization, entirely new grains form[42]. Gradual heating may begin with recovery and then transition to recrystallization at higher temperatures. Rapid heating beyond the recrystallization threshold can skip recovery, proceeding directly to recrystallization [43].

1.3 Texture evaluation

As the plastic deformation part describes, every single crystal within the metal material is highly preferred in a particular orientation. Previous studies on Kanazawa gold leaf revealed that texture evolution occurs during different stages of processing. Initially, during the first hammering stage, the {011} texture was observed, but it transitioned to the {001} texture in the secondary hammering stage.

In the case of the hammering process of Kanazawa gold leaf, the primary factors influencing texture formation may be two parts:

Deformation Texture

During the plastic deformation of polycrystalline materials, the activation of

slip systems for dislocations occurs, as coordination between neighboring grains during deformation results in a gradual rotation of grains toward the deformation direction. For example, during rolling, grains tend to align their slip planes with the rolling direction. Additionally, the hammering process involves a primary stress source, as the downward force of the hammer. The texture will change according to the direction of the hammering. For the main deformation textures, there are several types:

- **Rolling Texture**: In typical rolling processes, the rolling direction as RD corresponds to a specific crystallographic direction as <uvw>, the normal direction corresponds to the plane normal {hkl} as ND, and the transverse direction is oriented within the plane, perpendicular to rolling. Typical rolling textures for face-centered cubic (FCC) metals during cold rolling include Brass texture ({110}<112>), commonly observed in low stacking fault energy (SFE) FCC metals such as α-brass. On the other hand, the Copper texture ({112}<111>) is typical in high SFE FCC metals, such as pure copper. Research indicates that {001}-related textures are generally unstable and rarely form as final textures during cold deformation.
- **Shear Texture**: Shear textures may form due to the limited size and shape of the hammer used in processing, specifically related to the

stress state and interaction with the material surface during deformation.

Annealing Texture

Annealing textures form during heat treatments, including recrystallization, recovery, or grain growth. As during the hammering process of the Kanazawa gold leaf, the local temperature between the washi paper and the gold leaf may increase. It is difficult to say that no influence of recovery or recrystallization can occur during the hammering process. The primary mechanisms for the formation of the annealing textures include:

- **Recrystallization Nucleation Orientation**: During recrystallization, some local areas will nucleate new grains due to the high stored energy in the deformed matrix, such as grain boundaries or shear bands with high dislocation densities. The orientations of these new grains are usually related to the deformation texture of the parent material and have a highly preferred orientation. For instance, during the annealing of deformed aluminum, the new defect-free grains may inherit deformation textures or form a new cube texture {100} <001>.
- **Preferential Grain Growth Orientation:** Grain boundary migration

is influenced by orientation differences between grains. Grains with specific orientations, either due to lower interfacial energies or higher migration rates, tend to grow preferentially, leading to annealing textures. An example is the Goss texture {110}<001>, which is frequently observed during silicon steel annealing due to its beneficial magnetic anisotropy, thereby reducing iron loss.

1.4 Purpose

In this study, we investigate the distinctive plastic deformation mechanisms and the evolution of crystallographic texture that underlie the traditional hammering process of Kanazawa gold leaf. We aim to elucidate the microstructural changes at the nanoscale, focusing on how stacking-fault energy (SFE), slip system activation, and microstructural factors drive deformation. By integrating advanced analytical methods—such as TEM and EBSD—we endeavor to clarify how Kanazawa gold leaf, an ancient ultra-thin material, achieves its remarkable properties.

1.5 Summary

Kanazawa gold leaf is an extraordinary historical material, distinguished by its extreme thinness and striking metallic sheen, achieved through a careful packing and hammering method. In this section, we reviewed texture

evolution, dislocation interactions, stacking faults, and cross-slip, but most of these concepts are based on studies of bulk materials. Here, we question whether these same processes occur in ultrathin gold leaf and whether unique phenomena arise due to such extreme thickness.

Overall, we have outlined the production background of Kanazawa gold leaf and key facets of plastic deformation in FCC metals. This provides a platform for further in-depth analysis of its microstructure using TEM, EBSD, and other advanced techniques.

References

[1] K. Kitagawa and K. Tanimura, “Texture of gold leaf fabricated by hammering,” *Scripta Metallurgica*, vol 20, no. 11, pp. 1511–1514, Nov. 1986, doi: 10.1016/0036-9748(86)90385-6.

[2] K. Kitagawa and K. Tanimura, “Texture of aluminum leaf fabricated by hammering,” *Scripta Metallurgica*, vol. 20, no. 5, pp. 673–676, May 1986, doi: 10.1016/0036-9748(86)90488-6.

[3] K. Kitagawa, “On the development of the (001) texture of gold leaf fabricated by hammering,” *J Mater Sci*, vol. 23, no. 8, pp. 2810–2814, Aug. 1988, doi: 10.1007/BF00547454.

[4] K. [Kanazawa Inst. of T. "Kitagawa Ishikawa (Japan). Faculty of Engineering]", “Skill and wisdom of craftsman of gold leaf; Kinpaku shokunin no waza to chie,” [], vol. 99, Jan. 1996.

[5] A. Takami, H. Kurita, and S. Koda, “Laser-Induced Size Reduction of Noble Metal Particles,” *J. Phys. Chem. B*, vol. 103, no. 8, pp. 1226–1232, Feb. 1999, doi: 10.1021/jp983503o.

[6] J. Lubliner, *Plasticity theory*. Courier Corporation, 2008.

[7] A. Marcano, “Fundamentals of Nonlinear Optics,” *Physics Today*, vol. 65, no. 10, pp. 56–57, 2012.

[8] D. Mendeleev, “Part of a series on the”.

[9] P. M. Anderson, J. P. Hirth, and J. Lothe, *Theory of dislocations*. Cambridge University Press, 2017.

[10] V. Volterra, “Sur l’équilibre des corps élastiques multiplement connexes,” *Ann. Sci. École Norm. Sup.*, vol. 24, pp. 401–517, 1907, doi: 10.24033/asens.583.

[11] G. I. Taylor, “The mechanism of plastic deformation of crystals. Part I.—

Theoretical," *Proceedings of the Royal Society of London. Series A, Containing Papers of a Mathematical and Physical Character*, vol. 145, no. 855, pp. 362–387, Jan. 1997, doi: 10.1098/rspa.1934.0106.

[12] D. Callister William, *Fundamentals of Materials Science and Engineering*. John Wiley, 2008.

[13] R. Reed-Hill and R. Abbaschian, "Physical metallurgy principles, PWS Publ," *Comp., Boston*, vol. 853, 1994.

[14] F. Edition and M. F. Ashby, "Material Selection in Mechanical Design," 2011.

[15] W. D. Callister Jr and D. G. Rethwisch, *Fundamentals of materials science and engineering: an integrated approach*. John Wiley & Sons, 2020.

[16] W. Soboyejo, *Mechanical properties of engineered materials*. CRC press, 2002.

[17] K. J. Van Vliet, "3.032 Mechanical behavior of materials," *available from internet: https://ocw. mit. edu/courses/materials-science-and-engineering/3-032-mechanical-behavior-of-materials-fall-2007/lecture-notes/lec1. pdf*, 2006.

[18] A. D. McNaught and A. Wilkinson, *Compendium of Chemical Terminology*, vol. 1669. Blackwell Science Oxford, 1997.

[19] E. Schmid and W. Boas, "Plasticity of crystals," 1950.

[20] G. Gottstein, *Physical foundations of materials science*, vol. 3. Springer, 2004.

[21] W. O. Soboyejo, *Mechanical properties of engineered materials*. in Mechanical engineering (Marcel Dekker, Inc.); 152. New York: Marcel Dekker, 2003.

[22] Z. Wang, I. Beyerlein, and R. LeSar, "Plastic anisotropy in fcc single crystals in high-rate deformation," *International Journal of Plasticity*, vol. 25, no. 1, pp. 26–48, 2009.

[23] V. Deshpande, A. Needleman, and E. Van der Giessen, "Discrete dislocation plasticity analysis of single slip tension," *Materials Science and Engineering: A*, vol.

400, pp. 154–157, 2005.

[24] R. Gröger, V. Racherla, J. Bassani, and V. Vitek, “Multiscale modeling of plastic deformation of molybdenum and tungsten: II. Yield criterion for single crystals based on atomistic studies of glide of 1/2< 111> screw dislocations,” *Acta Materialia*, vol. 56, no. 19, pp. 5412–5425, 2008.

[25] V. Deshpande, A. Needleman, and E. Van der Giessen, “Plasticity size effects in tension and compression of single crystals,” *Journal of the Mechanics and Physics of Solids*, vol. 53, no. 12, pp. 2661–2691, 2005.

[26] I. Karaman, H. Sehitoglu, K. Gall, Y. I. Chumlyakov, and H. Maier, “Deformation of single crystal Hadfield steel by twinning and slip,” *Acta materialia*, vol. 48, no. 6, pp. 1345–1359, 2000.

[27] P. Franciosi, L. Le, G. Monnet, C. Kahloun, and M.-H. Chavanne, “Investigation of slip system activity in iron at room temperature by SEM and AFM in-situ tensile and compression tests of iron single crystals,” *International Journal of Plasticity*, vol. 65, pp. 226–249, 2015.

[28] L. Dupuy and M. Fivel, “A study of dislocation junctions in FCC metals by an orientation dependent line tension model,” *Acta Materialia*, vol. 50, no. 19, pp. 4873–4885, 2002.

[29] T. Tisone, J. Brittain, and M. Meshii, “Lomer-cottrell locks in a Cu-15 at. % Al alloy,” *Philosophical Magazine*, vol. 16, no. 141, pp. 647–650, 1967.

[30] B. Devincre and L. Kubin, “Simulations of forest interactions and strain hardening in FCC crystals,” *Modelling and Simulation in Materials Science and Engineering*, vol. 2, no. 3A, p. 559, 1994.

[31] M. Niewczas and R. Hoagland, “Molecular dynamics studies of the interaction of a/6⟨ 112⟩ Shockley dislocations with stacking fault tetrahedra in copper. Part I: Intersection of SFT by an isolated Shockley,” *Philosophical Magazine*, vol. 89, no. 7, pp. 623–640, 2009.

[32] S. Raujol *et al.*, “Decorrelated movements of Shockley partial dislocations in the γ-phase channels of nickel-based superalloys at intermediate temperature,” *Philosophical Magazine*, vol. 86, no. 9, pp. 1189–1200, 2006.

[33] D. Stegall, M. Mamun, and A. Elmustafa, “The role of stacking fault energy on the indentation size effect of FCC pure metals and alloys,” *MRS Online Proceedings Library (OPL)*, vol. 1424, pp. mrsf11-1424, 2012.

[34] K.-Q. Li, Z.-J. Zhang, L.-L. Li, P. Zhang, J.-B. Yang, and Z.-F. Zhang, “Effective stacking fault energy in face-centered cubic metals,” *Acta Metallurgica Sinica (English Letters)*, vol. 31, pp. 873–877, 2018.

[35] S. Hayakawa, K. Doihara, T. Okita, M. Itakura, M. Aichi, and K. Suzuki, “Screw dislocation–spherical void interactions in fcc metals and their dependence on stacking fault energy,” *Journal of Materials Science*, vol. 54, pp. 11509–11525, 2019.

[36] G. Marnier, C. Keller, and L. Taleb, “Tensile prestrain memory effect on subsequent cyclic behavior of FCC metallic materials presenting different dislocations slip modes,” *International Journal of Plasticity*, vol. 78, pp. 64–83, 2016.

[37] W. G. Nöhring and W. Curtin, “Cross-slip of long dislocations in FCC solid solutions,” *Acta Materialia*, vol. 158, pp. 95–117, 2018.

[38] M. Ahlers, “Stacking fault energy and mechanical properties,” *Metallurgical Transactions*, vol. 1, pp. 2415–2428, 1970.

[39] C. Sellars, “Recrystallization of metals during hot deformation,” *Philosophical Transactions of the Royal Society of London. Series A, Mathematical and Physical Sciences*, vol. 288, no. 1350, pp. 147–158, 1978.

[40] D. Raabe, “Recovery and recrystallization: phenomena, physics, models, simulation,” *Physical metallurgy*, pp. 2291–2397, 2014.

[41] Q. Liu and N. Hansen, “Deformation microstructure and orientation of fcc crystals,” *physica status solidi (a)*, vol. 149, no. 1, pp. 187–199, 1995.

[42] C. Kopezky and L. Kokhantchik, “Evolution of Structure in Deformed Single Crystals of fcc Metals at Heating,” *Kristall und Technik*, vol. 14, no. 11, pp. 1303–1311, 1979.

[43] D. Hughes and W. Nix, “The absence of steady-state flow during large strain plastic deformation of some Fcc metals at low and intermediate temperatures,” *Metallurgical Transactions A*, vol. 19, pp. 3013–3024, 1988.

Chapter 2 Experimental and analysis method

2.1 Transmission electron microscopy (TEM)

2.1.1 The theory of TEM

Resolution in optical microscopy has essentially reached its theoretical limit. Because resolution depends on the wavelength of light, this limitation is often described by the Rayleigh criterion:

$$\delta = \frac{0.61}{\mu \sin \beta} \tag{2.1}$$

where δ denotes the resolution, λ is the wavelength of light, μ is the refractive index, and sinβ is half the lens aperture angle. Because the numerical aperture (μsinβ) cannot exceed 1, the resolution limit remains around half the wavelength of visible light (~300 nm) [1].

In 1924, de Broglie's wave theory established that electrons possess wave-like properties with significantly shorter wavelengths than visible light. This discovery theoretically enabled the development of atomic-scale electron microscopes. In 1932, Ruska et al.. constructed the first TEM, achieving a resolution of ~50 nm [2]. For modern TEM, the correlation between electron wavelength and energy is given by:

$$\lambda \approx \frac{1.22}{\sqrt{E}} \qquad (2.\ 2)$$

Here, λ denotes the electron wavelength, and E is the electron energy, which is principally determined by the accelerating voltage.

E(kev)	λ(Å)
100	0.037
200	0.025
300	0.0196
400	0.0169

Table 2. Wavelength of electrons at different accelerating voltages.

In essence, TEM employs an electron gun to direct a focused electron beam onto an ultrathin specimen. By detecting transmitted and elastically scattered electrons, one obtains an image that reveals atomic-scale features. Advances in higher accelerating voltages now enable the precise imaging of atomic structures. [3] Additionally, various signals (e.g., elastically or inelastically scattered electrons, characteristic X-rays) arise when the beam interacts with the sample. With extra detectors such as Energy-Dispersive X-ray Spectroscopy (EDS) or Electron Energy Loss Spectroscopy (EELS), high-resolution elemental analyses can be performed [4].

2.1.2 Basic components of TEM

A TEM comprises four basic modules: the electron gun, condenser lens system, objective lens, and intermediate and projector lenses (Figure 2).

Electron Gun

The electron gun, which serves as the source of electrons in a transmission electron microscope (TEM), is generally classified into two types: thermionic emission and field emission, depending on the emission principle.

Thermionic Emission

In thermionic emission, a metal is heated to provide electrons with enough energy to overcome the work function barrier and escape from the metal surface. The emission follows Richardson's law[6]:

$$J = AT^2 e^{-\frac{\phi}{kT}} \quad (2.3)$$

Where J is the current density, T is the operating temperature in Kelvin, ϕ is the work function of the material, k is Boltzmann's constant (8.6 × 10^-5 eV/K), and A is Richardson's constant (A/m^2K^2).

Lanthanum hexaboride (LaB_6) is often chosen for thermionic emission due to its low work function (~2.5 eV) and relatively high operating temperature, which results in higher electron current densities and longer source lifetimes. Thermionic emitters exhibit broader electron-energy distributions (less monochromatic) compared to field emission sources [8].

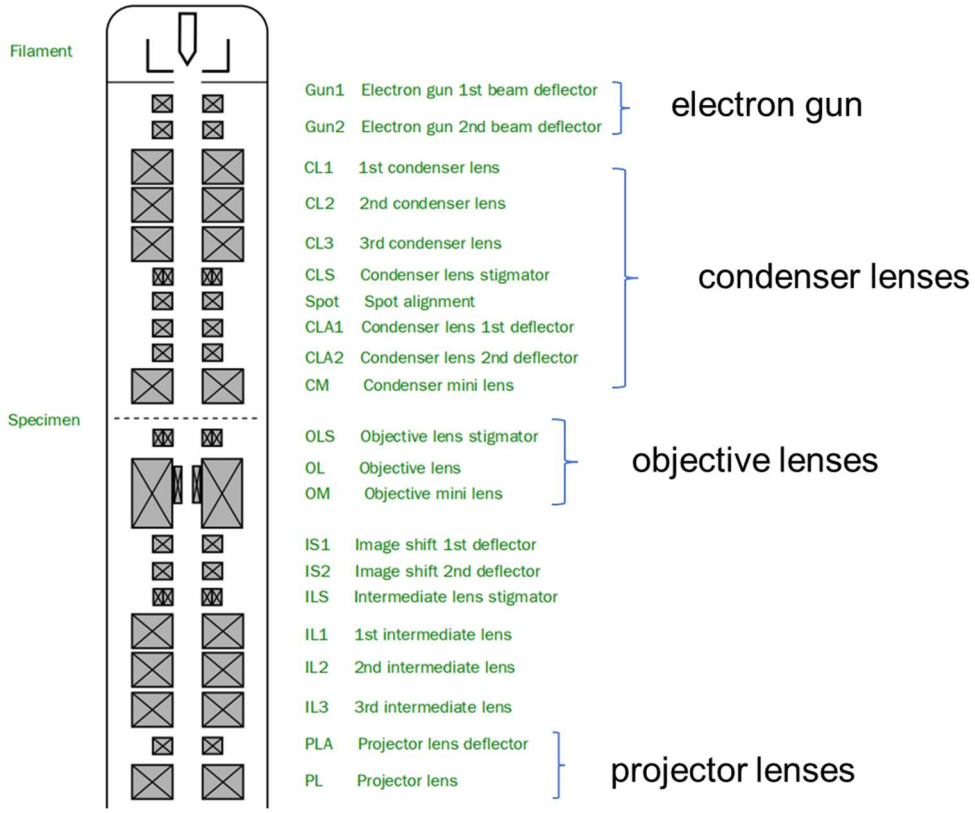

Figure 2. Main components of TEM[5].

Field Emission

Field emission leverages a high electric potential applied to an extremely sharp tip, which amplifies the local electric field. The field strength is

estimated by:

$$E = \frac{V}{r} \quad (2.4)$$

Where V is the applied voltage and r is the radius of the tip. If r is less than 0.1 μm, the field can reach 10^6 V/m, thereby reducing the energy barrier and allowing electrons to tunnel through it. [9][10].

In summary, thermionic emission guns are more robust and provide higher current, making them suitable for general-purpose electron microscopy. In contrast, field emission guns offer significantly higher resolution due to their monochromatic and coherent electron beams; however, they require more stringent maintenance and operating conditions [5].

Condenser Lenses

Condenser lenses in TEM control the electron beam emitted from the electron gun, ensuring even brightness and an adjustable illumination area. The condenser system typically consists of two primary lenses: Condenser Lens 1 (CL1) and Condenser Lens 2 (CL2). In advanced TEM systems, a third lens (CL3) is also included for enhanced control. At the same time, all condenser lenses share a similar construction; differences in the shape of their magnetic pole pieces and operating currents lead to variations in the strength and configuration of the generated magnetic field[11].

CL1 and Fixed Aperture: CL1 is a powerful lens that directs electrons through a fixed aperture into CL2. Operators adjust the beam size and intensity ("spot size") using the control panel [5].

CL2 and Condenser Aperture: CL2, which is weaker than CL1, governs the beam spot size and brightness on the specimen. A condenser aperture manages the total electron flux reaching the sample, which is controllable by the "brightness" knob. [12].

CL3 and Advanced Beam Control: Some TEMs include CL3 for finer adjustments of convergence angle and spot size, critical in high-resolution TEM (HRTEM) and scanning TEM (STEM) modes, where precise beam shaping is necessary [13].

CL3 and Convergence Angle: CL3 sets the convergence angle, concentrating the electron beam into a narrow, coherent spot. This condition is essential for achieving high spatial resolution in HRTEM and preserving beam quality in STEM [14].

CL3 and Beam Spot Size: CL3 is ideal for fine-tuning the beam size for any specific mode of imaging or analysis, enabling the operator to switch between various modes of operation without sacrificing beam quality.

Objective Lenses

Objective Lenses

The objective lens is the most critical component in the TEM, as it forms both the initial image and the diffraction patterns that subsequent lenses magnify. It typically consists of upper and lower pole pieces, as well as an objective aperture. Because the sample is situated within a strong magnetic field, advanced holders (e.g., tilt/rotation, heating/cooling) can be used to accommodate [10].

Intermediate Lenses

Intermediate lenses, situated between the objective and projector lenses, further enhance the image. They also adjust focus between imaging mode (real-space image) and diffraction mode (reciprocal-space pattern), allowing for flexible operation [5].

Projector Lenses

Finally, the projector lens system enlarges the image formed by the objective lens and displays it on a fluorescent screen or a digital camera [15].

2.1.3 Experimental Method and Basic Principles

When an electron beam passes through the sample, it undergoes analysis using advanced transmission electron microscopy (TEM)-based scattering and diffraction techniques.

Scattering and Diffraction

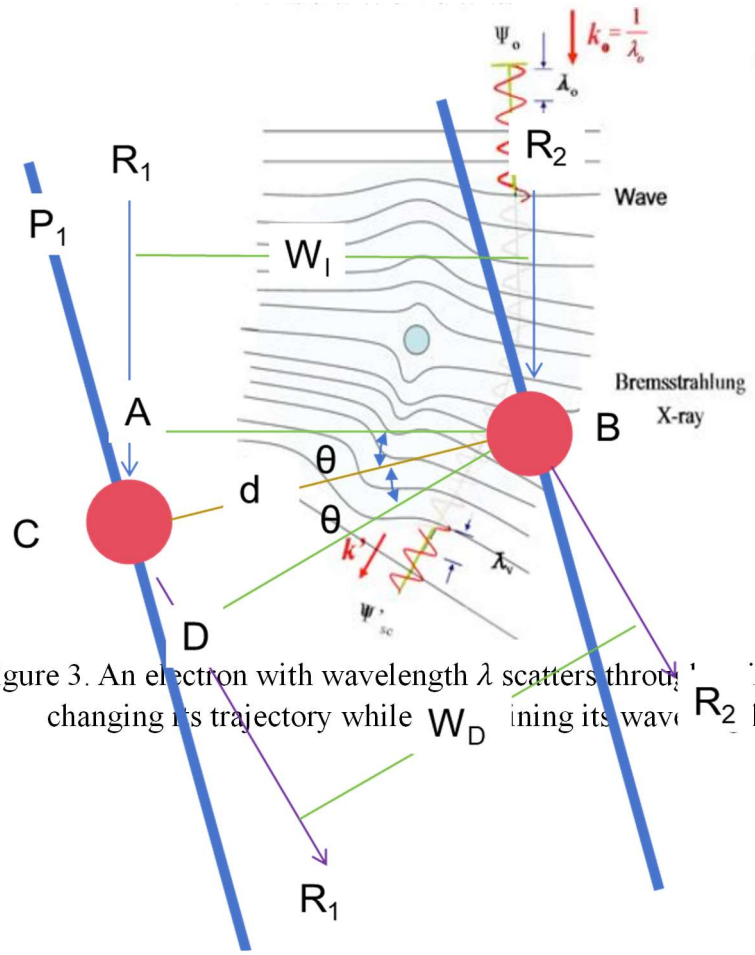

Figure 3. An electron with wavelength λ scatters throu ngle atom, changing its trajectory while ining its wav h [5].

Figure4. Beams R_1 and R_2 are scattered from two points, Cand B, which lie on different planes, P_1 and P_2. The rays travel different distances, resulting in a path difference of

In TEM, single-atom scattering provides quantitative images by elastically scattering electrons as they traverse a sample. In TEM, the incident electron beam can be approximated as a plane wave due to its coherence and wavelength characteristics. When an electron is brought near an isolated atom, the atom's Coulomb potential deflects the electron from k0 to k' (Figure 3). Despite this change in trajectory, the electron wavelength remains

unchanged in elastic scattering[16]. Occasionally, inelastic scattering co-occurs, causing energy loss and generating Bremsstrahlung X-ray emission [17].

Scattering by a Plane of Atoms

Similar to single-atom scattering, an electron beam interacting with a plane of atoms produces a diffracted wavefront (Figure 4). From geometry, the path difference is:

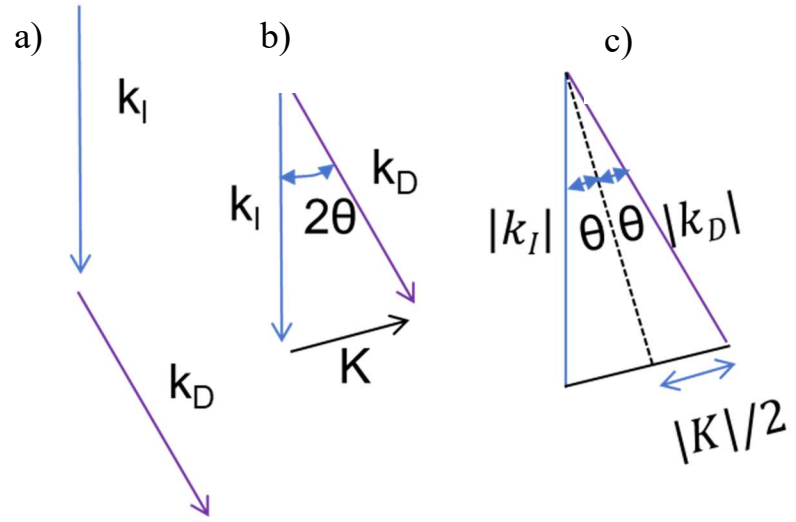

Figure 5. a) the incident wavefront normal is k_I, the diffracted wave normal is k_D; (b) K is the difference vector; (c) $\sin\theta$ is defined as $K/2K_I$ [5].

$$AC+CD=2d\sin\theta \qquad (2.5)$$

This path difference reflects the distinction between the incident wave normal k_I and the diffracted wave regular k_D (Figure 5). Since k_I and k_D each equal the reciprocal of the electron wavelength, their relationship can be

expressed as:

$$k = \frac{1}{\lambda} \tag{2.6}$$

Combining these relationships (Figures 4 and 5) with Bragg's Law yields the diffraction condition:

$$n\lambda = 2dsin\theta \tag{2.7}$$

Bragg's Law states that reducing the interplanar spacing (d) increases the diffraction angle (θ). Hence, measuring θ for a known electron wavelength λ allows the determination of d [18]. Because λ remains fixed under elastic scattering, constructive interference under Bragg's condition produces sharp diffraction spots [19].

Scattering by a Crystal

At the Bragg angle, the magnitude of K becomes K_B, satisfying:

$$K_B = \frac{1}{d} \tag{2.8}$$

This value represents the reciprocal-lattice vector for planes of spacing d.

Here, g denotes the diffraction vector. When an electron beam encounters atomic planes of spacing d under Bragg conditions, the resulting diffraction spots correspond to reciprocal-lattice points, indicating the directions of constructive interference. The vector g extends from the origin O to the first

diffraction spot G and remains perpendicular to the diffracting plane (Figure 6).

2.1.4 Diffraction Contrast

Selected Area Diffraction Patterns (SADPs)

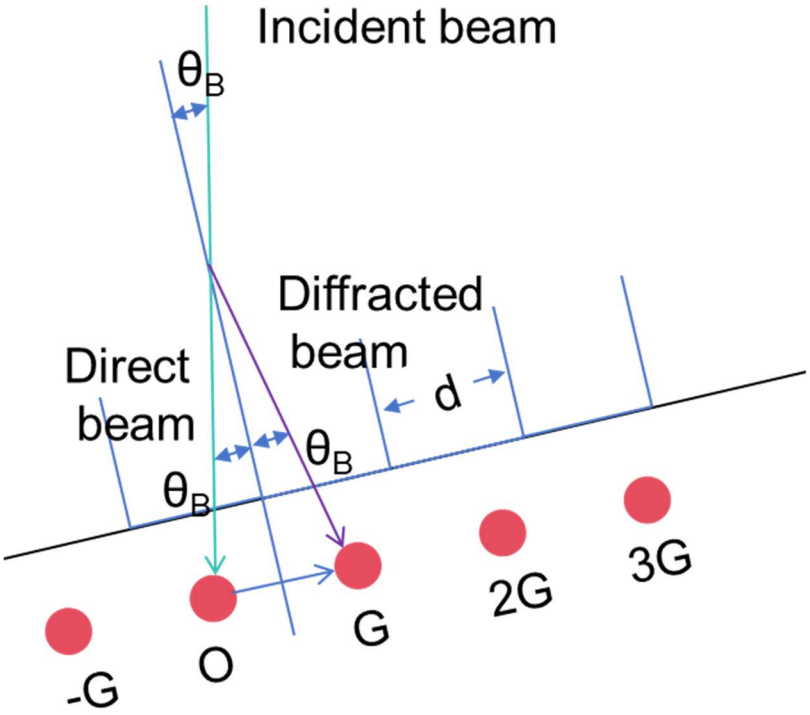

Figure 6. Diffraction spots formed when an incident beam passes through the crystal [5].

When multiple planes satisfy the Bragg condition, they produce an array of diffraction spots known as a diffraction pattern, which effectively probes crystal structures. To reduce complexity in these patterns, selected-area diffraction (SAD) confines the region contributing to diffraction, allowing for a more straightforward analysis [5].

By inserting a selected-area aperture in the first image plane below the objective lens (Figure 7), TEM operates in SAD mode, localizing the diffraction pattern to a chosen specimen region. During SAD, the condenser lens is often weakened to generate nearly parallel illumination [20].

When significant defects exist, local diffraction conditions shift. Hence, SADPs enable targeted orientations and regions for imaging, allowing precise analysis of crystal structures or defects. Typically, the central diffraction spot originates from unscattered electrons, while the additional spots arise from diffracted electrons [21].

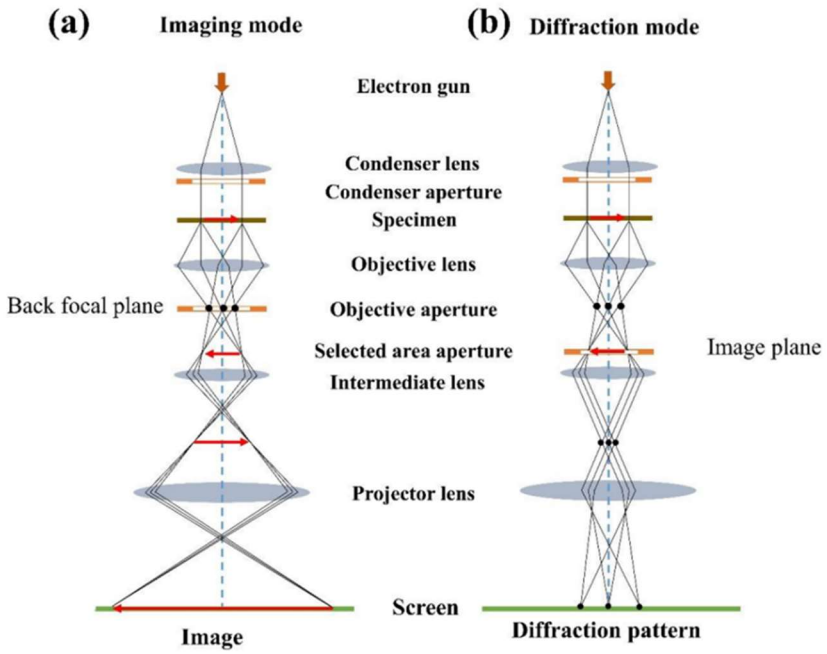

Figure 7.a) the image mode for TEM. b) the diffraction pattern mode for TEM, which is formed at or close to the back focal plane of the objective lens.

Dynamical Scattering

In TEM, an objective diaphragm positioned near the back focal plane can block most of the diffraction pattern, leaving a central spot from unscattered electrons and additional spots from diffracted beams.

Sample thickness has a significant influence on TEM images [22]. When specimens are thicker than a few tens of nanometers, electrons can traverse multiple sets of lattice planes, each fulfilling the Bragg condition. As electrons progress through the crystal, they continuously become scattered and remain unscattered, while others become diffracted (Figure 8a). Both the direct and scattered electrons will be further scattered as they pass deeper through the material. As the direct beam continues to scatter, the intensity decreases gradually while the number of scattered electrons increases. Sometimes, scattered electrons are in phase with direct electrons, resulting in constructive interference, whereby the intensity of the direct beam is slightly enhanced after passing through the material (Figure 8b) [23,24].

Consequently, a more complex diffraction pattern arises, rendering equally intricate TEM images. In thicker samples, additional planes meet Bragg conditions, reducing direct-beam intensity and producing darker regions (Figure 8).

Figure 8. a) when direction beam passing through a crystal under an influence of the dynamical scattering; b) the relationship between the incident beam and diffracted beam after passing through several position which follow the Bragg law.

Bright-Field (BF) and Dark-Field (DF) Imaging in TEM

In TEM, placing an objective diaphragm above the back focal plane inserts an aperture that blocks most diffracted beams (Figure 9a). If only the central, direct beam passes, the resulting image is a bright-field (BF) image [25]. Regions that diffract electrons appear darker since those electrons are blocked, and only transmitted electrons form the image. Conversely, if the central beam is blocked while a diffracted beam is selected, a dark-field (DF) image emerges (Figure 9b).

BF and DF imaging become especially useful in entirely defective crystals, such as gold leaf. Around a dislocation, local strain can temporarily affect some parts of the plane to satisfy Bragg conditions, scattering electrons and reducing the direct-beam intensity. In BF mode, defect regions appear darker because scattering weakens the direct beam; in DF mode, selecting scattered electrons brightens the same defects [26][27]. Such a contrast reveals detailed defect structures, which are crucial for materials like gold leaf [28].

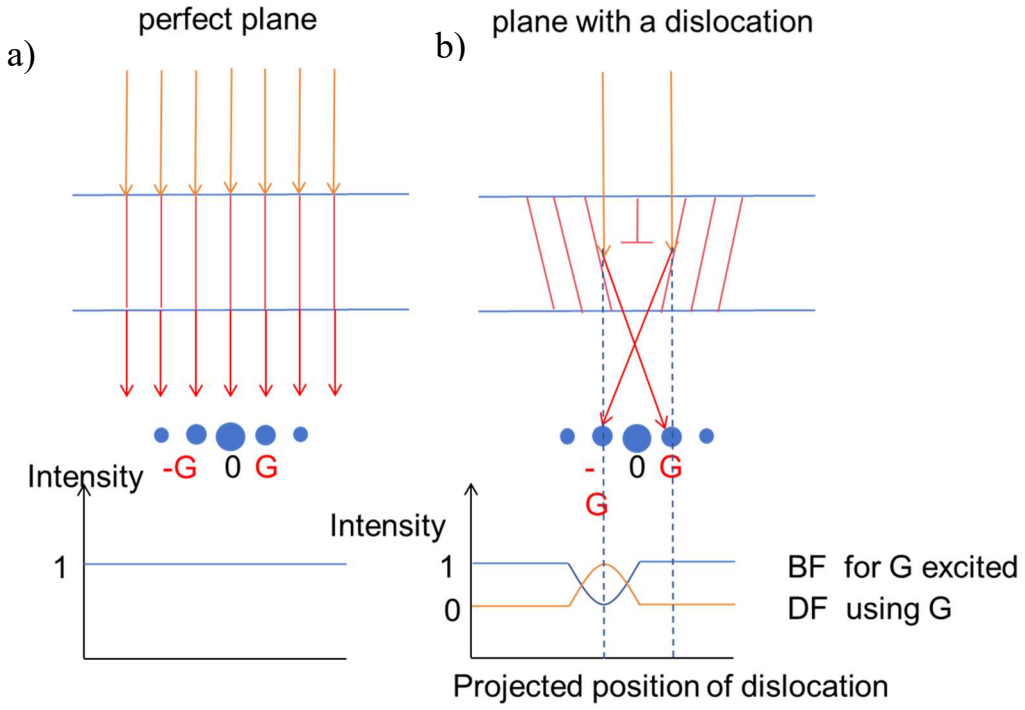

Figure 10. a) the beam passing by a crystal with perfect plane. (b): Intensity changes in BF and DF images due to the distorted planes.

Two-Beam Condition

In practice, dislocations complicate images because dynamic scattering often intensifies with sample thickness. When the beam aligns with a significant

zone axis (e.g., 100, 110, 111), multiple lattice planes diffract simultaneously. If, however, the electron beam is tilted slightly away from the zone axis, only one of the diffracted beams becomes prominent, and this has been referred to as the "two-beam condition."[29] In a two-beam condition, the scattering mechanism involves electrons scattering back and forth between the direct and only one diffracted state. As shown in Figure 11b, with increasing specimen thickness, the intensity of both the direct and diffracted beams

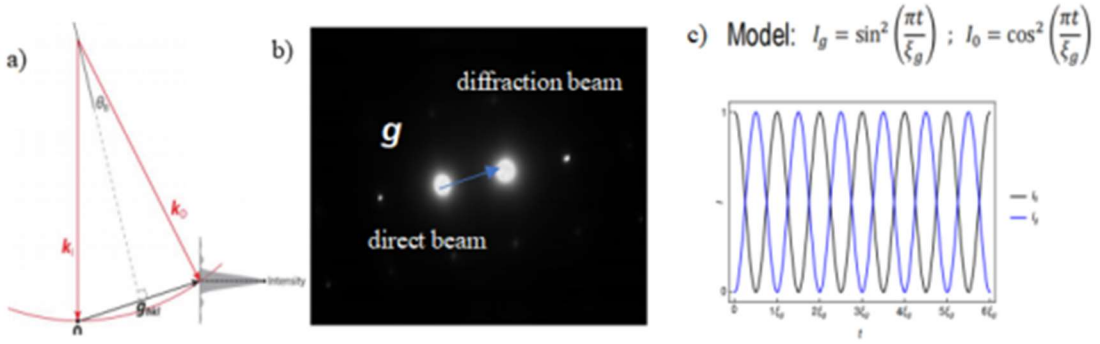

Figure 11. a) Two-beam condition with K_I and K_D following Bragg's Law； b) Diffraction pattern under the two-beam condition with a diffraction vector g； c): Dynamic correlation between direct and diffracted beam intensities.

oscillates[30]. Selecting a single diffraction spot enables dynamic scattering, facilitating a more straightforward interpretation. Therefore, images become easier to interpret. The diffraction vector, g, corresponds to the planes that satisfy Bragg's Law, so only those planes contribute to scattering [31].

This two-beam approach proves essential for investigating crystalline materials, especially in our study of gold leaf. It can highlight the defect, especially in contrast. It also helps us identify and locate dislocations.

Identification of Dislocations

Dislocations arise either from partial insertion/removal of lattice planes (edge dislocation) or by sliding (screw dislocation). An edge dislocation features an extra half-plane of atoms and a dislocation core perpendicular to the Burgers vector b. A screw dislocation involves twisted planes with a core parallel to b. In FCC crystals, all dislocations share a constant magnitude for b [32].

Because a dislocation's strain field aligns with b, the two-beam condition emphasizes distortions near the dislocation core. These distortions deviate locally from Bragg's condition, altering the electron intensities of both the direct and diffracted beams. As a result, dislocation structures become visible in the final image.

The visibility of a dislocation depends on $g \cdot b$. In detail (figure 12):

- If g is perpendicular to b ($g \cdot b = 0$) [33], then the dislocation will not be visible in the diffraction pattern because the strain field does not significantly alter the intensity of the diffracted beam.

- Conversely, if g is not perpendicular to b ($g \cdot b \neq 0$), the dislocation will be visible, as the strain field near the dislocation causes a measurable change in the intensity of the diffracted beam[34]

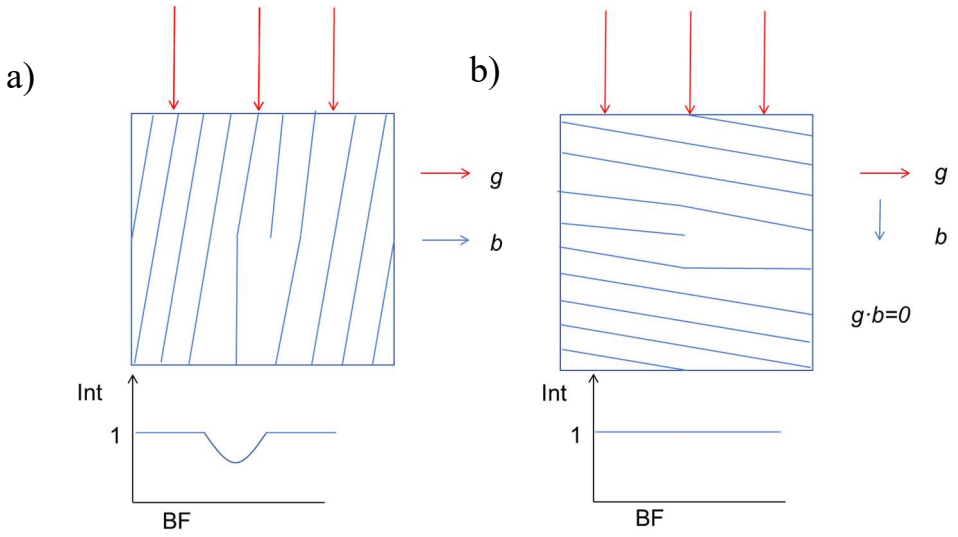

Figure12. a) when the dislocation's Burgers' vector is not perpendicular with the diffraction vector b) when the Burgers' vector is perpendicular with the diffraction vector.

During the experiment, by systematically varying g, one can determine the direction of b. A dislocation that disappears under certain g orientations but reappears under others reveals its Burgers-vector alignment [35].In the case, if $g_1 \cdot b=0$, $g_2 \cdot b=0$, but $g_3 \cdot b \neq 0$. We can get b = $g_1 \times g_2$.

Position of Dislocations and Dynamical Scattering

In practice, dislocation density and orientation can vary across a sample [37]. Some of them lie in planes that are usually incident to the electron beam, while others do not. Some dislocations lie in planes perpendicular to the electron beam, yielding uniform contrast, while others reside in angled

planes, producing alternating bright and dark fringes due to dynamical scattering [38]. Consequently, dislocations lying within planes perpendicular to the incident electron beam do not exhibit this contrast variation; instead, they appear as uniform, straight lines[39].

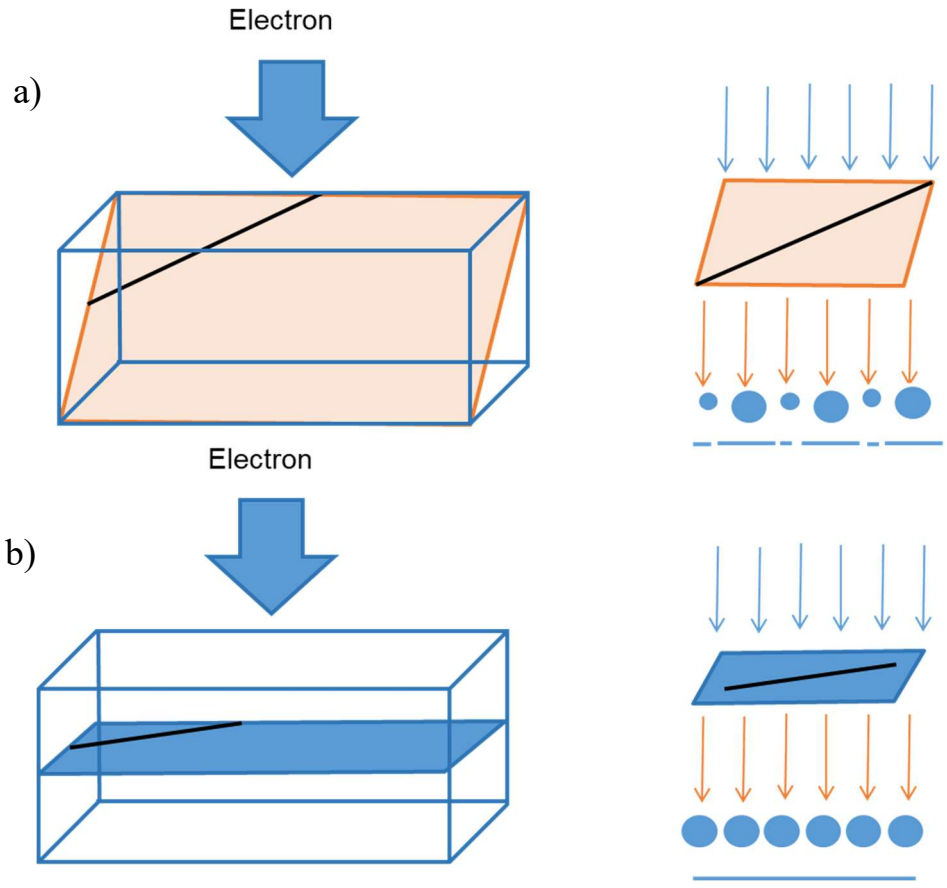

Figure 13.a) when a dislocation lies on planes non-perpendicular to the incident electron beam; b) lies on planes perpendicular to the incident electron beam

2.1.5 EDS Detector

Energy-dispersive X-ray spectroscopy (also referred to as EDX or XEDS) is

widely used for the identification and characterization of elements. A high-energy electron can eject an inner-shell electron of a target atom, creating a vacancy. An outer-shell electron then transitions to fill this vacancy, emitting a characteristic X-ray photon whose energy equals the difference between the two shells (Figure 14) [5]. Because each element's electron configuration is unique, the resulting X-ray energies serve as elemental "fingerprints". A silicon drift detector (SDD) collects these characteristic X-rays, generating an energy spectrum with peaks corresponding to specific elements. This analysis is often used in conjunction with SEM or TEM imaging to correlate microstructural features with chemical composition. Although EDS greatly facilitates concurrent microstructural and compositional analysis, its spatial resolution depends on the electron-beam interaction volume, which can potentially limit precision in elemental mapping due to the depth of X-ray generation.

As the gold leaf is an alloy, for our study, we use EDS in conjunction with STEM, allowing us to identify the alloy elements using TEM figures.

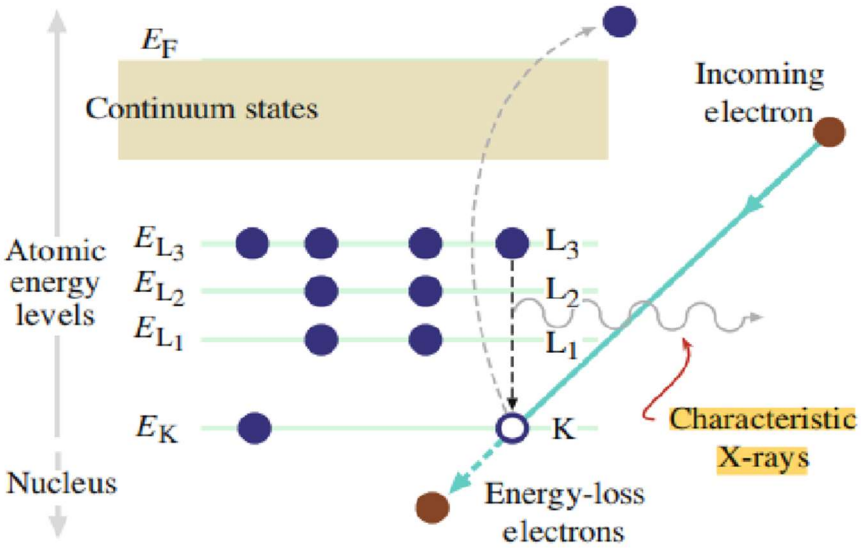

Figure14. Formation of Characteristic X-ray.

2.2 Electron Backscatter Diffraction (EBSD)

2.2.1 The theory of EBSD

Kossel Cones and Kikuchi Lines

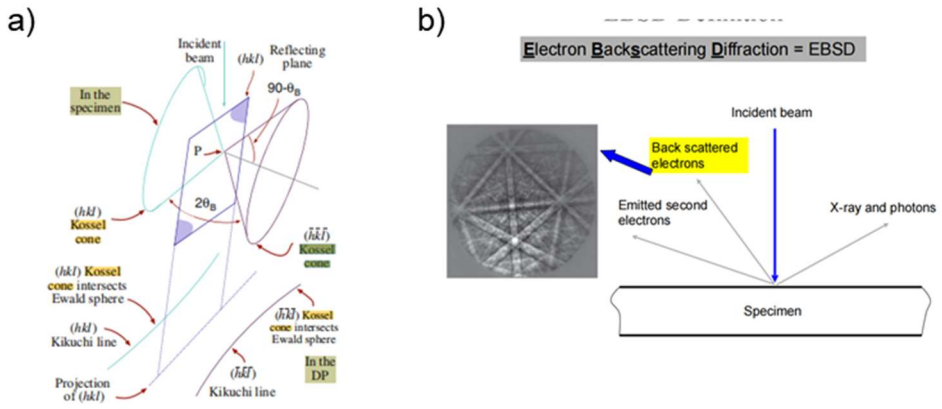

Figure 15. a) the formation of the Kossel cones and Kikuchi line. b) the EBSD base on SEM.

In a crystal, elastically scattered electrons radiate in multiple directions, sometimes meeting the Bragg condition for specific lattice planes. The collection of such scattered electrons forms a cone with an apex angle θ_B, called Kossel cones (Figure 15a). A corresponding cone at $-\theta_B$. Appears in the opposite direction. Each cone projects onto two lines, termed Kikuchi lines, with a fixed width of $2\theta_B$. Because they arise from Bragg diffraction, the positions of these Kikuchi lines follow the characteristics of the Bragg condition, which shift with changing diffraction angles and crystal planes [5]

Each crystal orientation generates a unique Kikuchi pattern, reflecting constant Bragg angles. For instance, in a [001] gold crystal, planes such as (100) and (110) form characteristic Kikuchi bands (Figure 16). These patterns effectively fingerprint crystal orientation because Bragg angles remain invariant for every crystal plane.

EBSD Patterns and Kikuchi Line Movement

In EBSD, Kikuchi lines map onto a stereographic projection, conveying crystallographic orientation data on a per-pixel basis. Unlike diffraction spots, which typically move with the beam, Kikuchi lines shift according to the sample's orientation. They resemble longitudinal lines on a globe, linking different crystallographic directions and enabling precise orientation measurements [40].

Orientation analysis in Kikuchi patterns arises by indexing these lines and comparing them to reference patterns. This methodology yields high-precision crystallographic data, revealing how the boundary geometry correlates with the sample's orientation. Such correlations offer crucial insights into crystal structure and orientation mapping [41].

Angle and Elastic Scattering in EBSD

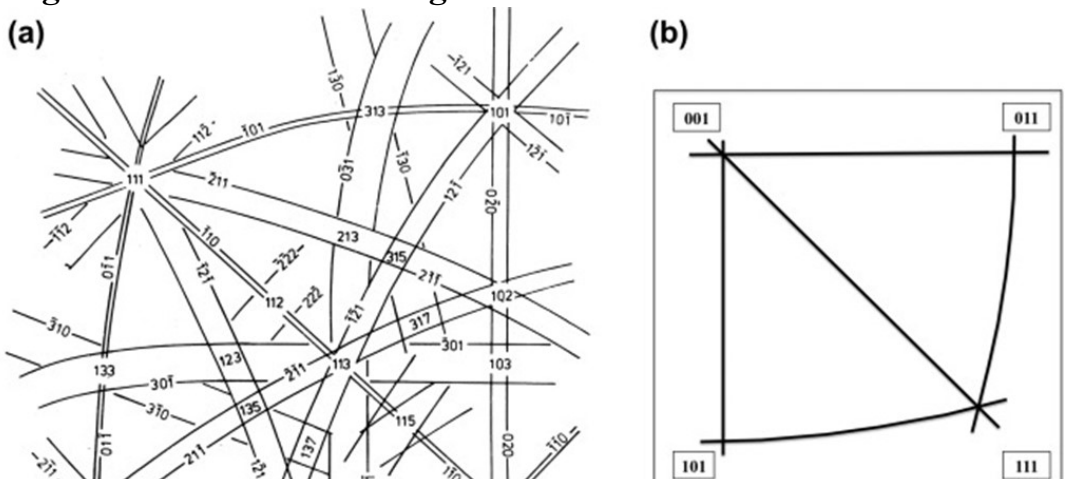

Figure 16. a) A Kikuchi map for FCC crystal (Taken from Loretto (1984)); b) The corresponding real-space stereogram. See text for explanation.

In SEM-based EBSD, the electron beam typically detects the sample at an angle of 60–70° (Figure 15b). At such tilt angles, backscattered electrons exhibit stronger elastic scattering under Bragg conditions, thereby enhancing Kikuchi-line visibility [42]. As sinθ is higher due to the more valuable tilting angle for the beam, resulting Kikuchi lines appear brighter and more distinct [43]. This approach broadens the range of crystallographic analysis, enabling a comprehensive structural assessment.

2.2.2 Methods of EBSD

Pole Figure (PF)

In polycrystalline materials, individual crystal often exhibits random orientations, yet some orientations can dominate, creating a texture. Two standard tools used to describe such distributions are the Pole Figure (PF) and the Inverse Pole Figure (IPF).

A Pole Figure (PF) (Figure 17) illustrates how a specific crystallographic plane (or direction) aligns with the sample's macroscopic coordinates. [44] For instance, in thin films, the Z-axis generally indicates the surface-normal direction, whereas X- and Y-axes define the plane of the film. The PF shows the orientation of a particular aircraft (or set of equivalent planes) in each grain, clarifying its alignment within the sample.

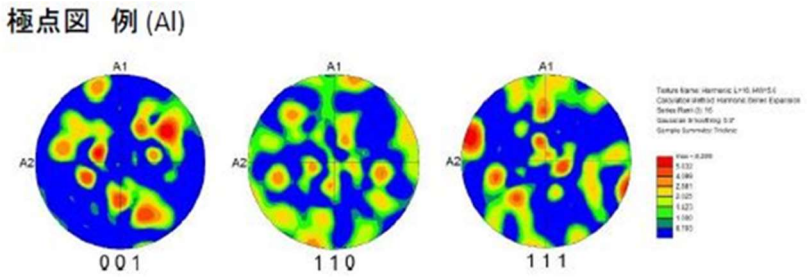

Figure 17. The pole figure shows a stereographic projection of how the {001} plane of the Al and the grain was tilted relative to the sample coordinates.

By contrast, an Inverse Pole Figure (IPF) maps how the sample's reference axis (e.g., the surface normal) aligns with the crystal's principal axes [45].

The Pole Figure is typically visualized using a stereographic projection. In this representation, each point on the PF corresponds to the orientation of the chosen crystallographic plane relative to the sample's coordinate system, providing a clear picture of how the grains are oriented within the sample and revealing any preferred crystallographic directions.

Inverse pole figure (IPF) and IPF coloring map

An IPF stereographic projection portrays grain orientations relative to the sample axes; each data point corresponds to a distinct crystal orientation. In EBSD, IPFs are often plotted along the [001] (Z) direction for thin samples, which denotes the sample's normal surface [46].

As an example, planes perpendicular to the z-axis, such as the (001) plane, are perpendicular to the [001] direction. EBSD, through this method, can

collect the Kikuchi patterns of every grain within the plane and determine the angular relationship it has with the [001] direction. To recognize every grain's orientation. A standardized color scheme typically codes {001}, {011}, and {111} as red, green, and blue, respectively (Figure 18). Grain boundaries between different orientations appear as lines on IPF maps.

Differences in crystal orientation along the x- and y-axes can then be visualized, represented by a small white cube indicating the alignment of the crystal axes with the sample's coordinate system.

By combining IPF data for the x -, y -, and z-axes, a 3D orientation profile is constructed for each grain [47]. For instance, grains displayed as predominantly red in a z-axis IPF (Figure 19) align their surface normal with the [001] direction. Combining the data along x- and y-axes, in our study, we collect such data to show as small orientation cubes.

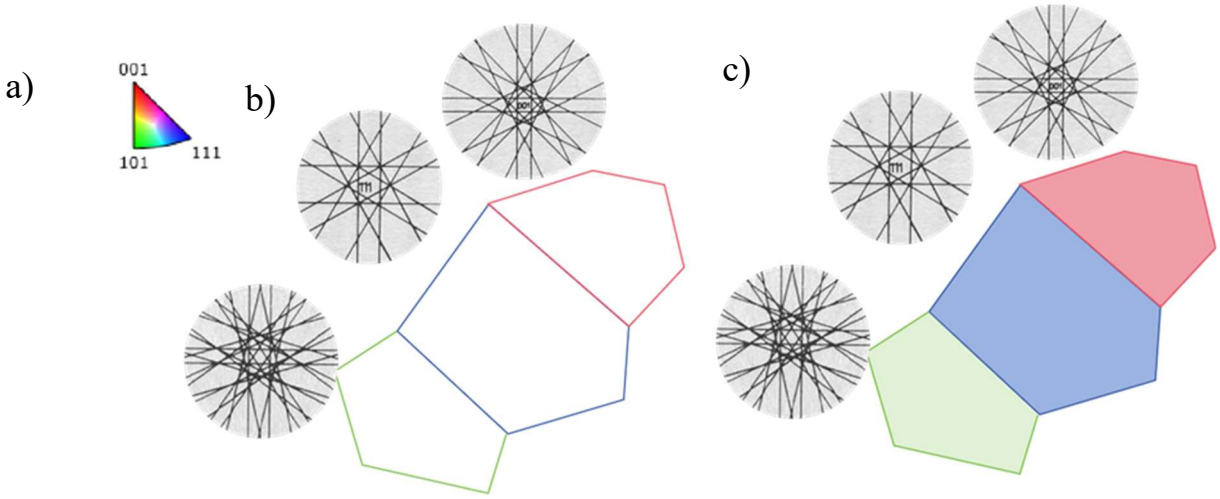

Figure 18.a) color scaling of IPF coloring; b) Kikuchi line which collect after EBSD scanning, which shows three types of different Kikuchi line of FCC from top is {001}, {111}, and {011}; c) After IPF coloring, different crystals have a different color

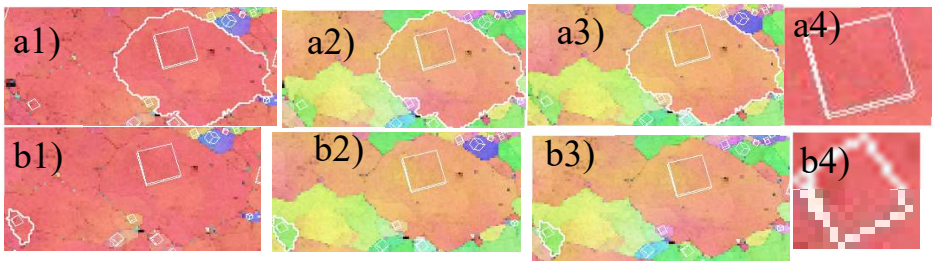

Figure19: IPF coloring for Al leaf data. a1, a1) for z-axis; a2 b2) for y-axis; a3, b3) for x-axis; a4, b4) after combining all three-axis data EBSD can help us make a figure for a crystal.

Grain boundaries

By the analysis method, we can also collect the Kikuchi patterns among neighboring grains and compare their angular misorientation values. Figure 20a illustrates high-angle grain boundaries (HAGBs) [48]. In this case, the Kikuchi line between the two grains is dramatically different, with distinct colors marking the grains. On the other hand, lower misorientations form

low-angle grain boundaries (LAGBs), which are indicated in green on IPF maps (Figure 20b). For such grains, in nearly aligned grains with minor angular deviation, IPF maps show similar colors, but there is a slight tilt between every grain. From empirical observations, such an angle is often less than 10° [49]. To distinguish the two types of grain boundaries, our study determined that the LAGBs were within an angle of less than 10°.

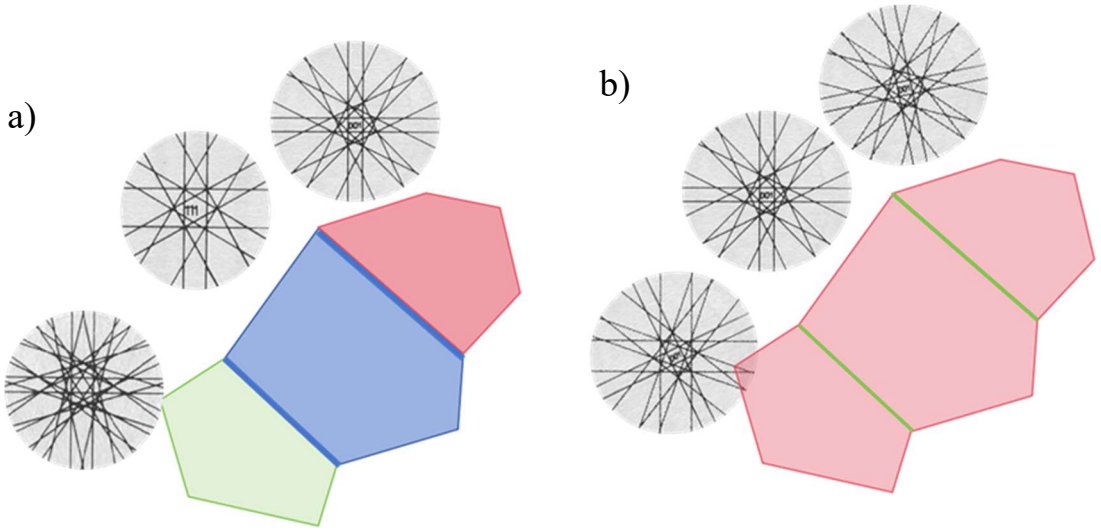

Figure20 a) blue line is high angle grain boundary, green line is low angle grain boundary) between different crystals, there is a grain boundary which can detect by EBSD scanning. b) Even though some area only a little bit twist, EBSD can also identify how much angel differences are they.

Kernel Average Misorientation (KAM)

Kernel Average Misorientation (KAM) quantifies the local misorientation between a reference pixel and its neighbors, typically within a range of 5° or less. High KAM values located within the grain indicate intense plastic deformation and elevated dislocation density, whereas low KAM values

within the grain mark minimally deformed or recrystallized grains [50]. Because KAM relies on parameters such as threshold angles and scan step sizes, its interpretation requires caution. In Kanazawa gold leaf specifically, KAM maps can help us highlight heavily deformed zones.

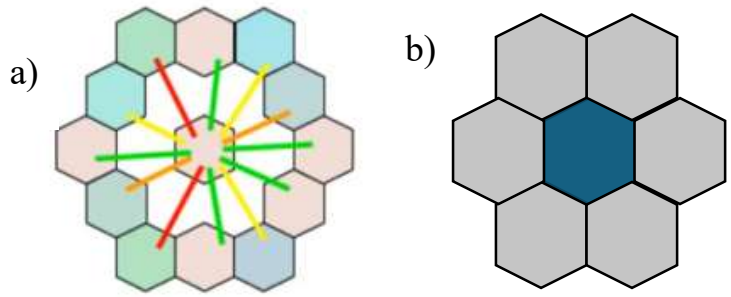

Figure 21 a) Calculate the angular deviation from the orientation at each point at the perimeter of the kernel with respect to the orientation at the center; b) Color center point according to the average deviation

Grain Orientation Spread (GOS) in EBSD Analysis

During EBSD acquisition, each pixel in a grain captures orientation data. Grain Orientation Spread (GOS) measures the deviation of each pixel's orientation from the average grain orientation. GOS is computed by summing the misorientations of all pixels relative to the central grain's mean orientation and then dividing by the total number of pixels. For instance, the orientation of pixel A, as shown in Figure 22A, is computed, and its orientation is compared to the orientations of its six nearest neighboring pixel points. The orientations of all pixel points in a grain, represented as device control 4 g indices a, l, l, and the average orientation of the grain, $\bar{g}$, are

analyzed. A measure is calculated by averaging these pixel orientations (Figure 22 B).

The deviation of each pixel point's orientation from the average, $\Delta g_i = \Delta(g_i, \bar{g})$, is calculated as the misorientation between the orientation of pixel point i and the average grain orientation.

The GOS value is then obtained by summing the orientation deviations of all points and dividing by the total number of points N:

$$\text{GOS} = \frac{1}{N}\sum_{i=1}^{N} \Delta g_i$$

Through the use of this method, each pixel in the grain color codes its orientation deviation from the average orientation of the grain, allowing for the visualization of the amount of variation in orientation. A low GOS value

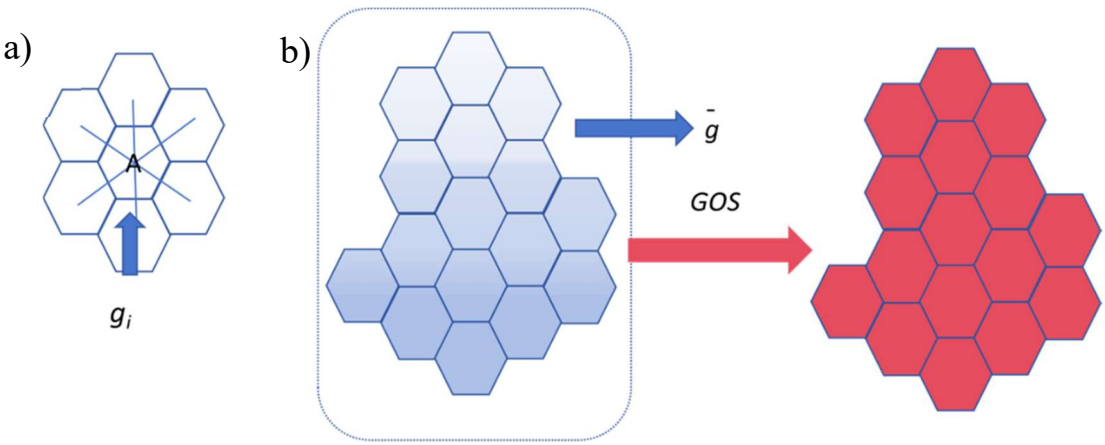

Figure 22. a) detect the orientation data for a single pixel. b) every $\bar{g}$ in the whole crystals for each pixel) GOS color for every points.

indicates that the grain is oriented in a reasonably consistent manner, often pointing to less deformation or post-recrystallization. A high GOS value indicates a significant variation in orientation within the grain, typically associated with plastic deformation and a higher density of dislocations.

The GOS value reflects the uniformity of grain orientation. Evaluation of GOS reveals regions of strain accumulation, providing insight into mechanical properties. For our study, this can help us understand how hammering influences the plastic deformation of the Kanazawa gold leaf.

A low GOS value implies uniform orientation, typically signifying mild deformation or post-recrystallization. High GOS marks indicate more extensive orientation spreads within the sample, consistent with plastic deformation and increased dislocation density [51]. GOS thus offers insight into how mechanical processes (e.g., hammering) alter microstructures, particularly relevant for Kanazawa gold leaf.

Equivalent Circle Diameter (ECD)

An Equivalent Circle Diameter (ECD) estimates grain size by matching a grain's projected 2D area to that of an equivalent circle (Figure 23). ECD is widely used to standardize grain-size measurements, enabling clear comparisons across samples or processing conditions [52].

As a measurement technique, this quantification method provides a precise and repeatable means of determining grain size, which enables direct comparison of various samples and test conditions. In our study, this approach allows us to quantify the grain size in each sample.

Aspect Ratio of the Fitted Ellipse

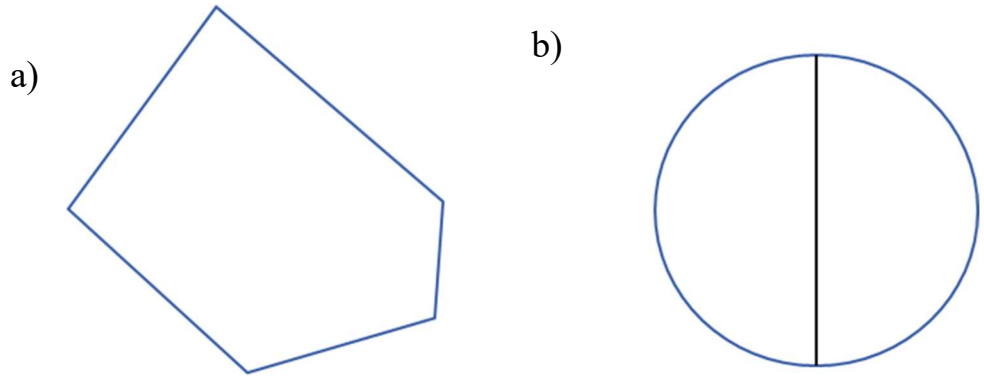

Figure 23. a) A crystal; b) A circle which have a same area as crystal A, and the black line is the ECD

The aspect ratio of a fitted ellipse quantifies the shape of grains. In this method, first find the central axis and minor axis by treating every grain as

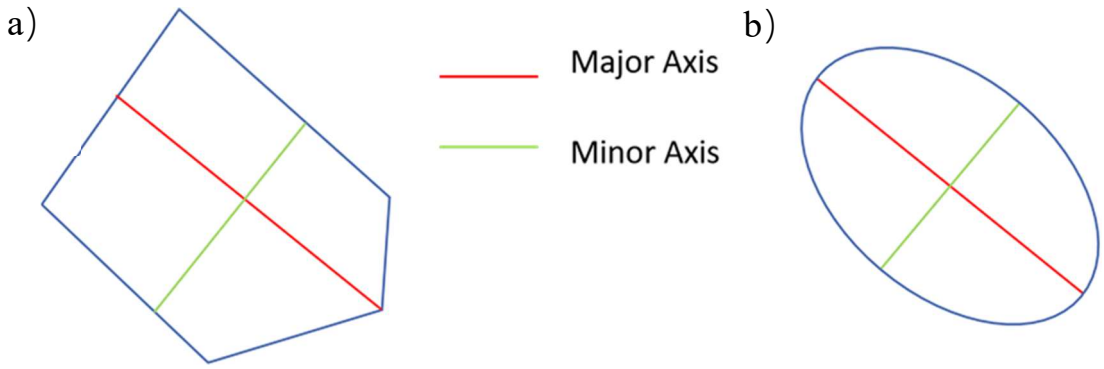

Figure 24 a) A crystal with a major axis (red), minor axis (green); b) based on the two axes, can for mate an oval. The Aspect ratio of the fitted ellipse is based on these two axes.

an oval, then compute the ratio of the significant axis length to the minor axis length (Figure 24). Values near 1 denote nearly circular grains, whereas those exceeding 1.5 indicate significant elongation [52].

Aspect ratio analysis is a crucial feature for describing the shape of grains, allowing us to understand material microstructural details. Elevated aspect ratios indicate elongated grains and potential anisotropy. This is typically observed in the cold deformation process, which occurs without the tempering process and influences mechanical behavior, such as strength and deformation. In our study, the severe hammering process may alter the grain size and morphology, providing us with a deeper understanding of the microstructural characteristics within gold leaf.

2.3 Sample and Experimental Method

2.3.1 Sample preparation

Sheet samples

We prepared two types of gold leaves: a 0.7 μm thick gold leaf referred to as the Zumi leaf and a typical 0.1 μm thick Kanazawa gold leaf, referred to as No. 4 leaf. Both of them contain the same alloy element compound, comprising gold, silver, and copper, as shown in No. 4. We also examined an Al leaf (~0.37 μm thick) to study the hammering process in diverse metals

(Figure 25). All samples were provided by Hakuichi Co., Ltd. Each sample was cut. To determine appropriate sizes for EBSD and TEM observations.

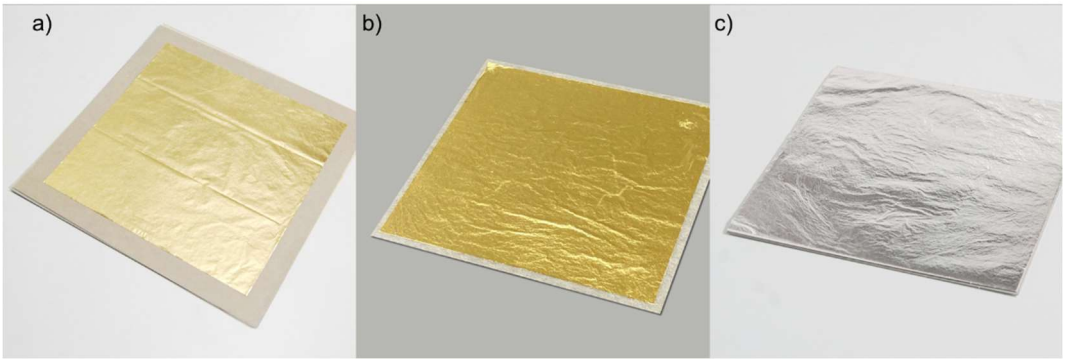

Figure 25. a) is the sheet of No.4 Kanazawa gold leaf with a thickness of 0.1μm; b) is the sheet of Zumi gold foil with a thickness of 0.7μm; c) is the sheet of Al leaf with a thickness of 0.37μm.

For EBSD, we affixed each sample to the stage with copper tape (Figure 26a).

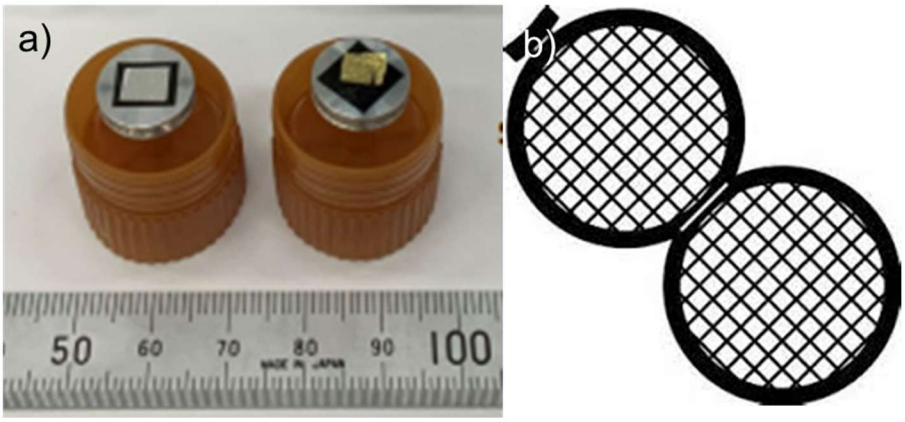

Figure 26. a) shows the Al leaf and gold leaf secured on the sample stage; b) is the double grid used for the sheet sample to make the TEM sample.

Figure 27. a) is the powder sample for pure gold leaf; b) is the powder sample for No.4 gold leaf.

For TEM, we used a double grid to secure sections of the sheet (Figure 26b).

Powder Sample

To gather higher-resolution data, we also prepared powder samples for TEM. One powder was derived from pure gold leaf (99.9% Au), and another was from No. 4 leaf (Figure 27). We subjected each powder to high-speed vibration, mixed it with alcohol, and deposited the suspension onto a single carbon (C) grid for TEM.

2.3.2 Experiment equipment

Ultra-high voltage TEM

To comprehensively observe the sheet structure of Kanazawa gold leaf, the metal textures of both No. 4 gold leaf and Al leaf (without thinning) were directly examined using a Hitachi H-3000 TEM at 2.0 MeV. This ultra-high-voltage TEM offers higher transmission power than conventional TEMs, enabling the acquisition of detailed internal structure information from thick specimens, such as gold leaf.

For an in-depth analysis of Kanazawa gold leaf structures, we employed a Hitachi H-3000 TEM at 2.0 MeV, which offers higher transmission power than standard TEMs due to its extra-high acceleration voltage. This capability enables detailed internal structural imaging of thicker samples

without the need for milling, allowing us to observe our sample without processing it and thereby preventing additional damage.

EDS and TEM

High-resolution TEM images of both No. 4 gold leaf and pure gold leaf in powder form were captured using a JEM-2100Plus TEM operating at 200 keV. We also conducted EDS for elemental composition analysis.

Figure 28. a) is Hitachi H-3000 TEM form Osaka university; b) is the JEM-2100Plus TEM with an eds detector; c) is the eds detector

SEM and EBSD

EBSD was performed using a ThermoFisher Scios2 dual-beam SEM with an Oxford Instruments EDS detector. Operating parameters included a grating resolution of 800 × 800 pixels, a step size of 0.25 μm, and an accelerating voltage of 15 kV. Acquired data were processed and analyzed using

AZtecCrystal software. These conditions were applied to Zumi gold foil, No. 4 leaf, and Al leaf samples (Figure 29).

Figure 29. a) is ThermoFisher Scios2 dual-beam SEM with an Oxford Instruments EDS detector; b) shows the samples during the texting.

2.3 Summary

This chapter outlines the experimental and analytical methodologies used to investigate the microstructures of the Kanazawa gold leaf. Transmission Electron Microscopy (TEM) and Electron Backscatter Diffraction (EBSD) serve as the core techniques in our study, enabling us to achieve high-resolution imaging, crystallographic orientation mapping, and elemental analysis.

TEM uses electron scattering to resolve atomic structures, characterize defects, and examine dislocations. EBSD is employed to study crystallographic texture and grain characteristics. Using Kikuchi patterns and the analysis method's help, to generate maps such as Inverse Pole Figures (IPFs) and Grain Orientation Spread (GOS) maps, and others. This

helps us to reveal the textural evolution and strain distribution within our samples.

Reference

[1] J. Canet-Ferrer and J. P. Martínez-Pastor, “Near-field scanning optical microscopy applied to the study of ferroelectric materials,” in *Ferroelectrics-Characterization and Modeling*, IntechOpen, 2011.

[2] S. J. Pennycook, “Transmission Electron Microscopy,” in *Encyclopedia of Condensed Matter Physics*, F. Bassani, G. L. Liedl, and P. Wyder, Eds., Oxford: Elsevier, 2005, pp. 240–247. doi: 10.1016/B0-12-369401-9/00582-9.

[3] M. P. Oxley, A. R. Lupini, and S. J. Pennycook, “Ultra-high resolution electron microscopy,” *Reports on Progress in physics*, vol. 80, no. 2, p. 026101, 2016.

[4] R. Gronsky, “Electron microscopy at atomic resolution,” *MRS Online Proceedings Library*, vol. 31, pp. 1–9, 1983.

[5] “Williams 和 Carter - 2008 - Transmission electron microscopy a textbook for m.pdf.”

[6] “The emission of electricity from hot bodies”.

[7] B. J. Kirby, *Micro- and Nanoscale Fluid Mechanics: Transport in Microfluidic Devices*, 1st ed. Cambridge University Press, 2012. doi: 10.1017/CBO9780511760723.

[8] D. C. Bell, C. J. Russo, and D. V. Kolmykov, “40keV atomic resolution TEM,” *Ultramicroscopy*, vol. 114, pp. 31–37, Mar. 2012, doi: 10.1016/j.ultramic.2011.12.001.

[9] D. J. Smith, “Progress and problems for atomic-resolution electron microscopy,” *Micron*, vol. 43, no. 4, pp. 504–508, 2012.

[10] P. D. Nellist *et al.*, “Direct sub-angstrom imaging of a crystal lattice,” *Science*, vol. 305, no. 5691, pp. 1741–1741, 2004.

[11] H. Kohl and L. Reimer, “Transmission electron microscopy,” *Springer Series in Optical Sciences*, vol. 36, 2008.

[12] P. D. Nellist *et al.*, “Direct sub-angstrom imaging of a crystal lattice,” *Science*, vol. 305, no. 5691, pp. 1741–1741, 2004.

[13] D. J. Smith, “Progress and problems for atomic-resolution electron microscopy,” *Micron*, vol. 43, no. 4, pp. 504–508, 2012.

[14] I. MacLaren and Q. M. Ramasse, “Aberration-corrected scanning transmission electron microscopy for atomic-resolution studies of functional oxides,” *International Materials Reviews*, vol. 59, no. 3, pp. 115–131, 2014.

[15] D. J. Smith, “Progress and perspectives for atomic-resolution electron microscopy,” *Ultramicroscopy*, vol. 108, no. 3, pp. 159–166, 2008.

[16] Z. Wang, *Elastic and inelastic scattering in electron diffraction and imaging*. Springer Science & Business Media, 2013.

[17] K. Mkhoyan, S. Maccagnano-Zacher, M. Thomas, and J. Silcox, “Critical role of inelastic interactions in quantitative electron microscopy,” *Physical review letters*, vol. 100, no. 2, p. 025503, 2008.

[18] M. Whelan, “Electron Diffraction Theory and Its Application to the Interpretation of Electron Microscope Images of Crystalline Materials,” *Advances in Electronics and Electron Physics*, vol. 39, pp. 1–72, 1976.

[19] K. Mkhoyan, S. Maccagnano-Zacher, M. Thomas, and J. Silcox, “Critical role of inelastic interactions in quantitative electron microscopy,” *Physical review letters*, vol. 100, no. 2, p. 025503, 2008.

[20] R. Pantel *et al.*, “Inelastic electron scattering observation using energy filtered transmission electron microscopy for silicon–germanium nanostructures imaging,” *Micron*, vol. 34, no. 3–5, pp. 239–247, 2003.

[21] K. Kimoto and Y. Matsui, “Experimental investigation of phase contrast formed by inelastically scattered electrons,” *Ultramicroscopy*, vol. 96, no. 3–4, pp. 335–342, 2003.

[22] A. Dutta and H. Heinrich, “Interfacial Atomic Number Contrast in Thick TEM Samples,” *arXiv preprint arXiv:1912.11440*, 2019.

[23] J. Cowley and P. Fields, “Dynamical theory for electron scattering from crystal defects and disorder,” *Acta Crystallographica Section A: Crystal Physics, Diffraction, Theoretical and General Crystallography*, vol. 35, no. 1, pp. 28–37, 1979.

[24] B. Kabius, V. Seybold, S. Hiller, A. Rilk, E. Zellmann, and W. Probst, “Energy-Filtering Techniques for Thick Samples,” *Microscopy and Microanalysis*, vol. 6, no. S2, pp. 166–167, 2000.

[25] P. Phillips, M. Mills, and M. De Graef, “Systematic row and zone axis STEM

defect image simulations," *Philosophical Magazine*, vol. 91, no. 16, pp. 2081–2101, 2011.

[26] J. E. Nathaniel II *et al.*, "Toward high-throughput defect density quantification: A comparison of techniques for irradiated samples," *Ultramicroscopy*, vol. 206, p. 112820, 2019.

[27] P. G. Callahan *et al.*, "Transmission scanning electron microscopy: Defect observations and image simulations," *Ultramicroscopy*, vol. 186, pp. 49–61, 2018.

[28] E. Butler, "An experimental evaluation of bright and dark field imaging modes in high voltage electron microscopy," *Micron (1969)*, vol. 5, no. 3, pp. 293–305, 1974.

[29] Z. Zhou, M. Jenkins, S. L. Dudarev, A. Sutton, and M. Kirk, "Simulations of weak-beam diffraction contrast images of dislocation loops by the many-beam Howie–Basinski equations," *Philosophical Magazine*, vol. 86, no. 29–31, pp. 4851–4881, 2006.

[30] L. C. Gontard, A. Barroso-Bogeat, R. E. Dunin-Borkowski, and J. J. Calvino, "A single slice approach for simulating two-beam electron diffraction of nanocrystals," *Ultramicroscopy*, vol. 195, pp. 171–188, 2018.

[31] V. A. Drits and V. A. Drits, "Dynamical n-Beam Scattering of Electrons," *Electron Diffraction and High-Resolution Electron Microscopy of Mineral Structures*, pp. 85–101, 1987.

[32] J. Jung, A. M. DaSilva, A. H. MacDonald, and S. Adam, "Origin of band gaps in graphene on hexagonal boron nitride," *Nature communications*, vol. 6, no. 1, p. 6308, 2015.

[33] Y. Yao *et al.*, "Study of dislocations in AlN single-crystal using bright-field synchrotron x-ray topography under a multiple-beam diffraction condition," *Applied Physics Letters*, vol. 117, no. 9, 2020.

[34] J. C. Ondry, M. R. Hauwiller, and A. P. Alivisatos, "Dynamics and removal pathway of edge dislocations in imperfectly attached PbTe nanocrystal pairs: toward design rules for oriented attachment," *ACS nano*, vol. 12, no. 4, pp. 3178–3189, 2018.

[35] N. Miyajima and N. Walte, "Burger's vector determination in deformed perovskite and post-perovskite of CaIrO3 using thickness fringes in weak-beam dark-field images," *Ultramicroscopy*, vol. 109, no. 6, pp. 683–692, 2009.

[36] W. Wu and R. Schäublin, “TEM diffraction contrast images simulation of dislocations,” *Journal of microscopy*, vol. 275, no. 1, pp. 11–23, 2019.

[37] W. Wu and R. Schäublin, “TEM diffraction contrast images simulation of dislocations,” *Journal of microscopy*, vol. 275, no. 1, pp. 11–23, 2019.

[38] W. Tunstall, P. Hirsch, and J. Steeds, “Effects of surface stress relaxation on the electron microscope images of dislocations normal to thin metal foils,” *Philosophical Magazine*, vol. 9, no. 97, pp. 99–119, 1964.

[39] B. Dulong, R. Haynes, and M. Robertson, “A study in the computation time required for the inclusion of strain field effects in Bloch-wave simulations of TEM diffraction contrast images,” *Ultramicroscopy*, vol. 108, no. 5, pp. 415–425, 2008.

[40] C. Ball, “Accurate determination of crystallographic orientation from Kikuchi patterns,” *Philosophical Magazine A*, vol. 44, no. 6, pp. 1307–1317, 1981.

[41] A. Winkelmann, G. Cios, T. Tokarski, G. Nolze, R. Hielscher, and T. Kozieł, “EBSD orientation analysis based on experimental Kikuchi reference patterns,” *Acta Materialia*, vol. 188, pp. 376–385, 2020.

[42] A. Schwartz, “Electron Backscatter Diffraction in Materials Science,” 2009.

[43] M. Vos and A. Winkelmann, “Two-dimensional Kikuchi patterns of Si as measured using an electrostatic analyser,” *Ultramicroscopy*, vol. 171, pp. 19–25, 2016.

[44] J. Starkey, “Analysis of orientation diagrams derived from a simulated quartz fabric,” *Canadian Journal of Earth Sciences*, vol. 24, no. 3, pp. 565–571, 1987.

[45] C. Chou, P. Rolland, and K. Dicks, “A new method for analyzing electron backscatter diffraction (EBSD) data for texture using inverse pole figures,” *Microscopy and Microanalysis*, vol. 8, no. S02, pp. 686–687, 2002.

[46] G. Nolze and R. Hielscher, “Orientations–perfectly colored,” *Journal of Applied Crystallography*, vol. 49, no. 5, pp. 1786–1802, 2016.

[47] P. Callahan, S. Singh, M. Echlin, J. Stinville, T. Pollock, and M. De Graef, “Automated Prediction of Pseudo-Symmetry Issues in EBSD,” *Microscopy and Microanalysis*, vol. 24, no. S1, pp. 566–567, 2018.

[48] L. Zhang, B. Radiguet, P. Todeschini, C. Domain, Y. Shen, and P. Pareige, “Investigation of solute segregation behavior using a correlative EBSD/TKD/APT

methodology in a 16MND5 weld," *Journal of Nuclear Materials*, vol. 523, pp. 434–443, 2019.

[49] Y. Chen, Y. Li, J. C. Walmsley, S. Dumoulin, P. C. Skaret, and H. J. Roven, "Microstructure evolution of commercial pure titanium during equal channel angular pressing," *Materials Science and Engineering: A*, vol. 527, no. 3, pp. 789–796, 2010.

[50] K. Kubushiro, Y. Sakakibara, and T. Ohtani, "Creep strain analysis of austenitic stainless steel by SEM/EBSD," *Journal of the Society of Materials Science, Japan*, vol. 64, no. 2, pp. 106–112, 2015.

[51] A. Ayad, N. Allain-Bonasso, N. Rouag, and F. Wagner, "Grain Orientation Spread values in IF steels after plastic deformation and recrystallization," presented at the Materials Science Forum, Trans Tech Publ, 2012, pp. 269–272.

[52] Y. Coutinho, S. Rooney, and E. Payton, "Analysis of EBSD grain size measurements using microstructure simulations and a customizable pattern matching library for grain perimeter estimation," *Metallurgical and Materials Transactions A*, vol. 48, pp. 2375–2395, 2017.

Chapter 3 Texture evaluation of Kanazawa gold leaf

3.1 Introduction

Kanazawa gold leaf is a traditional Japanese material renowned for its exceptional thinness (100–200 nm), brilliant luster, and intricate fabrication technique that has been refined over centuries. It is fabricated by a pack and hammer method at room temperature, which differs fundamentally from conventional techniques such as cold rolling, but the underlying mechanisms to achieve such thinness and luster remain unclear. Kitagawa and Tanimura [1] [2] used X-ray diffraction (XRD) to investigate the thinning process of Kanazawa gold leaf by the pack and hammer method and found that the {011} texture, which developed when the thickness was reduced to about 10 μm, was replaced by the near-cube {001} texture when the thickness was reduced below 0.3 μm. Kitagawa [3] proposed that a high percentage of the {001} texture may result from cross-slip events induced by severe hammering deformation. The {001} texture is generally considered unstable and does not typically serve as the final texture in cold-rolled materials. Various cold-rolled materials that exhibit an initial cube texture frequently transition to other textures [4] [5]. For example, Akef and Driver [6] demonstrated that aluminum processed at a temperature below 60% of the melting temperature

(T_m) transitioned from the cube {001} <100> and rotated-cube {001} <110> textures to the copper {112} <111> or brass {011} <211> textures owing to activation of an octahedral slip system. The degree of rotation of cube and near-cube textures varies with the applied stress and strain [7] [8] [9]. In contrast, cube textures are frequently observed during annealing of heavily deformed face-centered cubic (FCC) materials or during hot rolling [10] [11]. Under these conditions, the formation of a cube texture is generally associated with recrystallization [12]. Maurice and Driver [13] demonstrated that the high-temperature processing of FCC metals can activate non-octahedral slip systems such as the {110}–<110> slip system, which results in the formation of a stable cube texture. However, the development of a strong and stable {001} texture at room temperature has rarely been reported. Thus, understanding how ultrathin films such as Kanazawa gold leaf can be fabricated via the pack and hammer method at room temperature while maintaining a {001} texture is a topic of both scientific and industrial significance.

3.2 Materials and methods

We investigated the evolution of the {001} texture in Kanazawa gold leaf by electron backscatter diffraction (EBSD) [14] [15] and transmission electron microscopy (TEM) [16] [17]. Because the {001} texture is dominant when

the thickness is below 0.3 μm, two types of gold leaf were prepared: one with a thickness of about 1 μm and corresponding to the starting material for the second hammering stage (i.e., Zumi foil) and the other with a thickness of 0.1 μm, which is typical of Kanazawa gold leaf (No. 4 leaf). Both types of gold leaf were obtained from Hakuichi Co., Ltd. and were cut into small pieces for observation by EBSD and TEM [18]. EBSD was performed by using dual-beam scanning electron microscopy (Thermo Fisher Scios 2) with an energy-dispersive spectroscopy detector (Oxford Instruments). The operating parameters included a grating resolution of 800 × 800 pixels, step size of 0.25 μm, and accelerating voltage of 15 kV. The acquired data were processed and analyzed by using the software AZtecCrystal (Oxford Instruments). The Kikuchi patterns of the backscattered electrons were obtained by illuminating a convergent electron beam at each pixel, which were then used to obtain the three-dimensional crystal orientation and local strain [19] [20]. The orientation distribution function (ODF) was obtained for quantitative analysis of sample textures [21]. To assist in understanding the ODF data, Fig. 2 shows the relationships of typical textures with their orientation within a synthesized film as a reference. TEM (Hitachi H-3000) was operated at an ultrahigh voltage (UHV) of 2.0 MV to increase the transmittance of the samples and facilitate the observation of their structures

without sample thinning processes [22] [23]. Samples were tilted to adjust the excitation conditions for electron incidence, which obtained bright-field (BF)- and dark-field (DF)-TEM images that could be used to observe dislocations.

3.3 Results

3.3.1 Electron backscatter diffraction

Fig. 1 (a) and (b) shows the inverse pole figure (IPF) and the derived coloring map for the Zumi foil and No. 4 leaf [24]. The coloring map for the Zumi foil (Fig. 1(a)) predominantly comprised {101}-oriented grains (green area), although the orientation was not perfectly aligned even within individual grains as evidenced by their non-uniform colors. In addition, high-angle grain boundaries (HAGBs) (black lines) were not straight but wandering. The unit cell of the FCC lattice (white lines) shows different orientations depending on the location. These results suggest that many dislocations and defects exist in the Zumi foil. The IPF of the Zumi foil (Fig. 1(c)) show that the multiple random distribution (MRD), which increases in value with the ratio of the corresponding texture, was about 4.81 for {101}-oriented grains (red area) and 2.13 for {201}-oriented grains. The presence of {201}-oriented grains indicates that the texture was not strongly oriented to {101}

but was slightly tilted along the <001> direction.

For the No. 4 leaf (Fig. 1(b)), {001}-oriented grains were predominant (red area). The unit cell of the FCC structure (white lines) showed almost the same orientation throughout the observed area, which means that the crystal orientation was aligned not only perpendicular to the sample surface. Areas without {001}-oriented grains (yellow and purple streaks) had orientations tilted from the <001> direction to the <101> direction or the <111> direction. In addition, such regions surrounded by HAGBs were observed to have the {101} texture. These results suggest that the change in orientation from the {101} texture to {001} texture occurred in individual regions tens of micrometers in diameter during the second hammering stage, which may have formed HAGBs between adjacent regions. The IPF of the No. 4 leaf (Fig. 1(d)) shows that the MRD value of the {001}-oriented grains was 22.28, which suggests that the {001} texture is dominant.

The ODF describes the three-dimensional distribution of the crystal orientation in a sample and was obtained for the sections φ_2 = 0° and φ_2 = 45°, as shown in Fig. 2. For the section φ_2 = 0°, the textures of the Zumi foil (Fig. 2(a)) were roughly distributed around φ_1 ~ 0°, 45°, 90°, 135°, and 180°

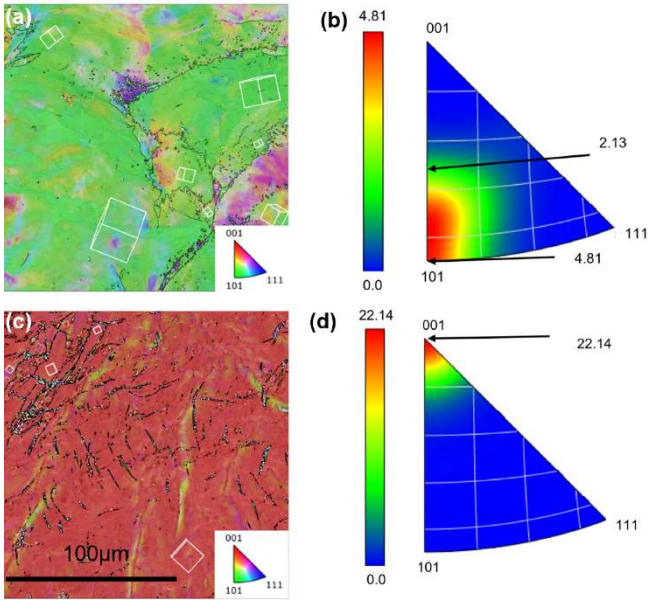

Figure 4. Inverse pole figure (IPF) coloring maps of the (a) Zumi foil and (c) No. 4 leaf. The color scale is derived from orientations aligned perpendicular to the sample surface (red, green, and purple correspond to the {001}, {110}, and {111} planes, respectively; black curves correspond to grain boundaries with misalignment angles greater than 15°; white lines depict the projected unit cell of the cubic structure). IPFs from the Z-axis of the (b) Zumi foil and (d) No. 4 leaf.

along the line of Φ = 45°. This indicates strong alignment with the {011} texture and a certain degree of in-plane crystalline orientation. However, the MRD values were not locally maximum at φ_1 ~ 0°, 45°, 90°, 135°, and 180°, which suggests that the crystal orientation must slightly deviate from the Goss texture (i.e., {011} texture with <100> orientation along the X-axis

corresponding to (0° (or 90°), 45°, 0°)) or rotated Goss texture (i.e., {011} texture with <110> orientation along the X-axis corresponding to (45° (or 135°), 45°, 0°)). These textures had MRD values of 7.2 and 4.6, respectively.

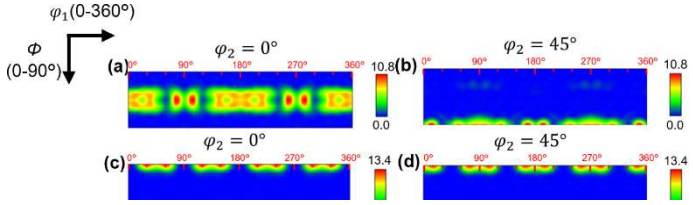

Figure 5. φ_2 = 0° and 45° sections of the orientation distribution function (ODF) showing the textures of the (a, b) Zumi foil and (c, d) No. 4 leaf.

In contrast, the {011} texture with the <133> orientation along the X-axis corresponding to (φ_1,Φ,φ_2) = (75°,45°,0°) had a MRD value of 10.8. This orientation deviates 15° from the ideal rotated Goss texture. In addition, the brass texture (i.e., {011} texture with the <112> orientation corresponding to (35°, 45°, 0°)) had a MRD value of 8.4. Conversely, the MRD value remained below 2 for φ_1 = 55°–65°, which indicates that the corresponding textures were rare. For the φ_2 = 45° section (Fig. 2(b)), the Zumi foil did not exhibit any notable textures. This suggests that the Zumi foil strongly prefers the {011} plane in the Z-direction but is more broadly distributed in the in-plane direction rather than being strongly associated with a single ideal texture.

The ODF results for the No. 4 leaf revealed a sharper distribution of textures than for the Zumi foil. For the φ_2 = 0° section (Fig. 2(c)), a pair of preferred

textures were observed with MRD values of 13.4 at (30°, 0°, 0°) or (60°, 0°, 0°), which correspond to the {001} texture with the <310> orientation. This orientation deviates from the rotated cube texture ({001} texture with the <110> orientation corresponding to (45°, 0°, 0°)) by 15°, which suggests that the preferred texture was formed. In addition, these dominant textures were observed at symmetric positions including lines along Φ = 90° in the φ_2 = 0° section and Φ = 0° in the φ_2 = 45° section (Fig. 2(d)). Compared to the Zumi foil, which exhibited multiple textures, the No. 4 leaf demonstrated a transition toward a single dominant texture.

Figs. 3(a) and (b) show the kernel average misorientation (KAM) maps of the Zumi foil and No. 4 leaf, respectively. The maximum misorientation angle was set to 15°. The KAM is similar to the second derivative of the crystal orientation distribution, so it gives data that are sensitive to dislocations. A KAM value that exceeds 1 indicates the presence of a dislocation. The KAM maps contain many green streaks with KAM values of 1–2, which may correspond to dislocation lines. For the Zumi foil, many short green streaks can be observed along the HAGBs (black lines), suggesting that dislocations moved to the grain boundaries and collected there. For the No. 4 leaf, the dislocations were observed throughout the sample, suggesting that many dislocations became entangled and became

immobile. In addition, about 61% of the area of the No. 4 leaf had KAM values exceeding 1, but this held true for only 23% of the area of the Zumi foil. Thus, the dislocation density increased during the second hammering

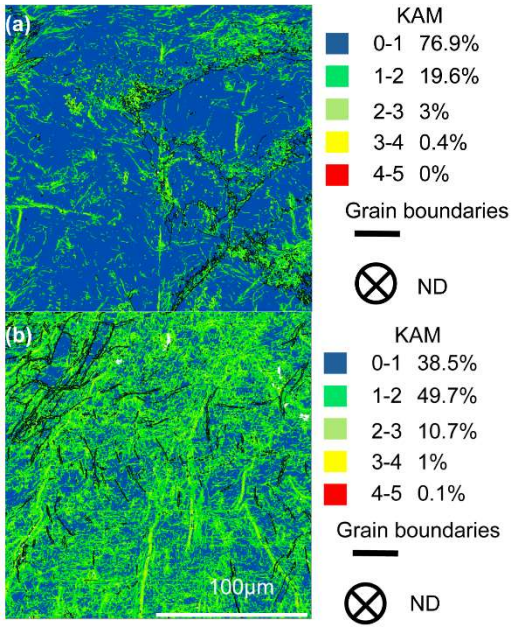

Figure 6. Kernel average misorientation (KAM) maps of the (a) Zumi foil and (b) No. 4 leaf. Colors indicate the average misorientation. Blue indicates a relatively small value, and green, yellow, and red indicate larger values in order. A larger value suggests the presence of a dislocation.

stage, which indicates that no recrystallization or recovery occurred.

3.3.2 Transmission electron microscopy

As shown in Fig. 4(a), the BF-TEM images of the Zumi foil were taken under the two-beam condition by exciting the $g = 020$ reflection at an accelerating voltage of 2 MeV. Some dark streaks (white arrows) were observed with a large number of dislocations between them. In the selected area electron

diffraction (SAED) pattern (Fig. 4(b)), which was taken at the area

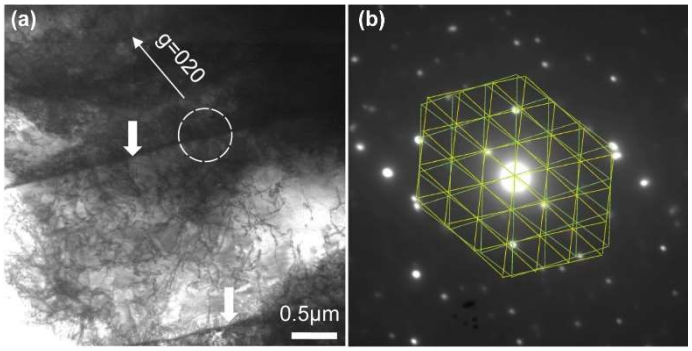

Figure 7. (a) Two-beam bright-field (BF)-TEM images of the Zumi foil under the condition g = 020. (b) Local diffraction pattern for the dashed white circle in (a).

containing the dark streak (dashed circle in Fig. 4(a)), two periodic patterns (yellow and green hexagonal lattices) are observed. These correspond to patterns obtained when the incident electron beam was irradiated almost along the <110> zone axis but were tilted by approximately 5° from each other. This indicates that the black streak in the SAED pattern may correspond to a low-angle grain boundary. It was difficult to obtain clear TEM images or diffraction patterns of the Zumi foil owing to the thickness of the sample, but HAGBs were rarely observed, which is consistent with the KAM results (Fig. 3).

Figs. 5(a) and (b) show BF- and DF-TEM images of the No. 4 leaf obtained under the two-beam condition with a strong excitation of $g = \bar{2}00$. The DF-TEM image shows not only bright regions corresponding to areas where the Bragg condition was satisfied but also bright streaks corresponding to areas

satisfying the Bragg condition near dislocation lines, where the electron diffraction conditions varied owing to the large structural deformation. The bright streaks formed along not only the $[\bar{1}01]$ direction but also the $[101]$ direction, which are orthogonal to each other. This is important evidence that slip occurred on the $\{110\}$ plane even in the FCC structure. It cannot be explained by slip on the $\{111\}$ plane because the (111), $(\bar{1}11)$, $(1\bar{1}1)$ and

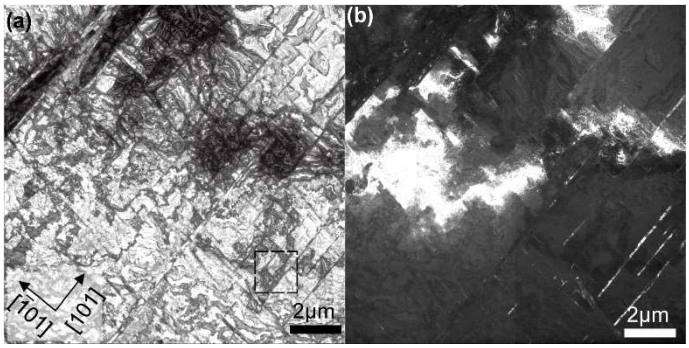

Figure 8. (a) BF- and (b) dark-field (DF)-TEM images of the No. 4 leaf. The DF-TEM image was taken by selecting the diffracted spot ($g = \bar{2}00$). The bright narrow belts correspond to slip bands. Several bright narrow bands can be observed along not only the [101] direction but also the $[\bar{1}01]$ direction. These bands are orthogonal with each other.

$(11\bar{1})$ planes, which are the slip planes of gold FCC crystals, do not form angles of 90° with each other.

Fig. 6 shows an enlarged BF-TEM image of a selected area (dashed square in Fig. 5(a)). Slip bands with many short stripes were observed along the [101] direction. However, some bands were observed along the $[\bar{1}01]$ direction, which is perpendicular to the [101] direction. Because the short

stripes in the slip bands are not aligned as regularly as those typically seen in stacking faults, they must correspond to screw dislocations. However, the observed slip planes cannot be explained by {111} planes because they do not intersect at right angles in the case of FCC crystals. Therefore, these results may indicate the activation of non-octahedral slip systems such as the {110}–<110> slip system, as reported by Maurice and Driver [13]. In this case, the slip bands corresponded to the {110} slip planes. However, as shown in Fig. 6(a), the short stripes corresponding to the dislocation lines were not necessarily perpendicular to the slip bands because these dislocation lines can be formed by a mix of screw and edge dislocations. In addition, the widths of the slip bands were roughly the same (~100 nm). This may have been caused by the slip plane terminating at both surfaces of the No. 4 leaf, as shown by the schematic of the $(\bar{1}01)$ slip plane in Fig. 6(b). Screw dislocations that terminate at both surfaces may be more mobile and may line up at nearly equal intervals on the slip plane. Because the (011) slip plane was tilted 45° relative to the hammering direction, the thickness of the

No. 4 leaf was estimated to be approximately 100 nm, which is a reasonable value.

3.4 Discussion

The IPF map (Fig. 1(a)) and KAM data (Fig. 3(a)) indicate that the Zumi foil retained a certain dislocation density without evidence of recrystallization [25]. The dislocation density increased in the No. 4 leaf, which indicates that no recrystallization or recovery occurred during the second hammering stage.

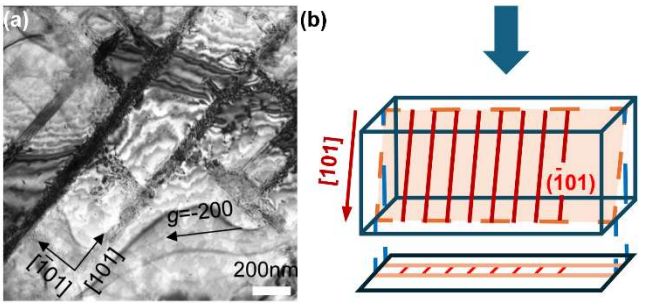

Figure 9. (a) BF-TEM image of the No. 4 leaf enlarged to show the local area shown in Fig. 5(a). A slip band with many dislocation lines arranged in a periodic pattern is formed along the [101] direction. (b) Schematic illustration of the slip plane and dislocations in the No. 4 leaf that can explain the slip band in (a). The blue arrow indicates the hammering direction (approximately [001]). The slip plane was determined to be the $(\bar{1}01)$ plane. The dislocations terminate at both surfaces with the Burger's vector of the [101] direction, which corresponds to screw dislocations. The dislocation lines are projected onto the screen.

In the BF-TEM image of the Zumi foil (Fig. 4), low-angle grain boundaries and dislocation tangles were observed, which suggests that dynamic recovery may have occurred during the first hammering stage that can be attributed to an increase in temperature within the package [26]. Conversely,

the DF-TEM image of the No. 4 leaf (Fig. 5(b)) indicated the presence of not only slip bands but also various dislocations and defects, and low-angle grain boundaries were rarely observed. These results suggest that the No. 4 leaf underwent high plastic strain without recovery or recrystallization in the second hammering stage, which matches the results of Aifantis [27] and is consistent with the argument that a lower deformation temperature impedes dynamic recovery and recrystallization [28]. The temperature within the package may have been lower because the package was opened periodically during the second hammering stage, and the high melting point of gold (T_m ≈ 1337 K) [30] would effectively prevent recovery or recrystallization.

During the hammering stages, stress is generated by two main factors: the vertical stress from the hammer and the frictional stress caused by the vertical stress at the contact between the *washi* paper and gold sheets. For the Zumi foil, which corresponded to the product of the first hammering stage, the out-of plane orientation was almost {110}, which can be attributed to the hammering, but the in-plane orientation was not along a specific direction, which suggests that the in-plane stress was isotropic. The {110} texture aligns with the prediction of the Taylor model for uniaxial compression, and experimental studies have also indicated that the formation of such a texture is associated with a uniaxial compression process [29] [30].

For the No. 4 leaf, which corresponded to the product of the second hammering stage, the out-of-plane orientation changed to {001}, and the in-plane orientation was also mostly aligned. Because the *washi* paper had a lower friction coefficient in the second hammering stage than in the first hammering stage, the former also seems to have resulted in uniaxial compression. In other words, the deformation was constrained in the hammering direction (ND) while remaining free in the in-plane direction.

During the second hammering stage, the No. 4 leaf exhibited a transition to its preferred textures. However, the dominant textures were rotated by 15° from the ideal rotated cube texture of {001} at <110> and were instead {001} at <310> (Fig. 2(b)). This cannot be explained by the conventional formation of cube textures driven by recrystallization that has been observed in hot-rolled FCC metals [11]. However, the rotated cube texture has been observed during cold rolling [31] [32] and has been attributed to the shear stress at the contact between the roll and sample surface [33] [34]. In the second hammering stage, the *washi* paper becomes so smooth that it may not rub against the gold leaf. This may explain the dominant formation of textures rotated 15° from the ideal rotated cube texture.

Kitagawa [3] used XRD to show that the {001} texture became dominant in Kanazawa gold leaf when the thickness was less than 0.3 μm, which suggests

that the sample thickness is a key factor for the formation of this texture. Dislocations near the surface have been reported to experience an image force [35] that draws dislocations toward the surface. Shan et al. [36] found that parts of a dislocation are attracted to the surface, which produces smaller segments. In metals, dislocation loops typically have a size of 100–200 nm, so a sample thickness of less than 200 nm may result in the loop partially exiting the surface and splitting into two dislocation lines terminating at both surfaces. These two dislocation lines are considered to primarily be components of screw dislocations. Edge dislocations, which have dislocation lines perpendicular to the sample surface, are likely to escape the surface entirely. Therefore, the slip band in Fig. 6(a) may have formed on the (011) slip plane and terminated on both surfaces of the No. 4 leaf.

The activation of non-octahedral slip systems, particularly the {011}–<011> slip system, has been reported in studies on the deformation studies of FCC metals at high temperatures [37] [38]. A competitive relationship has been observed between the {111}–<011> slip system and non-octahedral slip systems such as the {011}–<011> slip system in terms of the process temperature, processing rate, and stacking fault energy (SFE) [39] [40] [41] [42]. Under the condition that the processing temperature exceeds the recrystallization temperature ($0.6T_m$), the critical resolved shear stress of all

slip systems is reduced by the small influence of dislocations at high temperatures, which increases the likelihood of a slip occurring across all planes.

These results showed that the fabrication process of Kanazawa gold leaf is quite different from that of high-temperature fabrication processes. Dislocations on the {111} slip planes are entangled and immobilized because of extensive plastic deformation without recovery or recrystallization. When the thickness is reduced to about 100 nm, part of the dislocation loops exits the surface, which leaves behind a larger proportion of screw dislocations that are more likely to move and in turn results in non-octahedral slip systems such as the {110}–<110> slip system. In FCC crystals, screw dislocations on the (111) plane can cross-slip to the $(\bar{1}11)$ plane. In addition, those lines can protrude partially at an atomic distance. At the left and right ends of this protrusion, kinks with different signs are formed, which are called kink pairs. Bacroix and Jonas [39] showed that slip on the (011) plane occurs when these two phenomena occur. In detail, when a protruding dislocation line undergoes cross-slip, it can slip on the (011) plane due to the low Peierls barrier. Excluding the {011} planes, the {001} and {112} planes are also energetically favorable for slip in non-octahedral slip systems. Theoretically, the slip activation is affected by the effective shear stress [43] [44], which is

governed by the Schmid factor. The Schmid factor for the {011}–<011> slip system becomes much higher than that for other types of non-octahedral slip systems when the hammering direction gradually changes from [101] to

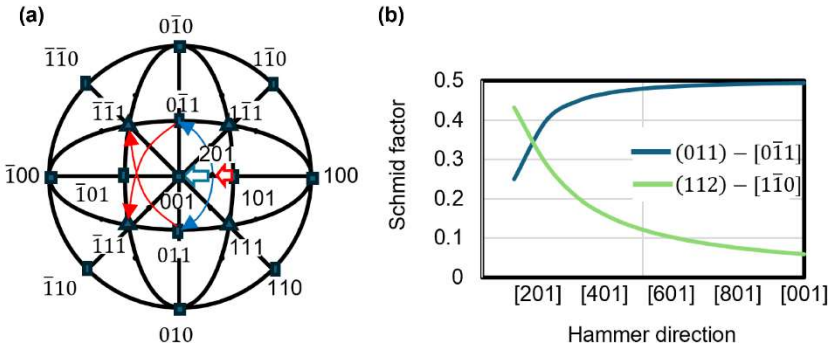

Figure 10. (a) Standard stereographic projection of the FCC crystal structure viewed from the [001] direction. After formation of the (101) texture, the hammering direction gradually changed from the [101] to the [201] direction by activation of either the $(\bar{1}\bar{1}1)$–[011] or $(\bar{1}11)$–$[0\bar{1}1]$ slip system (red curves). It gradually changed from the [201] to the [001] direction by activation of either the $(0\bar{1}1)$–[011] or (011)–$[0\bar{1}1]$ slip system (blue curves). These slip systems are non-octahedral. (b) Schmid factors for non-octahedral slip systems as a function of the hammering direction. The Schmid factor of the (112)–$[1\bar{1}0]$ slip system was high when the hammering direction was approximately along the [101] direction. However, the Schmid factor of the (011)–$[0\bar{1}1]$ slip system increased when the hammering direction changed from the [201] to the [001] direction.

[201].

Based on the observed results, Fig. 7 shows the formation process of Kanazawa gold leaf. In the first hammering stage, the (101) texture is formed because of activation of the (111)–$[0\bar{1}1]$ or $(1\bar{1}1)$–[011] slip system. In addition, because it is a low-temperature process, neither recrystallization nor recovery occurs, so the dislocations become entangled and immobilized.

In the second hammering stage, the entanglement of dislocations causes cross-slip of the screw dislocations, which activates the $(\bar{1}11)$–$[0\bar{1}1]$ or $(\bar{1}\bar{1}1)$–$[011]$ slip system instead of the initial slip system mentioned above and causes the crystal orientation to tilt from [101] to [201] along the Z-axis (Fig. 9(b)). A weak {201} texture forms in the Zumi foil (Fig. 3(b)). As the second hammering stage progresses, the $(0\bar{1}1)$–$[011]$ or (011)–$[0\bar{1}1]$ slip system is activated because of the high Schmid factor when the hammering direction reaches the [201] direction (Fig. 7(b)). In addition, entangled dislocations on the {111} slip planes due to extensive plastic deformation without recovery or recrystallization contribute to the activation of such a non-octahedral slip system, which changes the hammering direction from [201] to [001] and facilitates the formation of the (001) texture.

3.5 Conclusion

Kanazawa gold leaf samples corresponding to the products of the first hammering stage (Zumi foil) and second hammering stage (No. 4 leaf) were investigated by EBSD and TEM to clarify the fabrication process. The Zumi foil had the {011} texture but did not show uniform alignment of the in-plane orientations. A certain dislocation density was retained indicating no recrystallization, and the dislocations gathered near the grain boundaries. The No. 4 gold leaf had the {001} texture and showed almost uniform

alignment of the in-plane orientations. The average orientation deviated by 15° from the ideal rotated cube texture. Many dislocations were evenly distributed, which suggests that recrystallization or recovery did not occur. The entanglement and immobilization of dislocations may have activated cross-slip, which tilted the crystal orientation from [101] to [201] along the Z-axis. A non-octahedral {110}–<110> slip system was observed, which may have been induced by the entangled dislocations and high Schmid factor. The activation of the {110}–<110> slip system may have changed the hammering direction from [201] to [001] and caused the (001) texture to form. The alignment of the in-plane orientation may be related to the friction between the gold leaf and *washi* paper.

Reference

[1] K. Kitagawa and K. Tanimura, “Texture of aluminum leaf fabricated by hammering,” *Scr. Metall.*, vol. 20, no. 5, pp. 673–676, May 1986, doi: 10.1016/0036-9748(86)90488-6.

[2] K. Kitagawa and K. Tanimura, “Texture of gold leaf fabricated by hammering,” *Scr. Metall.*, vol. 20, no. 11, pp. 1511–1514, Nov. 1986, doi: 10.1016/0036-9748(86)90385-6.

[3] K. Kitagawa, “On the development of the (001) texture of gold leaf fabricated by hammering,” *J. Mater. Sci.*, vol. 23, no. 8, pp. 2810–2814, Aug. 1988, doi: 10.1007/BF00547454.

[4] P. Rodrigues and P. Bate, “Textures in non-ferrous metals and alloys,” *TMS Warrendale PA USA*, p. 173, 1985.

[5] A. K. Vasudévan, P. E. Bretz, A. C. Miller, and S. Suresh, “Fatigue crack growth behavior of aluminum alloy 2020 (Al□Cu□Li□Mn□Cd),” *Mater. Sci. Eng.*, vol. 64, no. 1, pp. 113–122, 1984, doi: https://doi.org/10.1016/0025-5416(84)90078-8.

[6] A. Akef and J. H. Driver, “Orientation splitting of cube-oriented face-centred cubic crystals in plane strain compression,” *Mater. Sci. Eng. A*, vol. 132, pp. 245–255, Feb. 1991, doi: 10.1016/0921-5093(91)90381-V.

[7] R. Becker, J. Butler, H. Hu, and L. Lalli, “Analysis of an aluminum single crystal with unstable initial orientation (001)[110] in channel die compression,” *Metall. Trans. A*, vol. 22, pp. 45–58, 1991.

[8] A. Godfrey, D. J. Jensen, and N. Hansen, “SLIP PATTERN, MICROSTRUCTURE AND LOCAL CRYSTALLOGRAPHY IN AN ALUMINIUM SINGLE CRYSTAL OF BRASS ORIENTATION {110}h112i”.

[9] Z. J. Li, A. Godfrey, and Q. Liu, “Macroscopic sub-division of rolled Al–1%Mn single crystals of 001〈110〉 orientation,” *Scr. Mater.*, vol. 45, no. 7, pp. 847–852, 2001, doi: https://doi.org/10.1016/S1359-6462(01)01104-6.

[10]J. Pospiech, J. Jura, A. Mücklich, K. Pawlik, and M. Betzl, “Deformation and Recrystallisation Textures of Polycrystalline Nickel,” *Texture Stress Microstruct.*, vol. 6,

no. 1, pp. 63–79, Jan. 1983, doi: 10.1155/tsm.6.63.

[11] F. Basson and J. H. Driver, “Deformation banding mechanisms during plane strain compression of cube-oriented f.c.c. crystals,” *Acta Mater.*, vol. 48, no. 9, pp. 2101–2115, May 2000, doi: 10.1016/s1359-6454(00)00042-2.

[12] O. Dalland and E. Nes, “Origin of cube texture during hot rolling of commercial Al□Mn□Mg alloys,” *Acta Mater.*, vol. 44, no. 4, pp. 1389–1411, Apr. 1996, doi: 10.1016/1359-6454(95)00289-8.

[13] Cl. Maurice and J. H. Driver, “High temperature plane strain compression of cube oriented aluminium crystals,” *Acta Metall. Mater.*, vol. 41, no. 6, pp. 1653–1664, Jun. 1993, doi: 10.1016/0956-7151(93)90185-U.

[14] D. Stojakovic, “Electron backscatter diffraction in materials characterization,” *Process. Appl. Ceram.*, vol. 6, no. 1, pp. 1–13, 2012, doi: 10.2298/PAC1201001S.

[15] W. Zhou and Z. L. Wang, *Scanning microscopy for nanotechnology: techniques and applications*. Springer science & business media, 2007.

[16] P. Parajuli, R. Mendoza-Cruz, U. Santiago, A. Ponce, and M. J. Yacamán, “The Evolution of Growth, Crystal Orientation, and Grain Boundaries Disorientation Distribution in Gold Thin Films,” *Cryst. Res. Technol.*, vol. 53, no. 8, p. 1800038, Aug. 2018, doi: 10.1002/crat.201800038.

[17] S. A. Jang, H. J. Lee, C. V. Thompson, C. A. Ross, and Y. J. Oh, “Crystallographic analysis of the solid-state dewetting of polycrystalline gold film using automated indexing in a transmission electron microscope,” *APL Mater.*, vol. 3, no. 12, p. 126103, Dec. 2015, doi: 10.1063/1.4937432.

[18] N. T. Razali, I. Osaka, K. Takimiya, V. Vohra, and H. Murata, “Achieving high efficiency and stability in inverted organic solar cells fabricated by laminated gold leaf as top electrodes,” *Appl. Phys. Express*, vol. 7, no. 11, p. 111602, 2014.

[19] D. An, T. A. Griffiths, P. Konijnenberg, S. Mandal, Z. Wang, and S. Zaefferer, “Nowell,” *Acta Mater.*, vol. 156, pp. 297–309, Sep. 2018, doi: 10.1016/j.actamat.2018.06.044.

[20] S. I. Wright, M. M. Nowell, R. De Kloe, and L. Chan, “Orientation Precision of Electron Backscatter Diffraction Measurements Near Grain Boundaries,” *Microsc. Microanal.*, vol. 20, no. 3, pp. 852–863, Jun. 2014, doi: 10.1017/S143192761400035X.

[21] V. Randle and O. Engler, “Introduction to Texture Analysis”.

[22] J. Yamasaki, Y. Ubata, and H. Yasuda, “Empirical determination of transmission attenuation curves in mass–thickness contrast TEM imaging,” *Ultramicroscopy*, vol. 200, pp. 20–27, 2019.

[23] Y. Oshima *et al.*, “Lorentzian-like image blur of gold nanoparticles on thick amorphous silicon films in ultra-high-voltage transmission electron microscopy,” *Microscopy*, vol. 62, no. 5, pp. 521–531, 2013.

[24] M. Jedrychowski, J. Tarasiuk, B. Bacroix, and S. Wronski, “Electron backscatter diffraction investigation of local misorientations and orientation gradients in connection with evolution of grain boundary structures in deformed and annealed zirconium. A new approach in grain boundary analysis,” *J. Appl. Crystallogr.*, vol. 46, pp. 483–492, Feb. 2013, doi: 10.1107/S0021889812052016.

[25] E. F. Ferdinand Knipschildt, “Nucleation of recrystallization,” *Mater. Sci. Technol.*, vol. 38, no. 12, pp. 765–779, 2022.

[26] S. Gourdet and F. Montheillet, “A model of continuous dynamic recrystallization,” *Acta Mater.*, vol. 51, no. 9, pp. 2685–2699, May 2003, doi: 10.1016/S1359-6454(03)00078-8.

[27] E. C. Aifantis, “The physics of plastic deformation,” *Int. J. Plast.*, vol. 3, no. 3, pp. 211–247, Jan. 1987, doi: 10.1016/0749-6419(87)90021-0.

[28] V. V. Stolyarov, Y. T. Zhu, I. V. Alexandrov, T. C. Lowe, and R. Z. Valiev, “Influence of ECAP routes on the microstructure and properties of pure Ti,” *Mater. Sci. Eng. A*, vol. 299, no. 1–2, pp. 59–67, 2001.

[29] S. Ahzi, S. M’Guil, H. Youssef, M. Khaleel, and J. Gracio, “Non-linear viscoplastic polycrystalline intermediate modelling for texture evolution in FCC metals: compression test,” *Mater. Werkst.*, vol. 36, no. 10, pp. 533–537, Oct. 2005, doi: 10.1002/mawe.200500900.

[30] Y. Y. Zhang, M. X. Tang, J. C. E, Z. Y. Zhong, and S. N. Luo, “Texture evolution of Cu nanopowder under uniaxial compression,” *Materialia*, vol. 1, pp. 236–243, Sep. 2018, doi: 10.1016/j.mtla.2018.06.001.

[31] H. Hu, P. Sperry, and P. A. Beck, “Rolling textures in face-centered cubic metals,” *Jom*, vol. 4, pp. 76–81, 1952.

[32] G. Wassermann, “Über die Abhängigkeit der Kristallitanordnung in gewalzten Aluminiumblechen von der Blechdicke,” *Met. Met. Met.*, vol. 12, no. 36, pp. 511–513, 1933.

[33] O. Engler, C. Tomé, and M.-Y. Huh, “A study of through-thickness texture gradients in rolled sheets,” *Metall. Mater. Trans. A*, vol. 31, no. 9, pp. 2299–2315, 2000.

[34] C. Lee and B. Duggan, “A simple theory for the development of inhomogeneous rolling textures,” *Metall. Trans. A*, vol. 22, pp. 2637–2643, 1991.

[35] D. Hull and D. J. Bacon, Eds., *Introduction to dislocations*, 5th ed. in Materials science and technology (New York, N.Y.), no. v. 37. Oxford: Butterworth-Heinemann, 2011.

[36] Z. W. Shan, R. K. Mishra, S. A. Syed Asif, O. L. Warren, and A. M. Minor, “Mechanical annealing and source-limited deformation in submicrometre-diameter Ni crystals,” *Nat. Mater.*, vol. 7, no. 2, pp. 115–119, Feb. 2008, doi: 10.1038/nmat2085.

[37] M. Arzaghi, B. Beausir, and L. S. Tóth, “Contribution of non-octahedral slip to texture evolution of fcc polycrystals in simple shear,” *Acta Mater.*, vol. 57, no. 8, pp. 2440–2453, May 2009, doi: 10.1016/j.actamat.2009.01.041.

[38] Ph. Lequeu, P. Gilormini, F. Montheillet, B. Bacroix, and J. J. Jonas, “Yield surfaces for textured polycrystals—I. Crystallographic approach,” *Acta Metall.*, vol. 35, no. 2, pp. 439–451, Feb. 1987, doi: 10.1016/0001-6160(87)90250-1.

[39] B. Bacroix and J. J. Jonas, “The Influence of Non-Octahedral Slip on Texture Development in FCC Metals,” *Texture Stress Microstruct.*, vol. 8, no. 1, pp. 267–311, Jan. 1988, doi: 10.1155/TSM.8-9.267.

[40] A. Mecif, B. Bacroix, and P. Franciosi, “Temperature and orientation dependent plasticity features of Cu and Al single crystals under axial compression—I. Lattice rotation effects and true hardening stages,” *Acta Mater.*, vol. 45, no. 1, pp. 371–381, 1997.

[41] R. Le Hazif, P. Dorizzi Et, and J. P. Poirier, “Glissement {110} 〈110〉 dans les metaux de structure cubique a faces centrees,” *Acta Metall.*, vol. 21, no. 7, pp. 903–911, Jul. 1973, doi: 10.1016/0001-6160(73)90148-X.

[42] R. Le Hazif and J.-P. Poirer, “Cross-slip on {110} planes in aluminum single

crystals compressed along 〈100〉 axis," *Acta Metall.*, vol. 23, no. 7, pp. 865–871, Jul. 1975, doi: 10.1016/0001-6160(75)90203-5.

[43] F. Perocheau and J. H. Driver, "Slip system rheology of Al–1% Mn crystals deformed by hot plane strain compression," *Int. J. Plast.*, vol. 18, no. 2, pp. 185–202, Feb. 2002, doi: 10.1016/S0749-6419(00)00075-9.

[44] M. Carrard and J. L. Martin, "A study of (001) glide in [112] aluminium single crystals," *Philos. Mag. A*, vol. 56, no. 3, pp. 391–405, Sep. 1987, doi: 10.1080/01418618708214395.

Chapter 4 Alloy element in Kanazawa gold leaf

4.1 Introduction

Kanazawa gold leaf is not just pure gold; it is an alloy containing silver and copper. The alloys can be divided based on their gold content, ranging from No. 1 to No. 4, as shown in Chapter 1. For example, No. 4 contains approximately 8.5 wt% Ag and 1.9 wt% Cu [1,2]. This classification is significant as it impacts both the mechanical and aesthetic properties of the leaves. One unique combination, comprising roughly equal parts of silver and gold, enhances specific properties without compromising the intrinsic qualities of gold.

Gold is known for its high ductility and plasticity, but at nanoscale thickness, it becomes fragile and brittle. Alloy addition elements are implemented to enhance mechanical stability while maintaining ductility, such as silver and copper [3]. The use of silver is most popular in the production of Kanazawa gold leaf due to its ability to maintain the bright face of gold and facilitate hammering without significant changes in color and hardness, which contrasts with copper[4]. Silver's addition also helps maintain the alloy's reflectivity and durability, which are essential for both aesthetic and structural qualities [5].

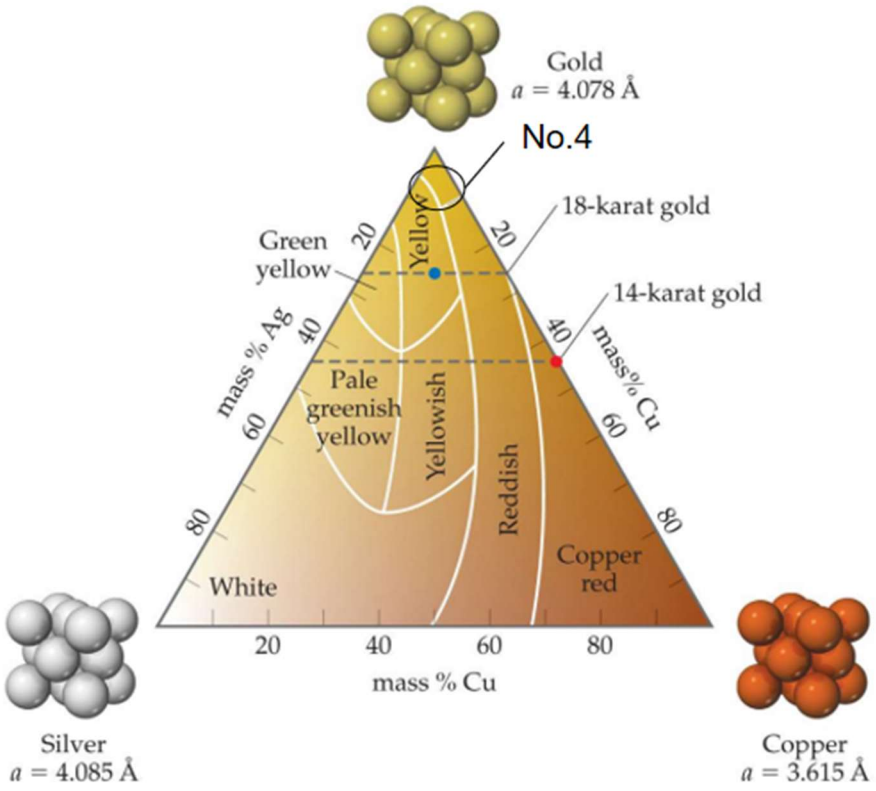

Figure 11 A ternary phase diagram of three elements Au, Ag, and Cu of color [6].

Although silver is more commonly used as an alloying element in Kanazawa gold leaf, copper may seem like a more cost-effective choice for achieving a color similar to pure gold [7]. It is easily understandable that the industrial 18k and 22k gold alloys contain a much higher amount of copper compared with Kanazawa gold leaf, as shown in Figure 1.

The choice of silver in Kanazawa gold leaf likely has both aesthetic and practical reasons. While copper can lower the costs and maintain the color close to that of pure gold, its presence alters the physical properties of the

alloy, making it harder and less ductile and, of course, rendering the process more difficult. Understanding the rationale behind choosing silver over copper as an alloying element reveals the delicate balance between optimizing processing performance, preserving visual appeal, and ensuring mechanical stability in this traditional Japanese craft.

4.2 Materials and Methods

This work features powdered Kanazawa No. 4 gold leaf and pure gold leaf. Transmission Electron Microscopy (TEM) was conducted using the TEM-2100plus, which is equipped with an Energy-Dispersive X-ray Spectroscopy (EDS) detector to analyze alloy composition.

4.3 Results and discussion

4.3.1 TEM Imaging of Pure Gold Leaf and No.4 Gold Leaf

Figures 2 and 3 show the microstructures of pure gold and No. 4 gold leaf, respectively, as observed from the [001] direction. The microstructure of pure gold leaf in Figure 2 exhibits band-like structures approximately 70 nm wide, aligned along the [1-10] direction, which correspond to slip bands that significantly impact the deformation behavior. It indeed reflects the generation of a well-defined slip band on the {110} plane as has already been

explained in Chapter 3.

Compared to this, Figure 3 shows a similar band-like structure in the No. 4 gold leaf, aligned along the [110] direction, marked by the blue arrow, indicating that the slip characteristic is maintained despite the addition of alloying elements. The low dislocation density observed may be related to surface disruption caused by powdering and, therefore, has a limited influence on the near-surface structure.

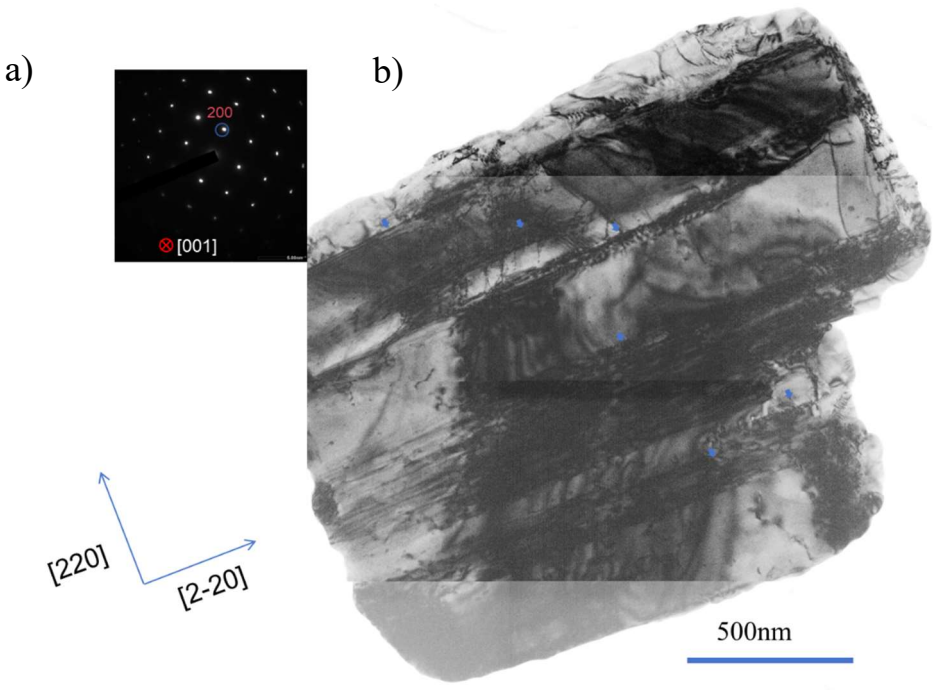

Figure 12.BF field image from [001] direction form pure gold leaf.

Additionally, slip bands on the {011} plane, as discussed in Chapter 3, were observed in both No.4 gold leaf and pure gold. This confirms that a non-octahedral slip occurs in both types of gold leaf. Furthermore, no significant

microstructural differences were detected between the two, indicating that No.4 gold leaf maintains a high degree of similarity to pure gold in terms of

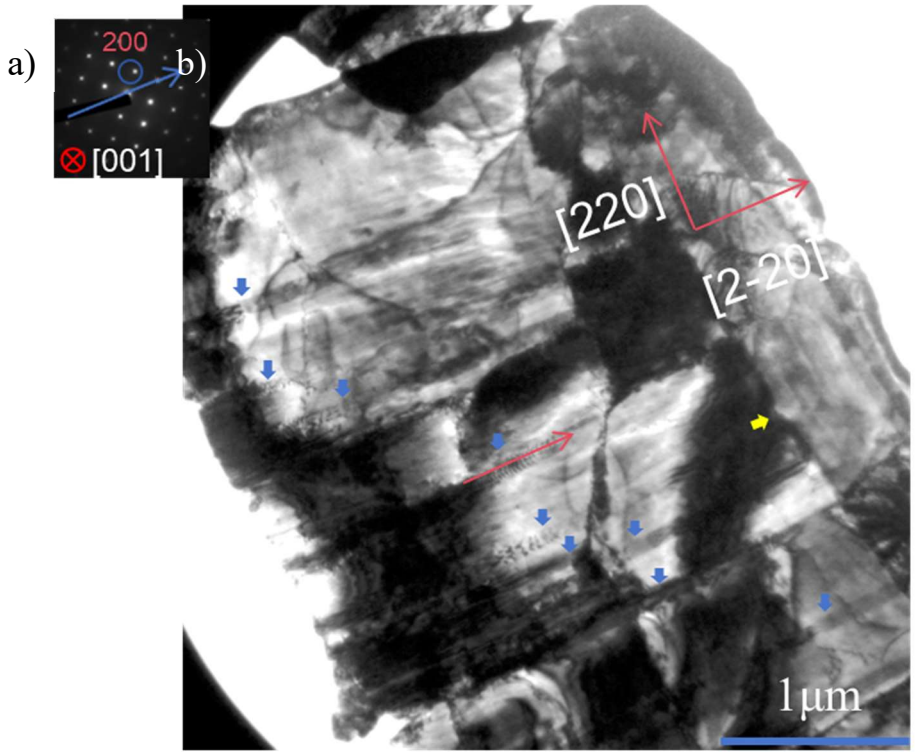

Figure 13.BF image form [001] direction for the No.4 gold leaf.

slip behavior and overall microstructure.

4.3.2 EDS and TEM Data for No.4 Gold Leaf

Further EDS analysis carried out on No. 4 gold leaf from the [001] direction is presented in Figure 4. This also shows the slip band, corresponding to the [110] and [1-10] directions, as shown in Figure 4b. The composition in this region, as shown in Figure 4c, is approximately 90% gold, 9% silver, and 1% copper, matching the standard No. 4 alloy ratio.

Figure 4 demonstrates the uniform distribution of alloying elements—silver

and copper—across the sample, with no significant clustering of either aspect. This even distribution results in an α-phase alloy, which supports a stable atomic structure and prevents the formation of ordered superlattices in the No. 4 gold leaf. The α-phase structure also indicates that the alloying elements have a minimal impact on the crystal structure, highlighting a substantial similarity between No. 4 gold leaf and pure gold. Studies on phase stability in gold alloys reveal that such α-phase structures promote a homogeneous atomic distribution and limit the formation of superlattices, resulting in stable mechanical properties and minimal alteration to gold's inherent characteristics [8].

In the [011] directional view (Figure 5), a residual grain aligned along the

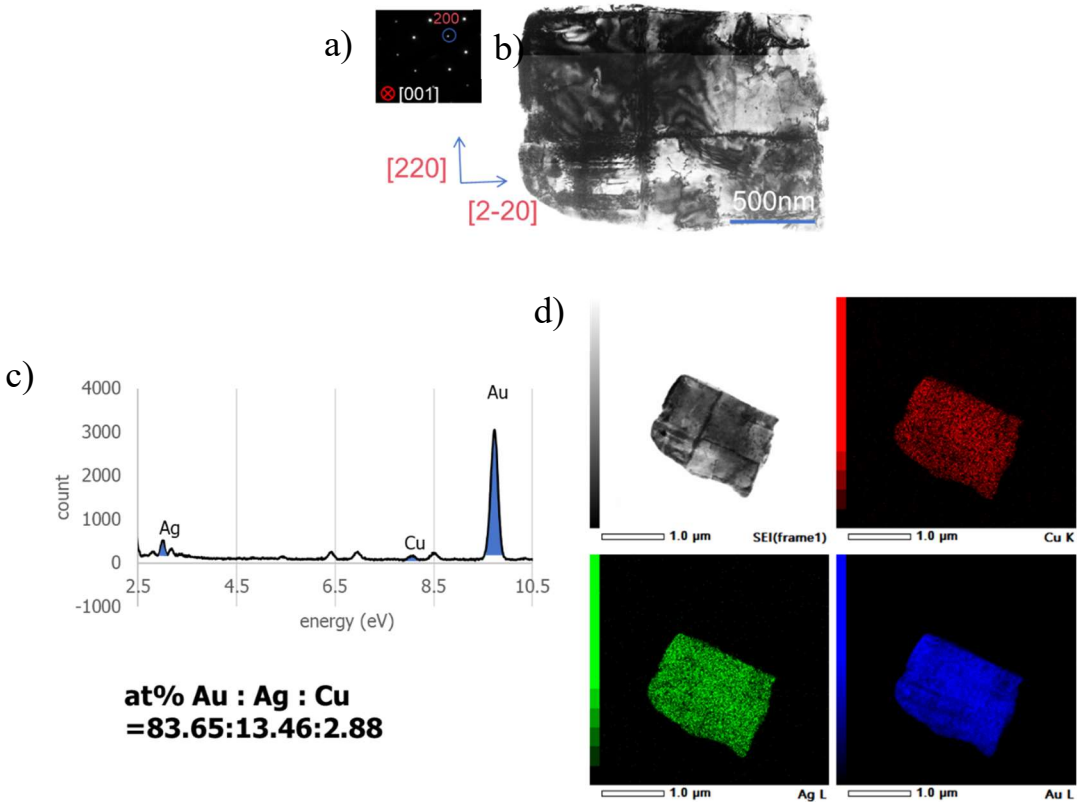

Figure4. a) is the diffraction pattern form [001] direction; b) is the BF image form same condition; c) is eds spectrum analysis, showing the at% of every atom; d) is the eds elements map, red is for copper, green is for silver, blue is for gold.

(011) plane, as indicated by EBSD analysis in Chapter 3, displays red bands that align with the {111} plane. These bands represent specific slip systems that are important for deformation behavior. Unlike the (001) plane, which may display non-octahedral slip bands, the (011) plane lacks these features.

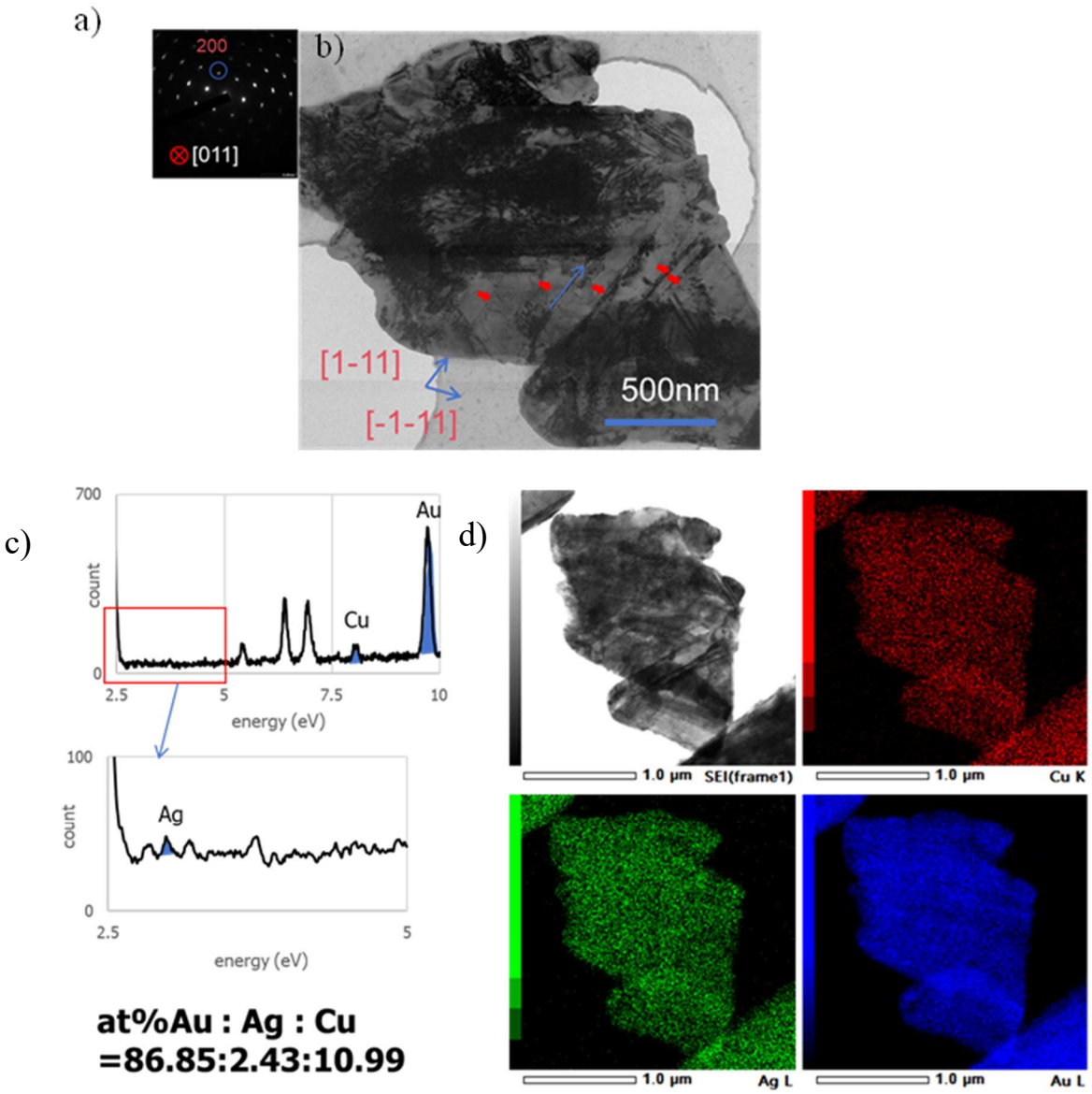

Figure 14. a) is the diffraction pattern form [011] direction; b) is the BF image form same condition; c) is eds spectrum analysis, showing the at% of every atom; d) is the eds elements map, red is for copper, green is for silver, blue is for gold.

However, slip activity along the {111} plane may still contribute to the material's deformation.

In Figure 5c, the copper content in the observed region is approximately

10.9at %, notably higher than the standard levels in No. 4 gold leaf. Despite this increased concentration, non-octahedral slip structures are absent in this region. Non-octahedral slip primarily occurs through a mechanism called the kink-pair mechanism, which requires a high density of screw dislocations[9].

Le Hazif and Dorizzi indicated that non-octahedral slip activity is influenced by stacking fault energy (SFE), with higher SFE levels promoting this type of slip [10, 11]. Although the alloying elements in No.4 gold leaf are insufficient to alter the lattice structure significantly, they can still impact SFE due to their atomic properties. L. F. Vassamillet and T. B. Massalski suggested that small amounts of silver (below 4 at %) do not significantly affect SFE. In comparison, copper levels above 1 at % can substantially reduce SFE due to differences in the Fermi surfaces of copper and gold [12]. Thus, if the copper content in gold leaf exceeds 1 at %, the SFE would decrease sufficiently to inhibit non-octahedral slip, thereby limiting further deformation in these regions. As discussed in Chapter 3, the continued thinning of Kanazawa gold leaf largely depends on non-octahedral slip, as regions without sufficient non-octahedral slip tend to retain more thickness. In other words, if the percentage of copper is higher than 1at % in the gold leaf, as a result of the higher reducing power in the SFE, the non-octahedral slip may stop, and lead deformation cannot proceed further.

4.4 Conclusion

Slip bands on the {011} plane, as discussed in Chapter 3, were observed in both No.4 gold leaf and pure gold, confirming that non-octahedral slip occurs in both types of gold leaf. Furthermore, no significant microstructural differences were detected between the two, indicating that No.4 gold leaf maintains a high degree of similarity to pure gold in terms of slip behavior and overall microstructure.

EDS analysis confirms the uniform distribution of silver and copper in No. 4 gold leaf, resulting in a stable α-phase alloy that ensures a homogeneous atomic structure without the formation of superlattices. The slightly higher copper concentration observed on the (011) plane, which reduces stacking fault energy, may contribute to inhibiting non-octahedral slip. This reduction in SFE limits the gold leaf's capacity to rely on the non-octahedral slip for continuous deformation. Therefore, this explains why the copper content in Kanazawa gold leaf is carefully controlled to remain below 1%. Keeping copper at this low level helps preserve the advantageous slip systems and overall deformation capabilities, ensuring that the leaf retains its desired mechanical properties and workability.

Reference

[1] K. Kitagawa and K. Tanimura, “Texture of gold leaf fabricated by hammering,” *Scripta Metallurgica*, vol.. 20, no. 11, pp. 1511–1514, Nov. 1986, doi: 10.1016/0036-9748(86)90385-6.

[2] K. Kitagawa, “On the development of the (001) texture of gold leaf fabricated by hammering,” *J Mater Sci*, vol. 23, no. 8, pp. 2810–2814, Aug. 1988, doi: 10.1007/BF00547454.

[3] E. F. Roberts and K. M. Clarke, “The colour characteristics of gold alloys,” *Gold Bulletin*, vol. 12, no. 1, pp. 9–19, 1979.

[4] K. [Kanazawa Inst. of T. "Kitagawa Ishikawa (Japan). Faculty of Engineering]", “Skill and wisdom of craftsman of gold leaf; Kinpaku shokunin no waza to chie,” [], vol. 99, Jan. 1996.

[5] R. M. German, M. M. Guzowski, and D. C. Wright, “The colour of gold-silver-copper alloys: Quantitative mapping of the ternary diagram,” *Gold Bulletin*, vol. 13, no. 3, pp. 113–116, 1980.

[6] S. Lakshmipriya, S. Bhuvaneswari, V. Parvathy, C. R. Suganya Devi, and M. Abinaya, “IoT based detection of adulteration in Gold using ANN,” *IOP Conf. Ser.: Mater. Sci. Eng.*, vol. 764, no. 1, p. 012018, Feb. 2020, doi: 10.1088/1757-899X/764/1/012018.

[7] L. Gal-Or, “Gold Alloys,” presented at the The Santa Fe Symposium on Jewelry Manufacturing Technology 1987, 1987, pp. 57–75.

[8] T. Uzuka, Y. Kanzawa, and K. Yasuda, “Determination of the AuCu superlattice formation region in gold-copper-silver ternary system,” *Journal of Dental Research*, vol. 60, no. 5, pp. 883–889, 1981.

[9] D. Caillard and J.-L. Martin, “Glide of dislocations in non-octahedral planes of fcc metals: a review,” *International journal of materials research*, vol. 100, no. 10, pp. 1403–1410, 2009.

[10] R. Le Hazif and J.-P. Poirer, “Cross-slip on {110} planes in aluminum single crystals compressed along 〈100〉 axis,” *Acta Metallurgica*, vol. 23, no. 7, pp. 865–

871, Jul. 1975, doi: 10.1016/0001-6160(75)90203-5.

[11] R. Le Hazif, P. Dorizzi Et, and J. P. Poirier, “Glissement {110} 〈110〉 dans les metaux de structure cubique a faces centrees,” *Acta Metallurgica*, vol. 21, no. 7, pp. 903–911, Jul. 1973, doi: 10.1016/0001-6160(73)90148-X.

[12] L. F. Vassamillet and T. B. Massalski, “Stacking Fault Probabilities of Some Internoble Metal Alloys,” *Journal of Applied Physics*, vol. 34, no. 11, pp. 3402–3404, Nov. 1963, doi: 10.1063/1.1729200.

Chapter 5: Aluminum (Al) Leaf

5.1 Introduction

In Kanazawa, other metals, such as aluminum, silver, copper, and brass, are also subjected to traditional techniques for making gold leaf [1]. Previous studies have shown that the Al leaf forms a (001) texture during processing, similar to the texture in Kanazawa gold leaf [2]. This stimulated interest in understanding the mechanisms responsible for texture formation in Al, as texture is a crucial factor that determines the mechanical properties and behavior of a material.

Aluminum has some peculiarities in terms of thinning. A (001) texture often forms during annealing or high-temperature processing, which improves ductility and formability [3]. In contrast, a (011) texture, which is associated with increased strength, typically results from cold working[4]. In this part, we will investigate the texture formation in Al leaf, with a particular focus on the hammering process and a comparison to the texture observed in Chapter 3.

5.2 Materials and Methods

The Al leaf sample is thick at 0.37 μm. Similar to gold leaf, it is produced

through the hammering process; however, the thickness of Aluminum leaf cannot be reduced further using this method. The primary analytical tools used in this study are Transmission Electron Microscopy (TEM) and Electron Backscatter Diffraction (EBSD) techniques, which are employed via Scanning Electron Microscopy (SEM).

5.3 Results and discussion

5.3.1 EBSD Analysis

Figure 1 illustrates the EBSD Inverse Pole Figure (IPF) and IPF coloring maps for the Al leaf, observed on a plane perpendicular to the hammering

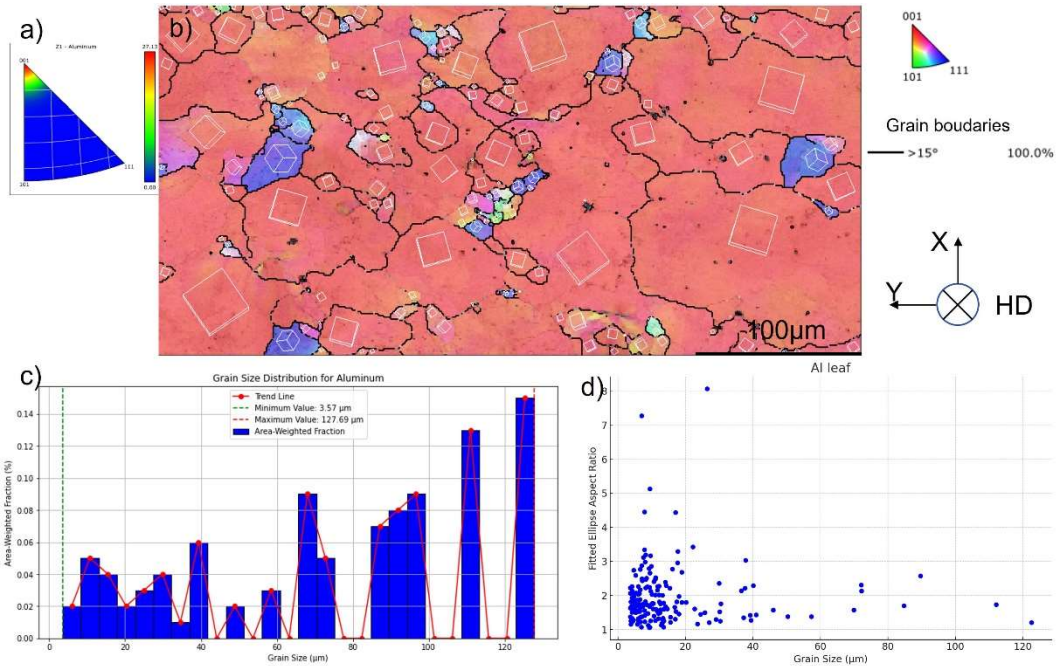

Figure 15.the EBSD data for Al leaf from HD. a) is the IPF figure; b) is the IPF-color map; c) is the grain size in such area; d) is the aspect ratios combine with the grain size.

direction (HD). Figure 1a presents the IPF analysis, which reveals a firm (001) texture. As shown in Figure 1 b, the red-colored regions, corresponding to the (001) orientations, dominate the IPF color map. This distribution suggests an inhomogeneous internal texture of scattered (001) regions across the Al leaf.

As shown in Figure 1c, grain sizes range from 3.57 to 120 μm. In Figure 1d, grain shapes are depicted using fitted ellipses, but the aspect ratios for most grains are less than 3, indicating their equiaxed nature. The aspect ratios of many grains are less than 1.5. This suggests that equiaxed grains are present

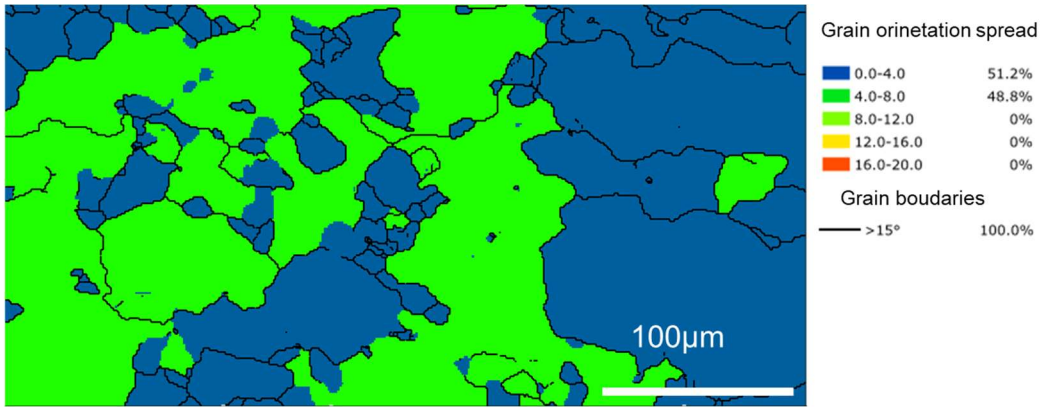

Figure 16. The GOS map, analysis form the HD.

across a range of sizes, not just limited to smaller grains, which contrasts with observations in cold-worked aluminum. It is a remarkably equiaxed microstructure compared to what has been reported for cold-worked aluminum in the literature.

Figure 2 is a GOS map. The color in this map shows an internal level of stress

inside the grains. Areas in blue correspond to GOS below 4° and represent low internal misorientations regarding grain average orientation and very low internal stresses, which cover 51.2% of the analyzed area. At the same time, areas where GOS values lie between 4° and 8° correspond to regions with higher internal stresses. The hammering process results in severe deformation, reducing the material's thickness by over 90% from its initial state. The lower stresses measured in some of the grains imply the occurrence of recrystallization mechanisms, which would act to reduce dislocation

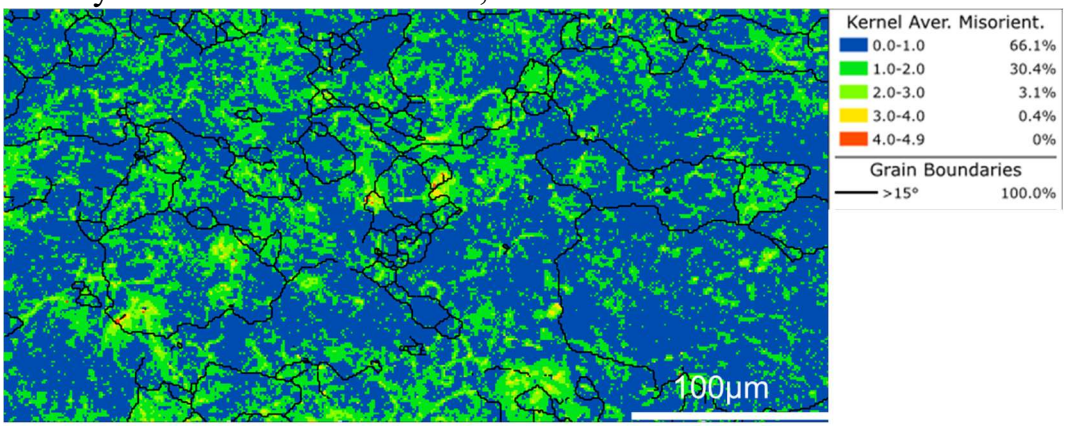

Figure 17. The KAM map analysis from the HD.

density. These observations align with those made by other researchers in studies of metals deformed to large strains [5]. Together, grain morphology and distribution of residual stress are consistent with features characteristic of recrystallized structures.

Figure 3, KAM map of the Al leaf. Blue coloration indicates little dislocation density and internal strain within that region. Warmer colors indicate a

greater misorientation, hence, higher dislocation densities and localized strain.

Notably, grains with orientations differing from (001) show higher dislocation densities, suggesting that specific orientations may be more dislocations. Most of the grains appear blue; thus, much of the sample has undergone efficient dislocation density reduction through recrystallization [6].

5.3.2 TEM Analysis

Figure 4 is an enlarged view of one grain, surrounded by boundaries numbered 1 to 4, with an area of 32.3 μm^2, which falls within the range of the sizes of the smaller grains identified in the EBSD analysis. Within this grain, dislocations form tangled line structures, as exemplified in the blue box, characteristic of localized strain accommodation; however, the dislocation density is generally low. The bright and dark linear structures that appear alternately in the green area indicate the formation of dislocation subgrains due to the high SFE of aluminum, which discourages the generation of stacking faults and enhances cross-slip.

The boundaries of grains 1, 2, and 3 are relatively straight with few dislocations in the vicinity; this infers that the boundary is stable and the magnitude of internal stresses that have built up is not significant. Grain

boundary 4 is wavy in appearance and falls within the influence of dislocation cells in the vicinity, suggesting that localized deformation and concentration of internal stresses occur. Dislocations accumulate along this grain boundary, expanding the dislocation cell structure to approximately 1 μm in width, which may contribute to localized hardening.

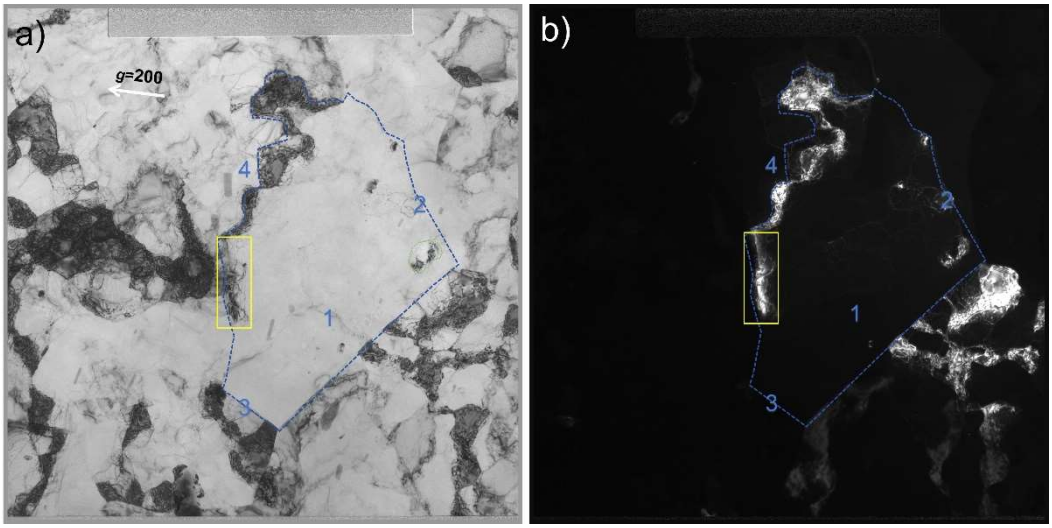

Figure 18. Ultra-high voltage TEM image of Al leaf form [001] direction. a) is the BF image; b) is the DF image.

Within the dislocation cell, reorganization is observed in the green-boxed area. In contrast, in the yellow-boxed portion, a configuration is formed that leads to the creation of new grain boundaries, indicating partial recrystallization. In such grain, a typical coexistence of recrystallized and non-recrystallized regions within a single grain may occur in materials processed under dynamic recrystallization [7].

5.3.3 Texture Analysis

Figure 5 shows Pole figures for Al leaf. Figure 5a is the {001} pole figure

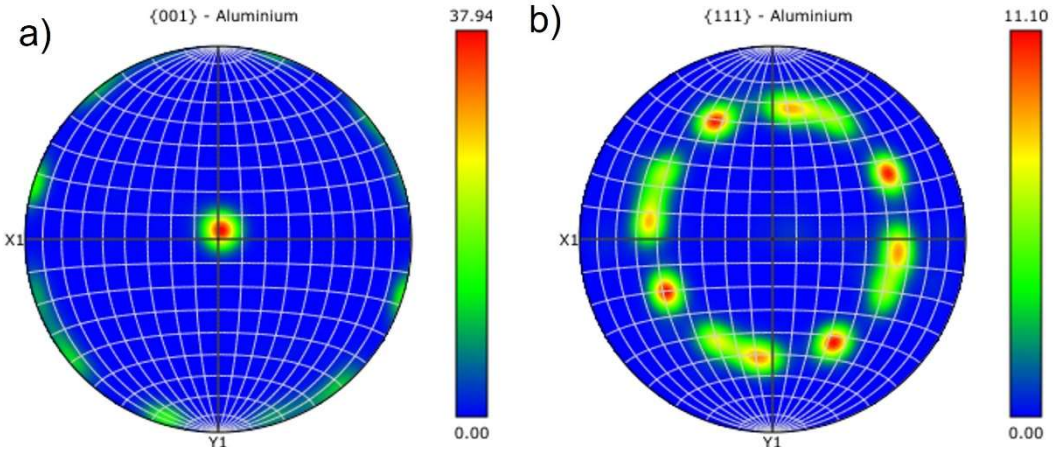

Figure 19. The pole figure form EBSD analysis. a) is the pole figure form {001} of the Al leaf; b) is the pole figure form {111} of the Al leaf.

showing a sharp peak in the {001} direction. This demonstrates a very significant {001} texture in the Al leaf. Figure 5b is a {111} pole figure, showing two peaks: one strong near <001> {100} and a weaker peak near <011> {100}. The misorientation of these peaks from the main crystal directions means incomplete texture development.

This incomplete texture can be attributed to partial recrystallization and the hammering process, which introduce complex stress states and grain realignment. The more substantial peak corresponds to the classical cube texture <001> {100}, typically associated with fully recrystallized aluminum, indicating that recrystallization has occurred [8]. The weaker one near <011>

{100} indicates a shear texture, which is generally associated with rolling processes and confirms the mechanical deformation effect[9]. EBSD analysis reveals a scattered (001) texture with equiaxed grains, unlike the elongated structures typically observed in cold-worked aluminum, suggesting that dynamic recrystallization through hammering is driving the development of the {001} texture [10]. Grain Orientation Spread (GOS) and Kernel Average Misorientation (KAM) maps indicate that hammering not only induces significant deformation but also promotes recrystallization, thereby reducing dislocation density [11]. TEM observations further confirm partial recrystallization, highlighting dislocation sub-grains and a heterogeneous microstructure.

Given that the melting point of aluminum is around 600°C, recrystallization for aluminum leaf begins at lower temperatures compared to gold leaf. Consequently, even with continuous hammering, complete recrystallization is not achieved; instead, the process remains within the realm of dynamic recrystallization.

5.4 Conclusion

Through EBSD and TEM data analysis, we investigated the primary reasons for the formation of the (001) texture in Al leaf. This (001) texture in Al leaf

primarily consists of two components: a cube texture, with orientation <001> {001}, and a shear texture, with orientation <011> {001}. However, the development of both textures is incomplete, indicating that the recrystallization process is not fully mature.

Based on the recrystallization features and dislocation structures observed in EBSD and TEM, we infer that the Al leaf undergoes a process of dynamic recrystallization during hammering. This behavior differs significantly from the (001) texture formation observed in gold leaf, as discussed in Chapter 3. The primary factor underlying this difference is the substantially lower recrystallization temperature of aluminum (Al) compared to gold (Au).

Reference

[1] K. [Kanazawa Inst. of Tech. "Kitagawa Ishikawa (Japan)"]. Faculty of Engineering. “Skill and Wisdom of the Craftsman of Gold Leaf: Kinpaku Shokunin no Waza to Chie,” vol. 99, Jan. 1996.

[2] K. Kitagawa and K. Tanimura, “Texture of aluminum leaf fabricated by hammering,” *Scripta Metallurgica*, vol. 20, no. 5, pp. 673–676, May 1986, doi: 10.1016/0036-9748(86)90488-6.

[3] M. Huh, S. Cho, and O. Engler, “Randomization of the annealing texture in aluminum 5182 sheet by cross-rolling,” *Materials Science and Engineering: A*, vol. 315, no. 1–2, pp. 35–46, 2001.

[4] Q. Xing, X. Huang, and N. Hansen, “Recovery of heavily cold-rolled aluminum: Effect of local texture,” *Metallurgical and materials transactions A*, vol. 37, pp. 1311–1322, 2006.

[5] M. S. Khorrami and M. Kazeminezhad, “Post deformation at room and cryogenic temperature cooling media on severely deformed 1050-Aluminum,” *Metals and Materials International*, vol. 24, pp. 401–414, 2018.

[6] R. Kaibyshev and S. Malopheyev, “Mechanisms of dynamic recrystallization in aluminum alloys,” presented at the Materials Science Forum, Trans Tech Publ, 2014, pp. 784–789.

[7] M. Crumbach, M. Goerdeler, G. Gottstein, L. Neumann, H. Aretz, and R. Kopp, “Through-process texture modelling of aluminium alloys,” *Modelling and simulation in materials science and engineering*, vol. 12, no. 1, p. S1, 2003.

[8] I. Samajdar and R. Doherty, “Cube recrystallization texture in warm deformed aluminum: understanding and prediction,” *Acta materialia*, vol. 46, no. 9, pp. 3145–3158, 1998.

[9] G. L. Wu, “Recrystallization microstructure and texture of highly strained commercial purity aluminium alloy,” presented at the Materials Science Forum, Trans Tech Publ, 2014, pp. 282–287.

[10] P. Ramesh Narayanan, S. Suwas, K. Sreekumar, P. P. Sinha, and S. Ranganathan, “Evolution of crystallographic texture in cold rolled al-zn-mg alloys used in space

applications," presented at the Materials Science Forum, Trans Tech Publ, 2012, pp. 315–319.

Acknowledgement

First and foremost, I would like to express my deepest gratitude to my supervisor, Professor Yoshifumi Oshima, for his invaluable guidance, unwavering support, and constant encouragement throughout my academic journey. I am deeply indebted to him for not only guiding me in my research but also teaching me valuable life lessons. His insights and mentorship have profoundly shaped my thinking and approach to research. I am especially grateful for the many opportunities he provided for me to participate in academic conferences, which have greatly enriched my experience and broadened my perspective.

I would also like to extend my heartfelt thanks to Professor Satoshi Ichikawa of Osaka University for granting me access to state-of-the-art ultrahigh-voltage electron microscopy facilities. His expertise, valuable suggestions, and insightful advice have been instrumental in advancing my research. My sincere appreciation goes to Professor Hideyuki Murata of JAIST for generously providing powder samples and facilitating access to critical literature, which has been indispensable to my work.

I am equally thankful to Professor Lei Xiaobin from the Institute of Science, Tokyo, for her patient guidance, valuable suggestions, and assistance during

my minor research, which significantly contributed to my academic growth.

I owe a deep debt of gratitude to Professor Yukiko Takamura and Professor Mikio Koyano, both from JAIST, for dedicating their time to thoroughly reviewing my thesis and providing thoughtful feedback and advice that will continue to guide me in my future studies. I also wish to thank Assistant Professor Kohei Aso of JAIST for her invaluable support in sample preparation.

I am immensely grateful to my lab colleagues, Mr. W. Xiong, Mr. X. Liu, and Mrs.L.Chen, for their thoughtful discussions and constructive suggestions on my research. I extend special thanks to my seniors, Dr. L. Xie, Dr. T. Chen, and Mrs. T. Yang, for their kind guidance in TEM operation and expertise in EBSD. I am also grateful to my friends, Dr. Y. Qi and Mr. D. Chong, for their encouragement, discussions, and support. To all my friends at JAIST, thank you for making my time here so memorable and enriching. Finally, I would like to express my heartfelt gratitude to my family for their unconditional love and unwavering support throughout this journey. Their belief in me has been my greatest source of strength.

Thank you all for being a part of this meaningful chapter in my life.